INFLUENCE OF NON-DIPOLE TRANSITIONS ON THE EXTRACTION OF EMCD

Master Thesis

PAUL MICHEL ZEIGER

UPPSALA
UNIVERSITET

Department of Physics and Astronomy

Supervisor: Dr. Ján Rusz
Uppsala, 2019

ABSTRACT

ELNES-spectra of the L_3 and L_2-edge of bcc-iron are simulated using a Bloch wave method for the calculation of the DDSCS within a 1st-order Born approximation of the inelastic electron scattering process in order to study the influence of non-dipole terms on the EMCD-signal. The necessary electronic structure information is obtained from a DFT-calculation using `WIEN2k`.

Two different different ways of extracting the EMCD-signal are considered: the pEMCD-signal, which is extracted from the pure imaginary part of the MDFF, and the eEMCD-signal, extracted via an EMCD difference method.

A non-negligible contribution of the 13 cross term to the eEMCD-signal is found. Furthermore it is shown that the double difference method and the single left-right difference method cancel out the contributions of the 01-term to the eEMCD-signal. The pEMCD-signal is found to be influenced by non-dipole terms only for large scattering angles. Conclusive quantitative results on the influence of non-dipole contributions to the eEMCD-signal remain to be found, however, since it is uncovered that the eEMCD-signal is strongly disturbed by the choice of the post-edge normalization range due to the inaccurate description of the post-edge region in the present simulation. Furthermore a not anticipated ”apparent anisotropy” of the real part of the MDFF is found, whose cause is presently unknown.

As a byproduct of these investigations deeper insight is gained on a reason, why the double difference method is superior to the other extraction methods. It practically eliminates the effect of non-dipole terms 01 and 12.

Lastly two effects are encountered that might pave the way to a deeper understanding of why the L_2-edge is experimentally often observed to be weakened or suppressed relative to the L_3-edge in comparison with simulations.

POPULÄRVETENSKAPLIG SAMMANFATTNING PÅ SVENSKA

Inom fysiken skiljer man mellan två olika sätt som två objekt kan kollidera. Om ett av objekten är en våg så kallas kollisionen för att vågen sprids. Det finns elastisk och inelastisk spridning. Vid elastisk spridning överförs ingen energi mellan de båda objekten. Vid inelastisk spridning å andra sidan förandras energin hos båda objekten. Om man skjuter elektroner på ett prov växelverkar de med de elektroner och atomkärnor som utgör provmaterialet. En maskin som gör detta är transmissionselektronmikroskopet (TEM) där strömmen av eletroner kallas för en stråle. Efter växelverkan med provet mäts elektroner med hjälp av en elektrondetektor. Det finns olika typer av detektorer men man kan förenklat klassificera dem i detektorer som mäter energin av elektroner och detektorer som enbart mäter att en elektron har detekterats.

Små objekt som elektroner beskrivs inom kvantfysiken som en våg och därfor är växelverkan mellan strålelektroner och provmaterialet en spridning av elektronvågor. Som sagt skiljer man mellan elastiska och inelastiska processer och elektroner sprids huvudsakligen elastiskt i interaktion med atomkärnor. Växelverkan mellan provmaterialets elektroner och strålelektroner är å andra sidan huvudsakligen en inelastisk process. Det finns tre huvudprocesser som skapar den inelastiska signalen: phonon spridning, plasmon spridning och så kallade kärnnivåexcitationer. Det här arbetet fokusserar på simulationer av kärnnivåexcitationer där en elektron exciteras från en kärnnivå till ett fritt tillstånd i materialets bandstruktur. Hos elektroner som undergår en sådan inelastisk process visar deras fördelning över energierna en skarp kant där den inelastiska processen blir möjlig. I fackspråket kallas det för ”electron energy loss near-edge structures (ELNES)”.

Alla inelastiska signaler ger tillsammans information om flertalet egenskaper hos provmaterialet. Genom ELNES-kantens form och position kan materialets komposition och kemiska uppbyggnad bestämmas. Dessutom kan en magnetisk signal som kallas ”electron energy loss magnetic chiral dichroism (EMCD)” mätas; genom att subtrahera två ELNES-spektra som har mättes vid två särskilda detektorpositioner. EMCD utlovas att vara en teknik som kan användas till att mäta styrkan hos enkla atomers magnetism. Beräkningar och teoretiska resultat visar att det skulle vara möjligt att mäta denna signal, men det finns ännu inget publicerat framgångsrikt experiment där det har lyckats och frågan är om beräkningar kanske förenklar någon aspekt eller effekt som väsentligt minskar EMCD-signalen.

Det här arbetet försöker att hitta ett svar på frågan hur stor påverkan av olika så kallade multipol-övergånger på den teoretiska EMCD-signalen är. För att hitta ett svar så simuleras ELNES-kantor av bcc-järn och detta används sedan till att beräkna EMCD-signalen. Det här arbetet ger inget avgörande svar på påverkan av multipol-övergångar, men avslöjar att den experimentella rutinen som kallas post-edge normalisation tillsammans med ett annat, oförväntat tillskott påverkar EMCD-signalen starkare än multipol-övergångar. Post-edge regionen behöver mer forskning generellt eftersom dess skepnad inte matchar bra med experiment och att EMCD-signalen är väldigt känslig för post-edge regionen. Därför behövs det mer forskning om processer som skapar post-edge regionen.

Vågfunktioner är generellt komplexa tal i kvantmekaniken och de har därför en realdel och en imaginärdel. Nu är det så att imaginärdelen av kvantiteten som beskriver inelastiska ELNES-spridningen ger information om magnetismen och man kan genom att subtrahera ELNES-signaler frilägga imaginärdelen. Därefter antas att realdelen faller bort och resulterande signalen enbart kommer från imaginärdelen. Det oförväntade tillskottet antydar att detta antagande inte är helt korrekt och att realdelen visar någon form av asymmetri som påverkar EMCD-signalen väsentligt. Grunden för denna asymmetrien är oklar tillsvidare och det behövs mer forskning även här.

ACKNOWLEDGMENTS

I would like to express my deep gratitude to my supervisor Ján Rusz for his supervision on several projects in the past, countless very valuable discussions, and his immense patience with me. Apart from this thesis I am also thankful for the many opportunities and the support he offered me during the last three years. Furthermore I would like to thank him especially for all the evenings and weekends he spent reading my manuscripts, providing most helpful comments, and late night email replies. This thesis would not be possible without him. I really enjoy to work with you, Ján, and look forward to the coming years.

I cannot find words to express my gratitude to my family, my mother Kerstin and my father Robert in particular. I feel very much encouraged by their their love and support on whichever path I choose. Furthermore I have come to greatly appreciate their patience when they did not hear from me for a longer time and when I extended my studies. Further special gratitude goes to my sister Caren who continues to help me navigate the treacherous waters of family birthdays and gifts and continues to be one of my first-hand addresses in case I need advice. I am very lucky to have you as my sister, Caren!

Furthermore I was incredibly lucky to meet my love Vanda about a year ago. She has quickly become my complement, my support in times of doubt, and my ”partner in crime”. Thank you for sharing this life with me, Vanda!

I would furthermore like to thank Barbara, Noémie, Yuhang, and Viktor for great study companionship. For memorable climbs, dinners, times, or trips in my free time I would like to thank Emma, Florens, Henrik, Irene, James, Jannik, Josh, Kai, Karolína, Leandra, Lucia, Malin, Max, Noémie, Per, Reinier, Robert, Sebastian, Simon, Steph, Tor, and Yanis. A special thanks goes to my flatmate Åland for allowing me to live in his apartment and for many insightful discussions on programming, economics, philosophy and history. Another special thanks goes out to Staffan whose Injera developed into some sort of Monday tradition and is a source of great delight.

Contents

List of Figures vii
List of Tables xi
Physical constants xii
Acronyms xii
1 INTRODUCTION 1
2 THEORY OF ELNES AND EMCD 3
  2.1 Electron energy loss near-edge structures 3
    2.1.1 Inelastic Scattering and DDSCS 6
    2.1.2 Bloch waves and dynamical diffraction 7
    2.1.3 Electron energy-loss magnetic chiral dichroism . . . 11
    2.1.4 Evaluation of mixed dynamic form factor 16
3 ELECTRONIC STRUCTURE CALCULATION OF BCC-IRON 19
  3.1 Method of WIEN2K 19
  3.2 Computational details of the DFT simulation 21
4 SIMULATION METHOD 23
  4.1 Computational procedure for calculation of the DDSCS . . . 23
  4.2 Extraction of the EMCD-signal 26
    4.2.1 Spectral broadening 27
    4.2.2 Post-edge normalization 29
    4.2.3 Difference methods for EMCD extraction 30
  4.3 Extraction of the ratio of orbital and spin magnetic moment 31
5 SIMULATION RESULTS 33
  5.1 Simulated ELNES-spectra and EMCD-signals: General features 33
  5.2 Maps of the energy-integrated EMCD-signal 39
  5.3 Non-dipole contributions to the EMCD-signal 43
  5.4 Maps of the m_L/m_S-ratio 47
    5.4.1 m_L/m_S-ratio computed from pEMCD-signal 47
    5.4.2 m_L/m_S-ratio computed from eEMCD-signal 52
  5.5 Apparent anisotropy of the real part of the MDFF 58
6 CONCLUSION 62

REFERENCES 63
A APPENDIX 67
  A.1 Additional maps of the energy-integrated EMCD-signal . . . 68
  A.2 Additional m_L/m_S-maps 72
    A.2.1 pEMCD 72
    A.2.2 eEMCD 95
  A.3 Additional maps of the apparent anisotropy 111

List of Figures

Figure 2.1 Overview of commona features EELS-spectra. . . . 5

Figure 2.2 Schematic drawing of dynamical diffraction 8

Figure 3.1 Convergence of the DOS of bcc-iron with respect to the number of k-points N_k and $R_{\mathrm{MT}} K_{\mathrm{max}}$. 22

Figure 4.1 Convergence of the unbroadened DDSCS with respect to the Bloch wave cutoff P_{min} at the L_3-edge (subfigure (a)) and at the L_2-edge (subfigure (b)). These spectra are computed for a scattering angle of $(\theta_x, \theta_y) = (9.0, 9.0)$ and thickness 15 nm. 24

Figure 4.2 Visualization of the effect of spectral broadening on the calculated DDSCS. 28

Figure 5.1 ELNES-spectra and EMCD-signal measured by *Thersleff et al.* 34

Figure 5.2 Simulated spectra and extracted EMCD-signals in dipole-approximation @ 15 nm. 37

Figure 5.3 Simulated spectra and extracted EMCD-signals in lamb3-approximation @ 15 nm. 38

Figure 5.4 Maps of the energy-integrated pEMCD-signal @ 15 nm. 40

Figure 5.5 Maps of the energy-integrated eEMCD-signal @ 15 nm. 42

Figure 5.6 Energy-resolved contributions of the main cross terms to the eEMCD-signal @ 15 nm with applied post-edge normalization. 45

Figure 5.7 Energy-resolved contributions of the main cross terms to the eEMCD-signal @ 15 nm without post-edge normalization. 46

Figure 5.8 pEMCD-m_L/m_S-map @15 nm, dipole-term, double difference method, q-averaging range: similar to post-edge normalization range. 48

Figure 5.9 pEMCD-m_L/m_S-map @15 nm, 11-term, double difference method, q-averaging range: similar to post-edge normalization range. 49

Figure 5.10 pEMCD-m_L/m_S-map @15 nm, lamb3-approximation, double difference method, q-averaging range: similar to post-edge normalization range. 50

Figure 5.11 pEMCD-m_L/m_S-map @15 nm, lamb3-approximation, double difference method, q-averaging range: 745 eV to 750 eV. 51

Figure 5.12 eEMCD-m_L/m_S-map @15 nm, dipole-approximation, double difference method, q-averaging range: similar to post-edge normalization range. 54

Figure 5.13 eEMCD-m_L/m_S-map @15 nm, 11-term, double difference method, q-averaging range: similar to post-edge normalization range. 55

Figure 5.14 eEMCD-m_L/m_S-map @15 nm, lamb3-approximation, double difference method, q-averaging range: similar to post-edge normalization range. 56

Figure 5.15 eEMCD-m_L/m_S-map @15 nm, lamb3-approximation, double difference method, q-averaging range: 745 eV to 750 eV. 57

Figure 5.16 Maps of the absolute magnitude of the contributions to the energy-integrated eEMCD-signal, which are attributable to the real part of the MDFF @15 nm. 59

Figure 5.17 Maps of the edge-resolved relative strength of the contribution due to the real part of the MDFF to the energy-integrated eEMCD-signal @15 nm. 61

Figure A.1 Maps of the energy-integrated pEMCD-signal @ 10 nm. 68

Figure A.2 Maps of the energy-integrated pEMCD-signal @ 20 nm. 69

Figure A.3 Maps of the energy-integrated eEMCD-signal @ 10 nm. 70

Figure A.4 Maps of the energy-integrated eEMCD-signal @ 20 nm. 71

Figure A.5 pEMCD-m_L/m_S-map calculated in dipole approximation at thickness 10 nm using the double difference method and q-averaging range equals post-edge noarmalization range. 72

Figure A.6 pEMCD-m_L/m_S-map calculated in dipole approximation at thickness 20 nm using the double difference method and q-averaging range equals post-edge noarmalization range. 73

Figure A.7 pEMCD-m_L/m_S-map calculated for 11-term at thickness 10 nm using the double difference method and q-averaging range equals post-edge noarmalization range. 74

Figure A.8 pEMCD-m_L/m_S-map calculated for 11-term at thickness 20 nm using the double difference method and q-averaging range equals post-edge noarmalization range. 75

Figure A.9 pEMCD-m_L/m_S-map calculated for 11-term at thickness 10 nm using the double difference method and q-averaging range equals post-edge noarmalization range. 76
Figure A.10 pEMCD-m_L/m_S-map calculated for Rayleigh expansion up to third order at thickness 20 nm using the double difference method and q-averaging range equals post-edge noarmalization range. 77
Figure A.11 pEMCD-m_L/m_S-map calculated in dipole approximation at thickness 10 nm using the double difference method and q-averaging range 745 eV to 750 eV. . . 78
Figure A.12 pEMCD-m_L/m_S-map calculated in dipole approximation at thickness 15 nm using the double difference method and q-averaging range 745 eV to 750 eV. . . 79
Figure A.13 pEMCD-m_L/m_S-map calculated in dipole approximation at thickness 20 nm using the double difference method and q-averaging range 745 eV to 750 eV. . . 80
Figure A.14 pEMCD-m_L/m_S-map calculated for Rayleigh expansion up to third order at thickness 10 nm using the double difference method and q-averaging range 745 eV to 750 eV. 81
Figure A.15 pEMCD-m_L/m_S-map calculated in dipole approximation at thickness 15 nm using the double difference method and q-averaging range 745 eV to 750 eV. . . 82
Figure A.16 pEMCD-m_L/m_S-map calculated for Rayleigh expansion up to third order at thickness 20 nm using the double difference method and q-averaging range 745 eV to 750 eV. 83
Figure A.17 pEMCD-m_L/m_S-map calculated for Rayleigh expansion up to third order at thickness 10 nm using the double difference method and q-averaging range 745 eV to 750 eV. 84
Figure A.18 pEMCD-m_L/m_S-map calculated for Rayleigh expansion up to third order at thickness 20 nm using the double difference method and q-averaging range 745 eV to 750 eV. 85
Figure A.19 pEMCD-m_L/m_S-map calculated in dipole approximation at thickness 10 nm using the double difference method and q-averaging range 750 eV to 760 eV. . . 86
Figure A.20 pEMCD-m_L/m_S-map calculated in dipole approximation at thickness 15 nm using the double difference method and q-averaging range 750 eV to 760 eV. . . 87
Figure A.21 pEMCD-m_L/m_S-map calculated in dipole approximation at thickness 20 nm using the double difference method and q-averaging range 750 eV to 760 eV. . . 88

Figure A.22 pEMCD-m_L/m_S-map calculated in dipole approximation at thickness 10 nm using the double difference method and q-averaging range 750 eV to 760 eV. . . 89

Figure A.23 pEMCD-m_L/m_S-map calculated in dipole approximation at thickness 15 nm using the double difference method and q-averaging range 750 eV to 760 eV. . . 90

Figure A.24 pEMCD-m_L/m_S-map calculated in dipole approximation at thickness 20 nm using the double difference method and q-averaging range 750 eV to 760 eV. . . 91

Figure A.25 pEMCD-m_L/m_S-map calculated for Rayleigh expansion up to third order at thickness 10 nm using the double difference method and q-averaging range 750 eV to 760 eV. 92

Figure A.26 pEMCD-m_L/m_S-map calculated in dipole approximation at thickness 15 nm using the double difference method and q-averaging range 750 eV to 760 eV. . . 93

Figure A.27 pEMCD-m_L/m_S-map calculated for Rayleigh expansion up to third order at thickness 20 nm using the double difference method and q-averaging range 750 eV to 760 eV. 94

Figure A.28 eEMCD-m_L/m_S-map calculated in dipole approximation at thickness 10 nm using the double difference method. 95

Figure A.29 eEMCD-m_L/m_S-map calculated in dipole approximation at thickness 20 nm using the double difference method. 96

Figure A.30 eEMCD-m_L/m_S-map calculated for Rayleigh expansion up to third order at thickness 10 nm using the double difference method. 97

Figure A.31 eEMCD-m_L/m_S-map calculated for Rayleigh expansion up to third order at thickness 20 nm using the double difference method. 98

Figure A.32 eEMCD-m_L/m_S-map calculated in dipole approximation at thickness 10 nm using the right-left difference method. 99

Figure A.33 eEMCD-m_L/m_S-map calculated in dipole approximation at thickness 15 nm using the right-left difference method. 100

Figure A.34 eEMCD-m_L/m_S-map calculated in dipole approximation at thickness 20 nm using the right-left difference method. 101

Figure A.35 eEMCD-m_L/m_S-map calculated for Rayleigh expansion up to third order at thickness 10 nm using the right-left difference method 102

Figure A.36 eEMCD-m_L/m_S-map calculated for Rayleigh expansion up to third order at thickness 15 nm using the right-left difference method. 103
Figure A.37 eEMCD-m_L/m_S-map calculated for Rayleigh expansion up to third order at thickness 20 nm using the right-left difference method. 104
Figure A.38 eEMCD-m_L/m_S-map calculated in dipole approximation at thickness 10 nm using the up-down difference method. 105
Figure A.39 eEMCD-m_L/m_S-map calculated in dipole approximation at thickness 15 nm using the up-down difference method. 106
Figure A.40 eEMCD-m_L/m_S-map calculated in dipole approximation at thickness 20 nm using the up-down difference method. 107
Figure A.41 eEMCD-m_L/m_S-map calculated for Rayleigh expansion up to third order at thickness 10 nm using the up-down difference method. 108
Figure A.42 eEMCD-m_L/m_S-map calculated for Rayleigh expansion up to third order at thickness 15 nm using the up-down difference method. 109
Figure A.43 eEMCD-m_L/m_S-map calculated for Rayleigh expansion up to third order at thickness 20 nm using the up-down difference method. 110
Figure A.44 Maps of the absolute magnitude of the contributions to the energy-integrated eEMCD-signal attributable to the real part of the MDFF @10 nm. . . 111
Figure A.45 Maps of the absolute magnitude of the contributions to the energy-integrated eEMCD-signal attributable to the real part of the MDFF @20 nm. . . 112
Figure A.46 Maps of the edge-resolved relative strength of the contribution due to the real part of the MDFF to the energy-integrated eEMCD-signal @10 nm. 113
Figure A.47 Maps of the edge-resolved relative strength of the contribution due to the real part of the MDFF to the energy-integrated eEMCD-signal @20 nm. 114

List of Tables

Table 2.1 Comparison of the relativistic quantum numbers of the initial states of the L_2 and L_3-edge of the bcc-Fe. 16

PHYSICAL CONSTANTS

The following physical constants are used in the main text.

Name	**Symbol**	**Value**	**Relation**
Bohr radius	a_0	0.529×10^{-11} Å	$1\,a_0 = \frac{\hbar^2}{m_e e^2}$
Bohr magneton	μ_B	5.788×10^{-5} eV T^{-1}	$1\,\mu_B = \frac{e\hbar}{2m_e}$
Electron rest mass	m_e	$0.510\,998$ MeV c_0^{-2}	
Elementary charge	e	1.602×10^{-19} C	
Planck constant	h	4.136×10^{-15} eV s	
Reduced Planck constant	$\hbar$	6.582×10^{-16} eV s	$1\,\hbar = \frac{h}{2\pi}$
Rydberg unit of energy	Ry	13.605 eV	$1\,\text{Ry} = \frac{e^2}{2a_0}$
Speed of light in vacuum	c_0	$299\,792\,458$ m s^{-1}	

ACRONYMS

APW	augmented plane wave	19
BZ	Brillouin zone	21
CCD	charge-coupled device	3
DFF	dynamic form factor	6
DFT	density functional theory	18
DDSCS	double differential scattering cross section	1
DOS	density of states	5
DP	diffraction pattern	3
eEMCD	extracted EMCD	27
EELS	electron energy loss spectroscopy	1

ELNES	electron energy loss near-edge structures	1
EMCD	electron energy loss magnetic chiral dichroism	1
EVB	electron vortex beam	1
FT	fourier transform	8
HWHM	half width at half maximum	29
KSE	Kohn-Sham eigenvalue	20
LAPW	linearized augmented plane wave	19
LO	local orbital	20
MDFF	mixed dynamic form factor	3
MLD	magnetic linear dichroism	11
pEMCD	pure EMCD	27
PM	photomultiplier	3
SEQ	Schrödinger equation	10
STEM	scanning transmission electron microscope	1
TEM	transmission electron microscope	1
XANES	x-ray absorption near-edge structures	29
XMCD	x-ray magnetic circular dichroism	1
ZLP	zero loss peak	4

1

INTRODUCTION

By combining the high spatial resolution of modern transmission electron microscopes (TEMs) down to the atomic level while being element specific and accessible with more or less lab sized experimental equipment, electron energy loss magnetic chiral dichroism (EMCD) promises to be a powerful investigation technique for magnetic materials. EMCD was first theorized to be accessible in an interferometric electron energy loss spectroscopy (EELS) experiment by exploiting the properties of a special scattering geometry in 2003 [1]. In 2006 *Schattschneider et al.* demonstrated that it is feasible to extract a magnetic signal in the proposed experiment, which is similar in shape to the signal seen in x-ray magnetic circular dichroism (XMCD) [2]. In this experiment the magnetic signal is obtained by taking the difference of two electron energy loss near-edge structures (ELNES)-spectra of the L_2- and L_3-edges of Fe measured in said scattering geometry from a two-beam case of a systematic row of Bragg spots. However, the measured signal was found to be considerably weaker than a computer simulation predicted it to be.

Until today many successful EMCD measurements have been carried out: the technique has been extended to scanning transmission electron microscope (STEM) [3] and the resolution of the technique has been improved to the sub-nanometer regime by use of convergent beams and the *double difference method* [3–7]. In 2010 electron vortex beams (EVBs) were experimentally demonstrated [8] and they were predicted to enhance the EMCD-signal to allow for atomic resolution microscopy of the magnetic state of materials [9]. In the case of EVBs a successful EMCD measurement is yet to be reported and this discrepancy between theory and experiment leads naturally to the question if the experimental setup is to be improved or if there are certain effects that are not properly considered in the simulations. One such possible effect are non-dipole transitions since most of the published results from simulations of EMCD were carried out in a convenient and computationally less expensive *dipole approximation*. As it will become clear in section 2.1.1 the dipole approximation amounts to a Taylor expansion of an exponential in the expression for the double differential scattering cross section (DDSCS) according to

$$e^{i\mathbf{q}\cdot\mathbf{R}} = 1 + i\mathbf{q}\cdot\mathbf{R} + \mathcal{O}(2), \tag{1.1}$$

i.e. only terms up to the first order are taken into account. This approach is justified as long as the argument of the exponential is small. In ELNES, however, one has often situations where $\mathbf{q}\cdot\mathbf{R} \approx 1$. Theoretical results, however, show that the dipole approximation gives reasonable results in 3d-ferromagnetic systems [10]. A more accurate, yet computationally more demanding, treatment of said exponential factor is based on the *Rayleigh expansion*, i.e.

$$e^{i\mathbf{q}\cdot\mathbf{R}} = 4\pi \sum_{\lambda=0}^{\infty} \sum_{\mu=-\lambda}^{\lambda} i^{\lambda} Y_{\lambda}^{\mu}(\mathbf{q}/q) Y_{\lambda}{}^{\mu} * (\mathbf{R}/R) j_{\lambda}(qR), \tag{1.2}$$

where Y_{λ}^{μ} are spherical harmonics and j_{λ} spherical Bessel functions.

As the title suggests the outset for the present work was to investigate the role of non-dipole transitions on the EMCD-signal obtained from ELNES-spectra simulations. In order to do so, ELNES-spectra of the L_2- and L_3-edge of bcc-Fe need to be simulated in dipole approximation and up to some order of the Rayleigh expansion, which is a computationally expensive task. These theoretical spectra, however, allow at the same time for further investigations on the influence of certain experimental technicalities such as the post-edge normalization range, the chosen difference method for EMCD-extraction, and the detector position.

This work is structured into 4 chapters: A description of the theoretical framework of the computational method used to simulate ELNES-spectra is given in chapter 2. Chapter 3 describes thereafter the method and results of the electronic structure calculation of the ground state of bcc-Fe. Chapter 4 is dedicated to the description of the method used to simulate the required ELNES-spectra and other computational or procedural details. Chapter 5 deals with the analysis od the results and their discussion. Final conclusions are drawn in chapter 6.

2

THEORY OF ELNES AND EMCD

This chapter is dedicated to a brief overview of the necessary theory required to understand the simulations performed in this work. Section 2.1 contains a brief introduction into the concept of ELNES. The remainder of this chapter will deal with a description of the theoretical concepts and equations needed in order to calculate ELNES-spectra: First an overview of the theoretical concepts of inelastic electron scattering and the mixed dynamic form factor (MDFF) are given in section 2.1.1. The theory of Bloch waves and dynamical diffraction is briefly developed in section 2.1.2 and section 2.1.3 uses these concepts to motivate the idea behind EMCD. Finally an expression used for the calculation of the mixed dynamic form factor (MDFF) is given in section 2.1.4.

2.1 ELECTRON ENERGY LOSS NEAR-EDGE STRUCTURES

This section gives a qualitative introductory overview of the physics of ELNES and motivates the following more mathematical sections. It summarizes some of the key aspects of chapters 4, 38 and 39 of the book by *Williams and Carter* [11].

The transmission electron microscope (TEM) is a powerful yet complicated device for the investigation of material properties. In a TEM so-called fast electrons of kinetic energy of typically 60-300 keV produced by an electron gun are focused onto a specimen using electron optical lenses. For thin enough specimen the electrons pass through it as the ”T” in in the abbreviation ”TEM” emphasizes. A fraction of the electrons in the beam interacts with the electronic structure and nuclei of the specimen via elastic and inelastic scattering processes. Using another set of electron lenses in the beam line of the microscope and behind the specimen, it is possible to form either a diffraction pattern (DP) or image of the specimen in the detector plane of the instrument. A scintillator-photomultiplier (PM) tube or charge-coupled device (CCD) camera is located in the detector plane behind the sample in order to detect the scattered electrons and thus record the formed image or DP. The electron optics of a TEMs can be adjusted to produce a variety of different beam types, such as more conventional parallel beams and convergent beams, but eventually also more complex ones such as electron vortex beams (EVBs) [9, 12].

Imaging and diffraction are the classical core functions of a TEM. Inelastic processes, however, generate a wealth of additional signals that require the TEM to be outfitted with specialized hardware: on one hand one has *secondary signals*, such as x-rays and secondary electrons, and on the other hand electron energy loss spectroscopy (EELS), i.e. the analysis of the energy spectrum of the scattered beam electrons. The EELS-signal can be measured experimentally using a magnetic-prism spectrometer.

The beam electrons do not experience a change in their energy in an elastic scattering event. Examples of elastic scattering are *Rutherford scattering* of electrons on nuclei and *Bragg scattering* observed for crystalline specimen. The beam electrons in a TEM scatter mainly elastically on the specimen's nuclei since the large difference in mass between an electron and a nucleus reduces the energy transfer to basically zero. Bragg scattering occurs due to elastic electron scattering on crystal planes and similar to x-rays, electrons can be used to form DPs of the specimen, which allow for the investigation of its crystal structure. The formation of these DPs is in comparison with x-rays much more complicated due to the electrons' stronger interaction with matter: in the case of x-rays the scattering process can often be simplified to single elastic scattering which allows in turn for good prediction of the intensity of Bragg spots. DPs formed in a TEM on the other hand exhibit so-called *pendellösung*-oscillations as a result of plural or multiple elastic scattering on the lattice planes of the specimen, called *dynamical diffraction*. These oscillations are effectively (periodic) variations in the intensity of Bragg spots due to changes of the thickness of the specimen. Dynamical diffraction is one of the reasons why the interpretation of TEM images requires often the comparison to the results of image simulations as there is no simple mathematical expression to account for it.

In contrast one describes a process as inelastic scattering if the scattering object experiences a change in its energy. There exists a multitude of different interactions with the specimen which form the inelastic part of EELS spectra but they all have in common that they are somewhat related to the electronic structure of the specimen. Without going into too much detail, *Williams and Carter* group them into three major groups [11, p. 54]: processes that generate x-rays, processes that generate other (secondary) electrons, and processes that result from collective interactions with many electrons or atoms. All these processes produce valuable secondary signals that can be analyzed with different tools such as x-ray and Auger electron spectrometers. In EELS, however, one detects the beam electrons after their interaction with the specimen and analyzes the information carried in their energy-loss spectrum.

In figure 2.1 an example EELS spectrum is depicted and features of some of the aforementioned processes are indicated: at zero energy loss the spectrum shows the so-called zero loss peak (ZLP), which is by far the strongest signal in the spectrum. The ZLPs is formed by mainly elastically scattered electrons and these electrons can be used to enhance contrast and resolution of TEM images [11, p. 702]. The second strongest contribution to the spectrum in figure 2.1 stems from the so-called plasmon peak(s) at low energy losses. Plasmons are collective excitations of almost free electrons in the valence and conduction band. For thin specimen only one plasmon peak is observed due the low probability for plural scattering. However as the thickness increases, the intensity of the plasmon peak increases because of the greater

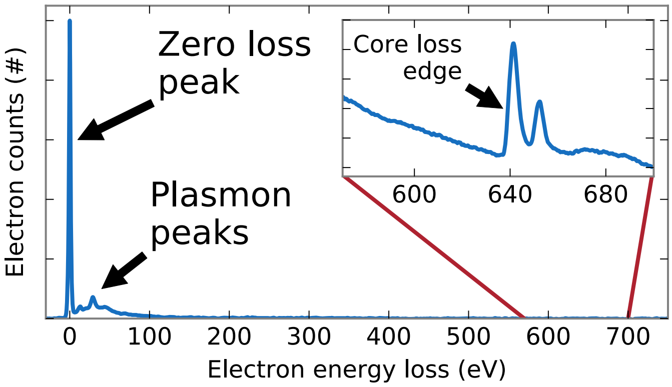

Figure 2.1: Schematic overview of the features commonly seen in EELS spectra. Modified reprint of the original figure uploaded by Wikipedia user Magnunor [13].

probability of scattering and further peaks appear due to plural scattering [14].

At energy losses of more than about 50 eV one often speaks of high energy loss spectra and the signal of interest in this regime stems from ionization edges, i.e. core-loss processes, where tightly bound electrons are excited from core-shells into the conduction band. The sharp onset of the edges gives them their name and is due to the quantization of atomic energy levels and the conservation of energy: at the onset energy the beam electron have lost just enough energy to excite a core-electron to the lower edge of the conduction band, right above the Fermi-energy. The energy-loss, at which the ionization edges appear, is element specific and allow thus for the analysis of the elemental composition of the specimen. The ionization edges are, however, superimposed on a rapidly decreasing background which is due to random plural plasmon scattering. The background is often assumed to follow a simple power law of the form [11, p. 726]

$$I = A \cdot E^{-r}, \tag{2.1}$$

where A and r are fitting parameters and E is the energy loss.

The term electron energy loss near-edge structures (ELNES) describes the EELS spectrum close to these ionization edges, which contains information on the unoccupied density of states (DOS) of the specimen. The investigations carried out in this work focus solely on results from simulated ELNES-spectra of bcc-Fe which governs the rest of this chapter.

The calculation of ELNES spectra can generally be thought of as a 4 step process: first the ground state electronic structure of the specimen's atoms including their core-electrons and the unoccupied DOS need to be calculated. Next the beam electron's wave function at the sites of the target atoms needs to be computed, followed by the calculation of the transition matrix elements between initial and final states of the target atoms. Finally the electron's wave function needs to be ”propagated” to the detector. In the following sections this process will be described in more detail.

2.1.1 *Inelastic Scattering and DDSCS*

The so-called double differential scattering cross section (DDSCS) $\frac{\partial^2\sigma}{\partial\Omega\partial E}$ is the key quantity that needs to be computed in order to simulate ELNES-spectra. It quantifies the probability that an electron, which lost an energy E as a result of inelastic scattering, is scattered towards the (infinitesimal) solid-angle $\mathrm{d}\Omega$. Experimentally the integrated DDSCS,

$$\frac{\partial\sigma}{\partial E} = \int_\Omega \frac{\partial^2\sigma}{\partial\Omega\partial E}\,\mathrm{d}\Omega\,, \tag{2.2}$$

is proportional to the energy-loss loss spectrum recorded by a detector covering the scattering angle Ω.

Thin specimen justify a first-order Born or single scattering approximation of the inelastic scattering event. The incident electron is in this approximation idealized to undergo only one core loss event and the DDSCS for inelastic scattering of a fast incident electron described by a plane wave with initial wave vector $\boldsymbol{\chi}_i$ into a plane wave with wave vector $\boldsymbol{\chi}_f$ on a core-electron in the initial state $|i\rangle$ reads [10, 15]

$$\frac{\partial^2\sigma}{\partial\Omega\partial E} = \frac{4\gamma^2}{a_0^2}\frac{\chi_f}{\chi_i}\frac{S(\mathbf{q},E)}{q^4}, \tag{2.3}$$

where $\gamma = 1/\sqrt{1-(v/c)^2}$ is a relativistic factor correcting the mass of the electron with velocity v, $\mathbf{q} = \boldsymbol{\chi}_i - \boldsymbol{\chi}_f$ is the momentum transfer in the scattering process and

$$S(\mathbf{q},E) = \sum_{i,f}\left|\langle f|e^{i\mathbf{q}\cdot\hat{\mathbf{R}}}|i\rangle\right|^2 \delta(E_i - E_f + E) \tag{2.4}$$

is the so-called dynamic form factor (DFF). $\hat{\mathbf{R}}$ is the position operator of the target electron and $|f\rangle$ is its final state. The transition matrix element $f(\mathbf{q}) = \langle f|e^{i\mathbf{q}\cdot\hat{\mathbf{R}}}|i\rangle$ is also called *form factor*. Here and in the following low temperatures will be assumed such that the Fermi-Dirac distribution governing the occupancy of initial and final states can be approximated by a step function. The sum over initial states, first appearing in equation 2.4, is then only to be taken over occupied states and the sum over final states only over unoccupied states.

In dipole approximation only the linear term in the Taylor expansion of the exponential factor is kept according to equation (1.1) and equation (2.3) becomes thus

$$S_{\text{dipole}}(\mathbf{q},E) = \sum_{i,f}\left|\langle f|\mathbf{q}\cdot\hat{\mathbf{R}}|i\rangle\right|^2 \delta(E_i - E_f + E). \tag{2.5}$$

This equation will be used to motivate the idea behind the first EMCD experiment.

The information about the phase of the form factor $f(\mathbf{q})$ is lost in the DDSCS according to (2.3) which leads to the so-called phase-problem in diffraction experiments. *Kohl and Rose* derived an expression for the DDSCS in an experiment, in which the incident wave is a coherent superposition $ue^{i\mathbf{k}} + ve^{i\mathbf{k}'}$ of two plane waves with wave vectors $\mathbf{k}$ and $\mathbf{k}'$, which can be thought of as being generated by a biprism [16]. The DDSCS reads then [1]

$$\frac{\partial^2\sigma}{\partial\Omega\partial E} = \frac{4\gamma^2}{a_0^2}\frac{k_f}{k_i}\left[|u|^2\frac{S(\mathbf{q},\mathbf{q},E)}{q^4} + |v|^2\frac{S(\mathbf{q}',\mathbf{q}',E)}{q'^4}\right. \tag{2.6}$$

$$\left. + 2\frac{\Re\{uv^* S(\mathbf{q},\mathbf{q}',E)\}}{q^2q'^2}\right], \tag{2.7}$$

where $\mathbf{q} = \mathbf{k}_i - \mathbf{k}_f$ and $\mathbf{q}' = \mathbf{k}_i' - \mathbf{k}_f$, i.e. both incoming plane waves are scattered in the same direction $\mathbf{k}_f$, and the dynamic form factor of equation 2.3 is generalized to the so-called mixed dynamic form factor (MDFF)

$$S(\mathbf{q},\mathbf{q}',E) = \sum_{i,f} \langle i|e^{i\mathbf{q}\cdot\hat{\mathbf{R}}}|f\rangle \langle f|e^{-i\mathbf{q}'\cdot\hat{\mathbf{R}}}|i\rangle\, \delta(E_i - E_f + E). \tag{2.8}$$

For $\mathbf{q} = \mathbf{q}'$ one notes that the MDFF reduces to the DFF of equation 2.4. In dipole approximation the MDFF becomes

$$S_{\text{dipole}}(\mathbf{q},\mathbf{q}',\mathrm{E}) = \sum_{i,f} \langle i|\mathbf{q}\cdot\hat{\mathbf{R}}|f\rangle \langle f|\mathbf{q}'\cdot\hat{\mathbf{R}}|i\rangle\, \delta(E_i - E_f + E). \tag{2.9}$$

It shall be noted here for reference purposes that the MDFF satisfies always

$$S(\mathbf{q},\mathbf{q}',E) = S^*(\mathbf{q}',\mathbf{q},E). \tag{2.10}$$

as one sees from equation (2.8) and it furthermore satisfies [2]

$$S(\mathbf{q},\mathbf{q}',E) = S(-\mathbf{q},-\mathbf{q}',E), \text{ if the system has an inversion center} \tag{2.11}$$

$$S(\mathbf{q},\mathbf{q}',E) = S(-\mathbf{q}',-\mathbf{q},E), \text{ if time-reversal symmetry holds.} \tag{2.12}$$

As a byproduct of these equations one finds that if both symmetries hold, the MDFF becomes a real quantity.

Equation 2.7 reminds qualitatively of the expression for the intensity in a double slit experiment, where the last term is the interference term. It depends on the relative phase of the two incoming waves and it should be possible to extract the phase information from the DDSCS in a suitable experiment. In section 2.1.3 it will be described how a magnetic field can give rise to an imaginary part of the MDFF which in turn leads to a dichroic signal known as EMCD. The following section deals with a description of the effects of the crystal symmetry.

2.1.2 *Bloch waves and dynamical diffraction*

Crystals are highly symmetric and periodic assemblies of atoms. In theory one idealizes them often to be infinitely periodic which is a good approximation in many cases. The crystal symmetry is conveniently described by defining a unit cell of the crystal structure, which is infinitely often repeated in

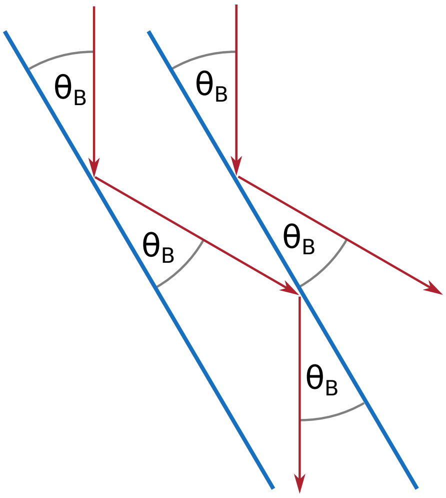

Figure 2.2: Schematic drawing of the fundamental process of dynamical diffraction: If an electron wave is scattered under the Bragg angle θ_B on a lattice plane (blue colored), there is a high probability of subsequent scattering under the Bragg angle θ_B on an adjacent lattice plane, which effectively reverses the first scattering event. As a result of such a double scattering the electron is still part of the direct, unscattered beam. Note that the angles are greatly exaggerated for clarity of presentation.

all spatial directions to form the crystal. The repetition is described in terms of the so-called *direct lattice* $\mathbf{R}_{pqr} = p\mathbf{a} + q\mathbf{b} + r\mathbf{c}$. Here the so-called *direct lattice vectors* $\mathbf{a}$, $\mathbf{b}$, and $\mathbf{c}$ are used and p, q, and r are integers. The direct lattice vectors satisfy in a cubic crystal structure such as bcc

$$a = |\mathbf{a}| = |\mathbf{b}| = |\mathbf{c}|, \qquad \mathbf{a} \perp \mathbf{b} \perp \mathbf{c}, \tag{2.13}$$

where a, b, and c are the direct lattice parameters. The direct lattice is accompanied by the so-called *reciprocal lattice*, which is essentially the fourier transform (FT) of the direct lattice. The reciprocal lattice vectors $\mathbf{a}^*$, $\mathbf{b}^*$, and $\mathbf{c}^*$ satisfy for a cubic crystal structure

$$a^* = |\mathbf{a}^*| = |\mathbf{b}^*| = |\mathbf{c}^*| = \frac{2\pi}{a}, \tag{2.14}$$

$$\mathbf{a}^* \parallel \mathbf{a}, \quad \mathbf{b}^* \parallel \mathbf{b}, \quad \mathbf{c}^* \parallel \mathbf{c} \quad \Longrightarrow \quad \mathbf{a}^* \perp \mathbf{b}^* \perp \mathbf{c}^*. \tag{2.15}$$

Points in the reciprocal lattice are indexed by the integer Miller-indices (hkl), which describes the direction of the normal $\mathbf{g}_{hkl} = h\mathbf{a}^* + k\mathbf{b}^* + l\mathbf{c}^*$ of a set of lattice planes in the crystal structure. After introducing the concepts of the direct and reciprocal lattices the focus is now shifted towards the process of elastic electron scattering in crystals.

An electron wave incident on a crystal is elastically scattered on the crystal lattice planes and the constructive interference of the scattered waves creates a characteristic spot pattern, the diffraction pattern (DP). The position of the spots in the DP is governed by the *Laue condition*, which states that resonant elastic scattering occurs inside a crystal for scattering vectors $\Delta\mathbf{k} = \mathbf{k}_\mathrm{o} - \mathbf{k}_\mathrm{i}$, which satisfy

$$\mathbf{a} \cdot \Delta\mathbf{k} = 2\pi h \tag{2.16}$$

$$\mathbf{b} \cdot \Delta\mathbf{k} = 2\pi k \tag{2.17}$$

$$\mathbf{c} \cdot \Delta\mathbf{k} = 2\pi l. \tag{2.18}$$

$\mathbf{k}_\mathrm{i}$ is thereby the wave vector of the incoming electron wave and $\mathbf{k}_\mathrm{o}$ the wave vector of the outgoing electron wave. The Laue condition states thus that $\Delta\mathbf{k} = \mathrm{g}_{hkl} = h\mathbf{a}^* + k\mathbf{b}^* + l\mathbf{c}^*\mathbf{g}$, i.e. $\Delta\mathbf{k}$ is a vector of the reciprocal lattice. The spots in a DP can therefore be labeled by the Miller-indices (hkl) of the reciprocal lattice and they are often called *Bragg spots* since one can show that the Laue condition is equivalent to the Bragg condition [17, pp. 99-100]

$$2d\sin(\theta_\mathrm{B}) = n\lambda, \tag{2.19}$$

where d is the distance between lattice planes, θ_B the *Bragg angle*, λ the wave length and n an integer. Pictorially a Laue peak for a given scattering vector $\Delta\mathbf{k}$ corresponds to a Bragg peak for the reflection off a lattice plane perpendicular to $\Delta\mathbf{k}$ under Bragg angle θ_B[17, pp. 100]. The Laue condition motivates the picture of the crystal as a beam splitter: the intensity of a Bragg spot is basically the square modulus of a plane wave component of the final wave function exiting the crystal in the direction of the Bragg spot, i.e. the intensity of a beam split off by the crystal.

The description of elastic scattering is not complete with this suggestive image, however. The elastic electron scattering cross section is considerably larger than the inelastic scattering cross section and even in thin specimen strong multiple elastic scattering occurs [11]. It thus does not suffice to consider only the 1st-order Born approximation, i.e. only single elastic scattering. Instead one needs to take into account so-called *dynamical diffraction*. The basic process behind dynamical diffraction is depicted in figure 2.2: the large elastic scattering cross section of electrons causes a considerable fraction of the incident electron beam to be scattered into diffracted beams characterized by their Miller-indices (hkl) after passing through just a few Å of the sample. These diffracted beams can easily be scattered again on the crystal's lattice planes since their angle of incidence is exactly the Bragg angle θ_B. In this way a scattered beam can be scattered again into the direct beam $\mathbf{0}$ or a different scattered beam $(h'k'l')$. The most striking feature of dynamical diffraction are periodic thickness-dependent intensity variations of Bragg spots known as *Pendellösung* [11].

After motivating the process of dynamical diffraction the remainder of this section is dedicated to the (brief) description of the mathematical framework used to simulate dynamical diffraction.

The beam electron's wave function incident on a crystal, however, does not necessarily satisfy the symmetry of the crystal potential and is thus not an eigenstate of the crystal Hamiltonian. A better description of the wave function $\Psi(\mathbf{r})$ is obtained if it is expanded into a set of Bloch waves $b_j\left(\mathbf{k}_j, \mathbf{r}_j\right)$, which satisfy the crystal's periodicity by construction [18, p. 118-120]. The expansion of the electron wave function reads inside the crystal

$$\Psi(\mathbf{r}) = \sum_j \epsilon_j b_j \left(\mathbf{k}_j, \mathbf{r}_j\right) \tag{2.20}$$

$$b_j \left(\mathbf{k}_j, \mathbf{r}_j\right) = e^{i\mathbf{k}_j \cdot \mathbf{r}} \sum_{\mathbf{g}} C_{\mathbf{g}}^{(j)} e^{i(\mathbf{k}_j - \mathbf{g}) \cdot \mathbf{r}}, \tag{2.21}$$

where $\mathbf{k}_j$ is the wave vector of the j-th Bloch wave and ϵ_j is an expansion coefficient determining the excitation strength of the j-th Bloch wave. $C_{\mathbf{g}}^{(j)}$ are Bloch coefficients. The incident wave function is taken to be a single plane wave,

$$\Psi_{\mathrm{i}}(\mathbf{r}) = e^{i\boldsymbol{\chi}_{\mathrm{in}} \cdot \mathbf{r}}, \tag{2.22}$$

where $\boldsymbol{\chi}_{\mathrm{i}}$ is the incident wave vector outside the crystal. The z-axis is from here on chosen to be parallel or anti-parallel to the direction of the incident beam and the entrance surface of the crystal is chosen to be parallel to the x-y-plane and intersect with the z-axis at $z = t_0$. The wave functions in- and outside the crystal and their derivatives need to be continuous on the entrance surface of the electron beam. This requirement constraints the Bloch wave vectors to read [10, 18]

$$\mathbf{k}_j = \boldsymbol{\chi}_{\mathrm{in}} + \gamma^{(j)} \mathbf{n}, \tag{2.23}$$

where $\mathbf{n}$ is a unit vector normal to the entrance surface. This shows that the x- and y-component of the wave vector are continuous and only the z-component may change by a small value $\gamma^{(j)}$ due to the difference in the potential inside and outside the crystal. This boundary condition fixes the value of the excitation coefficient [10]

$$\epsilon_j = C_{\mathbf{0}}^{(j)*} e^{-i\gamma^{(j)} t_0}. \tag{2.24}$$

The star (*) signals here complex conjugation. Inserting this into equation (2.20) and rewriting $\mathbf{k}_j$ according to equation (2.23) the wave function inside the crystal becomes

$$\Psi(\mathbf{r}) = \sum_{j\mathbf{g}} C_{\mathbf{0}}^{(j)*} C_{\mathbf{g}}^{(j)} e^{i\gamma^{(j)}(\mathbf{n} \cdot \mathbf{r} - t_0)} e^{i(\boldsymbol{\chi}_{\mathrm{in}} + \mathbf{g}) \cdot \mathbf{r}}. \tag{2.25}$$

Among others, *Rusz et al.* [10] describe how the Schrödinger equation (SEQ) is solved inside the crystal in the high energy limit in order to obtain the wave vector changes $\gamma^{(j)}$ and the Bloch coefficients $C_{\mathbf{g}}^{(j)}$ as the eigenvalues and the components of the eigenvectors of a linear eigenvalue problem, respectively [18].

It should be noted that equation (2.25) mathematically includes the effect of dynamical diffraction: the exponential term is periodic in the product $\mathbf{n} \cdot \mathbf{r}$, which is the thickness, at which the wave function is evaluated. This shows that the contribution of a term corresponding to a certain vector of the reciprocal lattice **g** reciprocal lattice (a beam) is strongly thickness dependent, which leads to the *Pendellösung*-oscillations in the diffraction pattern.

The last topic in this section concerns the so-called *systematic row approximation*: by tilting a specimen inside the TEM one can select to a certain degree, which Bloch waves are strongly excited. This is understood by considering the geometry of the *Ewald sphere* and how it intersects points in the reciprocal lattice. Tilting the incoming beam with respect to the reciprocal lattice changes, which and how many points the Ewalds sphere intersects. Since only reciprocal lattice points, which lie on the Ewald sphere, are visible in a diffraction pattern, the tilt can be used to suppress reflections. Two cases are important for the measurement of EMCD: the so-called *two-beam case* and the *three-beam* case. In the two-beam case only the direct beam $\mathbf{0} = \mathbf{g}_{000}$ and the beam associated with a selected reciprocal lattice vector $+\mathbf{G} \equiv \mathbf{g}_{hkl}$ are visible. A three-beam case DP on the other hand shows three excited reciprocal lattice points or beams: $-\mathbf{G} \equiv \mathbf{g}_{\bar{h}\bar{k}\bar{l}}$, $\mathbf{0}$ and $+\mathbf{G}$.

In the next section the phenomenon of EMCD is explained by drawing from the concepts developed in this section.

2.1.3 *Electron energy-loss magnetic chiral dichroism*

The momentum transfer $\mathbf{q}$ in inelastic electron scattering plays an analogous role to the polarization vector $\boldsymbol{\varepsilon}$ in x-ray absorption spectroscopy and besides EMCD, magnetic linear dichroism (MLD) has been demonstrated as well in EELS [1, 2, 19, 20]. In XMCD-measurements the difference in absorption of left- and right-circularly polarized x-ray photons allows to probe the spin-dependent unoccupied density of states of magnetic materials. The question is, however, how this concept can be carried over to inelastic electron scattering since electrons do not have a polarization: it turns out that circular polarization is replaced by the concept of ”chirality” in EMCD as it is motivated below.

Circularly polarized light is a superposition of two linearly polarized plane waves with polarization vectors $\boldsymbol{\varepsilon}$ and $\boldsymbol{\varepsilon}'$ and resulting polarization vector $\boldsymbol{\varepsilon} \pm i\boldsymbol{\varepsilon}'$, which satisfy

$$\boldsymbol{\varepsilon} \perp \boldsymbol{\varepsilon}', \qquad |\boldsymbol{\varepsilon}| = |\boldsymbol{\varepsilon}'| \tag{2.26}$$

i.e. the polarization vectors are orthogonal and the phase of the plane waves differs by $\frac{\pi}{2}$. If one naively replaces the momentum transfer $\mathbf{q}$ by the chiral momentum transfer $\mathbf{q} \pm i\mathbf{q}'$, equation (2.5) becomes

$$\sum_{i,f}\Big[\left|\langle i|\mathbf{q}\cdot\hat{\mathbf{R}}|f\rangle\right|^2 + \left|\langle i|\mathbf{q}'\cdot\hat{\mathbf{R}}|f\rangle\right|^2 \\ \pm 2\Im\left\{\langle i|\mathbf{q}\cdot\hat{\mathbf{R}}|f\rangle\,\langle f|\mathbf{q}'\cdot\hat{\mathbf{R}}|i\rangle\right\}\Big]\delta(E_i - E_f + E). \tag{2.27}$$

This result is effectively the DDSCS of equation (2.7) in dipole approximation of the MDFF according to equation (2.9) for $u = 1$ and $v = \pm i$. One notices further that the difference of the DDSCS for right- and left- chirality ($\nu = i$ and $\nu = -i$, respectively) gives access to the imaginary part of the MDFF, i.e.

$$\begin{aligned}\left[\frac{\partial^2\sigma}{\partial\Omega\partial E}\right]^{\nu=i}_{\text{dipole}} - \left[\frac{\partial^2\sigma}{\partial\Omega\partial E}\right]^{\nu=-i}_{\text{dipole}} \\ = 4\sum_{i,f} \Im\Big\{\langle i|\mathbf{q}\cdot\hat{\mathbf{R}}|f\rangle\,\langle f|\mathbf{q}'\cdot\hat{\mathbf{R}}|i\rangle\Big\}\delta(E_i - E_f + E) \\ = 4\Im\Big\{S_{\text{dipole}}(\mathbf{q},\mathbf{q}',E)\Big\} \qquad (2.28)\end{aligned}$$

and thus a dichroic effect appears by changing the chirality of the electron beam.

The physics of EMCD is, however, more subtle than this naive replacement suggests. If one recalls the physical situation for which (2.7) is derived, one notes that the incident wave is a coherent superposition of two plane waves of differing wave vectors $\mathbf{k}_i$ and $\mathbf{k}_i'$ which are scattered towards the same direction $\mathbf{k}_f$. The equivalence of equations (2.27) and (2.9) in dipole approximation for $a = 1$ and $b = \pm i$ suggests that one can observe the ELNES-equivalent of XMCD in the interference term of the scattering cross section of a coherent super position of plane waves. For closest similarity to XMCD one should setup the experiment such that $|\mathbf{q}| = |\mathbf{q}'|$, i.e., one studies the EMCD equivalence of circular polarization and not the equivalent of elliptical polarization.

It needs to be stressed at this point, however, that none of these conditions need to be strictly satisfied for the observation of EMCD, as the presence of a dichroic signal is connected to a non-vanishing imaginary part in the MDFF as equation (2.28) illustrates. This can be understood further by rewriting the MDFF in dipole approximation according to

$$\begin{aligned}S_{\text{dipole}}(\mathbf{q},\mathbf{q}',E) &= \sum_{i,f}\langle i|\mathbf{q}\cdot\hat{\mathbf{R}}|f\rangle\,\langle f|\mathbf{q}'\cdot\hat{\mathbf{R}}|i\rangle\,\delta(E_i - E_f + E) \\ &= \mathbf{q}T(E)\mathbf{q}', \qquad (2.29)\end{aligned}$$

where $T(E)$ is a complex 3×3 matrix. As such it can be written as

$$T(E) = R(E) + iI(E), \qquad (2.30)$$

$R(E) = \Re\{T(E)\}$ and $I(E) = \Im\{T(E)\}$, i.e., as a sum of its real and imaginary part. Since the MDFF satisfies equation (2.10) it follows that $R(E)$ is a real symmetric and $I(E)$ is a real antisymmetric matrix. One notes here that the imaginary part of the MDFF explicitly carries the notion of anisotropy with respect to the momentum transfer, since its trace is zero and only off-diagonal elements are non-zero. Inserting equation (2.30) into equation (2.29) and explicitly performing the matrix multiplications in the imaginary part,

$$\begin{aligned}\mathbf{q}I(E)\mathbf{q}' &= \begin{pmatrix} q_x \\ q_y \\ q_z \end{pmatrix} \begin{pmatrix} 0 & I_{xy}(E) & I_{xz}(E) \\ -I_{xy}(E) & 0 & I_{yz}(E) \\ -I_{xz}(E) & -I_{yz}(E) & 0 \end{pmatrix} \begin{pmatrix} q'_x \\ q'_y \\ q'_z \end{pmatrix} \\ &= \left[\begin{pmatrix} q_x \\ q_y \\ q_z \end{pmatrix} \times \begin{pmatrix} q'_x \\ q'_y \\ q'_z \end{pmatrix} \right] \cdot \begin{pmatrix} I_{yz}(E) \\ I_{xz}(E) \\ I_{xy}(E) \end{pmatrix}, \end{aligned} \tag{2.31}$$

one can identify the off-diagonal terms of the imaginary part $I(E)$ with a cross product of the momentum transfers. Equation (2.29) reads then

$$\mathbf{q}T(E)\mathbf{q}' = \mathbf{q}R(E)\mathbf{q}' + i(\mathbf{q} \times \mathbf{q}') \cdot \mathbf{m}(E), \tag{2.32}$$

where $\mathbf{m}(E) = (I_{yz}(E), I_{xz}(E), I_{xy}(E))^T$ carries information about the magnetic moment of the target atom. This is not a clean derivation why the imaginary part of the MDFF is connected to the magnetic moment and a qualitative motivation shall suffice at this point: as noted in section 2.1.1 the MDFF has only an imaginary part if time-reversal or inversion symmetry breaking occurs. In a cubic crystal such as bcc-iron inversion symmetry is not broken and thus time-reversal symmetry needs to be broken in order to observe an imaginary part. Note that this is the case in the presence of magnetic fields and the interested reader can find a more detailed discussion in the work of *Schattschneider et al.* [2, 4] and included references.

Equation (2.32) has a useful form for discussing the geometry used to measure EMCD: in a TEM the sample is subject to a strong magnetic field along the optical axis of the instrument, which stems from the electron optical lenses. This field acts on the atomic magnetic moments and in the case of a ferromagnet such as bcc-iron all magnetic moments align in the same direction, parallel to the magnetic field lines. Choosing the optical axis of the microscope along the z-axis $\mathbf{m}(E)$ aligns parallel to the z-axis too. In this case the imaginary part of the MDFF in dipole approximation becomes

$$\Im\{S_{\text{dipole}}(\mathbf{q}, \mathbf{q}', E)\} = (\mathbf{q} \times \mathbf{q}') \cdot \mathbf{m}(E) = (q_x q'_y - q_y q'_x) m_z(E). \tag{2.33}$$

Note that only the x- and y-components of the momentum transfers $\mathbf{q}$ and $\mathbf{q}'$ are of concern in obtaining an EMCD-signal in this geometry. Observe furthermore how the sign of the EMCD-signal changes with respect to changes of the sign of the q_x-, q_y-components

$$q_x, q'_x \longrightarrow -q_x, -q'_x \;:\; \Im\{S_{\text{dipole}}(\mathbf{q}, \mathbf{q}', E)\} \longrightarrow -\Im\{S_{\text{dipole}}(\mathbf{q}, \mathbf{q}', E)\} \tag{2.34}$$

$$q_y, q'_y \longrightarrow -q_y, -q'_y \;:\; \Im\{S_{\text{dipole}}(\mathbf{q}, \mathbf{q}', E)\} \longrightarrow -\Im\{S_{\text{dipole}}(\mathbf{q}, \mathbf{q}', E)\} \tag{2.35}$$

$$\mathbf{q}, \mathbf{q}' \longrightarrow -\mathbf{q}, -\mathbf{q}' \;:\; \Im\{S_{\text{dipole}}(\mathbf{q}, \mathbf{q}', E)\} \longrightarrow \Im\{S_{\text{dipole}}(\mathbf{q}, \mathbf{q}', E)\}. \tag{2.36}$$

The real part in equation (2.32) does not change sign under these transformations of the q_x-, q_y-components. Under the assumption of a $R(E)$ being diagonal the difference between MDFFs reads in dipole-approximation

$$\begin{aligned} S_{\text{dipole}}(\mathbf{q}_1, \mathbf{q}_1', E) - S_{\text{dipole}}(\mathbf{q}_2, \mathbf{q}_2', E) \\ &= \mathbf{q}_1 R(E) \mathbf{q}_1' + i(\mathbf{q}_1 \times \mathbf{q}_1') \cdot \mathbf{m}(E) \\ &- \mathbf{q}_2 R(E) \mathbf{q}_2' - i(\mathbf{q}_2 \times \mathbf{q}_2') \cdot \mathbf{m}(E) \\ &= 2i(\mathbf{q}_1 \times \mathbf{q}_1') \cdot \mathbf{m}(E), \end{aligned} \tag{2.37}$$

where $\mathbf{q}_1 = (q_x, q_y, q_z)$, $\mathbf{q}_1' = (q_x', q_y, q_z)$, $\mathbf{q}_2 = (-q_x, q_y, q_z)$, and $\mathbf{q}_2' = (-q_x', q_y, q_z)$. Property (2.34) of the MDFF is used in this derivation.

The next question is thus how one can obtain a chiral electron beam, i.e., a beam that allows for the extraction of the imaginary part of the MDFF. According to equation (2.8) any phase shift between the coherent incoming waves, which is not an integer multiple of π, gives rise to a non-vanishing imaginary part. However, the strength of the signal is theoretically maximized if the incoming waves are dephased by $\frac{\pi}{2}$ in the simple case described by equation (2.8). EMCD experiments exploit the beam splitter properties of a crystal in order to obtain a coherent superposition of incoming waves: as described in section 2.1.2 the electron's wave function becomes a superposition of Bloch waves inside the crystal and all partial waves of differing reciprocal lattice vector $\mathbf{g}$ can give rise to a MDFF. In the first EMCD-experiments the two-beam case was used used, in which only the $\mathbf{0}$ and $\mathbf{G}$-components of the Bloch wave are exited. These plane waves have as well a phase shift of close to $\frac{\pi}{2}$ for specimen that are not too thick [2]. The remainder of this section is dedicated to the description of how the Bloch wave formalism enters the calculation of the DDSCS for inelastic electron scattering on a crystal.

So far the discussion of the DDSCS and the MDFF was centered around the inelastic electron scattering on a single atom and thus a generalization to crystals is due: *Kohl and Rose* argue that this generalization is straightforward as the specimen's atoms can be considered as single, independent entities in ELNES since a core-electron is excited to an unoccupied state above the Fermi-level and this process is in good approximation unaffected by the other surrounding atoms [16, p. 206] and the DDSCS becomes an incoherent sum of the DDSCSs $\frac{\partial^2 \sigma_{\tilde{\mathbf{r}}}}{\partial \Omega \partial E}$ of a single atom at position $\tilde{\mathbf{r}}$ according to equation (2.7). Thus

$$\begin{aligned} \frac{\partial^2 \sigma}{\partial \Omega \partial E} &= \sum_{\tilde{\mathbf{r}}} \frac{\partial^2 \sigma_{\tilde{\mathbf{r}}}}{\partial \Omega \partial E} \\ &= \frac{4\gamma^2}{a_0^2} \frac{k_f}{k_i} \sum_{\tilde{\mathbf{r}}} \left[|u|^2 \frac{S_{\tilde{\mathbf{r}}}(\mathbf{q}, \mathbf{q}, E)}{q^4} + |v|^2 \frac{S_{\tilde{\mathbf{r}}}(\mathbf{q}', \mathbf{q}', E)}{q'^4} \right. \\ &\qquad \left. + 2 \frac{\Re\{u v^* S_{\tilde{\mathbf{r}}}(\mathbf{q}, \mathbf{q}', E)\}}{q^2 q'^2} \right]. \end{aligned} \tag{2.38}$$

Furthermore the momentum transfers $\mathbf{q}$ and $\mathbf{q}'$ need to satisfy in an infinite crystal [16]

$$\mathbf{g} = \mathbf{q} - \mathbf{q}' = \mathbf{k}_i - \mathbf{k}_i', \qquad \mathbf{g} = h\mathbf{a}^* + k\mathbf{b}^* + l\mathbf{c}^* \tag{2.39}$$

in addition to the properties of the MDFF already shown in equations (2.10), (2.11), and (2.12). $\mathbf{g}$ is a reciprocal lattice vector and equation 2.39 restricts the incoming wave vectors such that only those pairs of waves contribute to the MDFF in a crystal, whose wave vectors differ by a reciprocal lattice vector $\mathbf{g}$. This strict requirement is partly lifted, however, for finite thickness of the crystal. Due to breaking of infinite translational symmetry in z-direction the reciprocal lattice "smears" out and initial wave vectors satisfying $\mathbf{k}_i - \mathbf{k}_i' = \mathbf{g} + \mathbf{s}$ contribute as well to the DDSCS. $\mathbf{s}$ is non-zero in some vicinity of $\mathbf{g}$ and called *excitation error*.

This incoherent sum can be extended to the case where the incoming and outgoing waves for the inelastic scattering event are Bloch waves. The incoming wave reads then according to equation (2.25)

$$\Psi_{\mathrm{in}}(\mathbf{r}) = \sum_{j\mathbf{g}} C_{\mathbf{0}}^{(j)*} C_{\mathbf{g}}^{(j)} e^{i\gamma^{(j)}(\mathbf{n}\cdot\mathbf{r}-t_0)} e^{i(\chi_{\mathrm{in}}+\mathbf{g})\cdot\mathbf{r}}. \tag{2.40}$$

The inelastic event changes the energy of the electron and one finds

$$\mathbf{q} = \mathbf{k}^{(l)} - \mathbf{k}^{(j)} + \mathbf{h} - \mathbf{g} \tag{2.41}$$

$$\mathbf{q}' = \mathbf{k}^{(l')} - \mathbf{k}^{(j')} + \mathbf{h}' - \mathbf{g}', \tag{2.42}$$

where $\mathbf{k}^{(l)}$, $\mathbf{k}^{(l')}$ are the wave vectors of the outgoing wave. The principle of reciprocity is invoked for the outgoing wave: different beams in the DP can be viewed as the plane wave components of the beam electron's wave function after exiting the sample. Time reversal and the exchange of the source and detector allow then to solve the SEQ in the crystal for the outgoing wave in a similar way as one obtained the incoming wave [10]. One effectively propagates a plane wave back into a Bloch wave which is propagated backwards through the specimen to the site of the inelastic event. The outgoing wave reads then

$$\Psi_{\mathrm{out}}(\mathbf{r}) = \sum_{l\mathbf{h}} D_{\mathbf{0}}^{(l)} D_{\mathbf{h}}^{(l)*} e^{i\gamma^{(l)}(\mathbf{n}\cdot\mathbf{r}-t)} e^{i(\chi_{\mathrm{out}}+\mathbf{h})\cdot\mathbf{r}}. \tag{2.43}$$

$D_{\mathbf{h}}^{(l)}$ are the Bloch coefficients of the outgoing wave. The thickness of the crystalline specimen is taken to be t and the exit surface of the crystal is taken to be parallel to the entrance surface. In this geometry the DDSCS becomes [10]

$$\frac{\partial^2\sigma}{\partial\Omega\partial E} = \sum_{\mathbf{ghg'h'}} \frac{1}{N_{\mathbf{u}}} \sum_{\mathbf{u}} \frac{S_{\mathbf{u}}(\mathbf{q},\mathbf{q}',E)}{q^2 q'^2} e^{-i(\mathbf{q}-\mathbf{q}')\cdot\mathbf{u}} \sum_{jlj'l'} Y_{\mathbf{ghg'h'}}^{jlj'l'} T_{jlj'l'}(t), \tag{2.44}$$

where

$$Y_{\mathbf{ghg'h'}}^{jlj'l'} = C_{\mathbf{0}}^{(j)*} C_{\mathbf{g}}^{(j)} D_{\mathbf{0}}^{(l)} D_{\mathbf{h}}^{(l)*} C_{\mathbf{0}}^{(j')} C_{\mathbf{g}}^{(j')*} D_{\mathbf{0}}^{(l')} D_{\mathbf{h}}^{(l')*}, \tag{2.45}$$

$$T_{jlj'l'}(t) = e^{i[(\gamma^{(j)}-\gamma^{(j')})+(\gamma^{(l)}-\gamma^{(l')})]\cdot\frac{t}{2}} \frac{\sin\Delta(t/2)}{\Delta(t/2)} \tag{2.46}$$

Table 2.1: Comparison of the relativistic quantum numbers of the initial states of the L_2 and L_3-edge of the bcc-Fe.

edge	initial state	n	l	j	j_z	κ
L_2	$2p_{1/2}$	2	1	1/2	-1/2, 1/2	1
L_3	$2p_{3/2}$	2	1	1/2	-3/2, -1/2, 1/2, 3/2	-2

and

$$\Delta = (\gamma^{(j)} - \gamma^{(j')}) - (\gamma^{(l)} - \gamma^{(l')}). \tag{2.47}$$

The sum over $\mathbf{u}$ in equation (2.44) is effectively a sum over the basis of the lattice, i.e., all the atoms in the primitive cell of the crystal structure. The next section deals with a description of how the MDFF is evaluated in practice.

2.1.4 *Evaluation of mixed dynamic form factor*

This section is dedicated to a description of the evaluation process of the mixed dynamic form factor (MDFF). In order to simulate ELNES-spectra and EMCD equation (2.44) needs to be evaluated. In order to do so the MDFF must be rewritten into a tractable from.

First a suitable form of the initial and final state needs to be found. The initial state $|i\rangle$ in ELNES is a deep-lying atomic core state, that does not participate in the bonding. The crystal potential for these states is to good approximation spherically symmetric. For precise ELNES calculations of the spin-orbit split L_2 and L_3-edge of bcc-iron relativistic effects giving rise to the fine structure of atomic orbitals need to be taken into account. The initial state is thus taken to be a solution of the Dirac equation and is as such similar to an orbital of the free relativistic hydrogen atom, adapted to the larger nuclear charge of iron $Z = 26$. The quantum numbers of the initial states are the main quantum number n, the total angular momentum quantum number j, the magnetic quantum number j_z and the relativistic quantum number κ. $E_{nl\kappa}$ is furthermore its relativistic energy. The values of these quantum numbers are tabulated for the initial states of the bcc-Fe L_2 and L_3-edge in table 2.1. Considering each edge on its own the sum over the final state is replaced by the sum over j_z, i.e.,

$$\sum_i (\dots) \longrightarrow \sum_{j_z} (\dots) \tag{2.48}$$

The final state $|f\rangle$ in ELNES is an itinerant Bloch-state, i.e. an unoccupied continuum state $|\nu\mathbf{k}\rangle$ in the band structure of the investigated material: in the energy-loss window covered by ELNES the energy transfer from the beam electron to the core-electron in initial state $|i\rangle$ is just large enough to promote it into an unoccupied band state close to the Fermi level. The quantum numbers of the Bloch-state $\mathbf{k}$ and ν correspond to the band index ν and the Bloch wave vector **k**. The sum over the final state is thus replaced by the sum over bands and **k**

$$\sum_{f}(\dots) \longrightarrow \sum_{\nu\mathbf{k}}(\dots). \tag{2.49}$$

A complete derivation of the MDFF is included in the supplementary information to the paper by *Schattschneider et al.* [2]. The result of this derivation reads

$$\begin{aligned} S(\mathbf{q},\mathbf{q}',E) = &\sum_{mm'}\sum_{LMS}\sum_{L'M'S'}\sum_{\lambda\mu}\sum_{\lambda'\mu'} 4\pi i^{\lambda-\lambda'}(2l+1)\sqrt{[\lambda,\lambda',L,L']} \\ &\cdot Y_{\lambda}^{\mu}(\mathbf{q}/q)^{*}\, Y_{\lambda'}^{\mu'}(\mathbf{q}'/q')\left\langle j_{\lambda}(q)\right\rangle_{ELSj}\left\langle j_{\lambda'}(q')\right\rangle_{EL'S'j} \\ &\cdot \begin{pmatrix} l & \lambda & L \\ 0 & 0 & 0 \end{pmatrix}\begin{pmatrix} l & \lambda' & L' \\ 0 & 0 & 0 \end{pmatrix}\begin{pmatrix} l & \lambda & L \\ -m & \mu & M \end{pmatrix}\begin{pmatrix} l & \lambda' & L' \\ -m' & \mu' & M' \end{pmatrix} \\ &\cdot \sum_{j_z}(-1)^{m+m'}(2j+1)\begin{pmatrix} l & \frac{1}{2} & j \\ m & S & -j_z \end{pmatrix}\begin{pmatrix} l & \frac{1}{2} & j \\ m' & S' & -j_z \end{pmatrix} \\ &\cdot \sum_{\nu\mathbf{k}} D_{LMS}^{\nu\mathbf{k}} D_{L'M'S'}^{\nu\mathbf{k}*}\,\delta\left(E+E_{nl\kappa}-E_{\nu\mathbf{k}}\right), \end{aligned} \tag{2.50}$$

where $[\lambda,\lambda',L,L'] = (2\lambda+1)(2\lambda'+1)(2L+1)(2L'+1)$.

In the derivation of equation 2.50 exponential $e^{i\mathbf{q}\cdot\hat{\mathbf{R}}}$ was expanded according to the Rayleigh expansion given in equation (1.2) and Y_{λ}^{μ} are the spherical harmonics that stem from this expansion. All radial integrals are grouped together in equation 2.50 and read

$$\left\langle j_{\lambda}(q)\right\rangle_{ELSj} = \int_{0}^{R_{\mathrm{MT}}} \mathrm{d}r\, r^{2} u_{LS}^{E}(r) R_{jS}(r) j_{\lambda}(qr), \tag{2.51}$$

where $u_{LS}^{E}(r)$ is the radial wave function of the final state projected onto the LMS subspace within the muffin tin radius R_{MT} (c.f. chapter 3 for a definition of R_{MT}). $R_{js}(r)$ is the radial wave function of the initial state projected onto the position-spin basis $|r,s\rangle$ and j_{λ} are spherical Bessel functions. Wigner 3-j symbols,

$$\begin{pmatrix} j_1 & j_2 & j_3 \\ m_1 & m_2 & m_3 \end{pmatrix} = \frac{(-1)^{j_1-j_2-m_3}}{\sqrt{2j_3+1}}\left\langle j_1 m_1 j_2 m_2 | \, j_3(-m_3)\right\rangle, \tag{2.52}$$

and Wigner 3-jm symbols

$$\sqrt{\frac{(2l_1+1)(2l_2+1)(2l_3+1)}{4\pi}}\begin{pmatrix} l_1 & l_2 & l_3 \\ 0 & 0 & 0 \end{pmatrix}\begin{pmatrix} l_1 & l_2 & l_3 \\ m_1 & m_2 & m_3 \end{pmatrix} \tag{2.53}$$

$$= \int Y_{l_1 m_1}(\theta,\varphi) Y_{l_2 m_2}(\theta,\varphi) Y_{l_3 m_3}(\theta,\varphi)\, \sin\theta\, \mathrm{d}\theta\, \mathrm{d}\varphi \tag{2.54}$$

are used in equation (2.50) to express the summation of involved angular momenta. The last sum in equation (2.50) is the so-called cross-DOS

$$\sum_{\nu\mathbf{k}} D_{LMS}^{\nu\mathbf{k}} D_{L'M'S'}^{\nu\mathbf{k}*}\,\delta\left(E-E_{\nu\mathbf{k}}\right) \tag{2.55}$$

shifted by an energy $E_{nl\kappa}$. This quantity can be evaluated in from electronic structure calculations. In the present work the `WINE2k` density functional theory (DFT)-code is used as described in chapter 3.

It is evident that equation (2.50) cannot be calculated to all orders in λ, λ' and the expansion needs to be cut off: the terms

$$\begin{aligned}\text{lamb1}: &\quad 0 \leq \lambda, \lambda' \leq 1\\ \text{lamb2}: &\quad 0 \leq \lambda, \lambda' \leq 2\\ \text{lamb3}: &\quad 0 \leq \lambda, \lambda' \leq 3,\end{aligned}$$

will be used in the following to describe an approximation to the MDFF, which is computed for multipole terms up to a certain order. The lamb3-approximation is most accurate approximation level included in this work.

Sorting the components of the lamb3-MDFF according to λ, λ' and representing it in matrix-form, one gets

$$\begin{pmatrix} 00 & 01 & 02 & 03\\ 10 & 11 & 12 & 13\\ 20 & 21 & 22 & 23\\ 30 & 31 & 32 & 33 \end{pmatrix}, \tag{2.56}$$

which visualizes nicely what is meant by the term *cross term*: the *cross terms* (off-diagonal elements) of this matrix correspond to terms that mix different multipole terms. The matrix in equation (2.56) is hermitian and the contributions of cross terms are thus summed according to

$$\begin{aligned}\widetilde{01} &= 01 + 10\\ \widetilde{02} &= 02 + 20\\ &\vdots\\ \widetilde{33} &= 23 + 32.\end{aligned}$$

Equation (2.56) becomes then

$$\begin{pmatrix} 00 & \widetilde{01} & \widetilde{02} & \widetilde{03}\\ - & 11 & \widetilde{12} & \widetilde{13}\\ - & - & 22 & \widetilde{23}\\ - & - & - & 33 \end{pmatrix}.$$

For the remainder of this work the following notation is adopted for the cross terms:

$$\begin{aligned}01 &\equiv \widetilde{01}\\ 02 &\equiv \widetilde{02}\\ &\vdots\\ 23 &\equiv \widetilde{23}\end{aligned}$$

3

ELECTRONIC STRUCTURE CALCULATION OF BCC-IRON

This chapter is dedicated to the brief presentation of the results of a DFT-simulation of bcc-iron using the `WIEN2K` software package [21]. Section 3.1 deals with a brief description of the performed DFT-calculation and the obtained DOS is presented and checked for convergence in section 3.2.

3.1 METHOD OF WIEN2K

The `WIEN2k` software package [21–23] is used to compute the electronic structure of bcc-iron in the framework of scalar-relativistic DFT. DFT is based on the Hohenberg-Kohn theorems, which state the existence of a unique correspondence between the external potential in the many-body SEQ and the *ground state* electron density [24]. Therefore the density gives access to all properties of a material and it is the only quantity one needs to know. The Hohenberg-Kohn theorems do, however, not provide a way of obtaining the density. The second fundamental ingredient to DFT are thus the self-consistent Kohn-Sham equations, which provide an algorithm for calculating the density in a single electron mean-field picture [25].

`WIEN2k` employs by default the full-potential APW+lo+LO- and linearized augmented plane wave (LAPW)+LO-methods to solve the Kohn-Sham equations for all electrons in the studied system. A very good introductory text about these methods by *S. Cottenier* is freely available [26]. The interested reader is referred to this text for mathematical details and further references as these are omitted here for the sake of brevity.

The crystal is divided into two separate spatial regions in the spirit of the *muffin tin* approximation within the linearized augmented plane wave (LAPW)- and augmented plane wave (APW)(+lo)-method: spheres of a so-called *muffin tin radius* R_{MT} are centered around each atomic site of the crystal and the region in between the atomic spheres is called the *interstitial region*. Inside the atomic spheres the potential varies rapidly but it is in good approximation spherically symmetric. Thus the Kohn-Sham equations can be efficiently solved in a basis of spherical harmonics and spherical Bessel functions. The potential is on the other hand relatively flat in the interstitial region and obeys the crystal symmetry, which allows to efficiently use a plane wave basis. The boundary condition is that the wave functions inside the atomic region and inside the interstitial region need to match on the boundary of both regions.

The APW- and linearized augmented plane wave (LAPW)-basis use the same plane wave expansion in the interstitial region but differ in the basis set used in the atomic region and in the matching conditions at the boundary between the atomic and the interstitial region: The APWs have an energy-dependent radial part part in the atomic region. This makes the APW-basis inherently inefficient since the radial part needs to be computed again and again for every Kohn-Sham eigenvalue (KSE) even though the basis set required for a certain accuracy is smaller than for a plane wave basis [26]. The LAPWs-method remedies this energy-dependence by linearizing the radial part around the center energy of the respective band. The linearization error increases thereby with the square of the difference between the KSE and the band center energy. Doing so increases the basis set compared to the APW-basis but the overall computational costs are lowered. The APW+lo method on the other hand adds local orbitals (therefore "+lo") to the basis set in the atomic region, which are required to have zero value at the boundary between the atomic and interstitial region. It thereby achieves to have an energy-independent basis set of similar size as the APW-basis for a certain accuracy and is thus inherently faster than a calculation using the LAPW-basis.

In all the named methods the quality and thus size of the basis set is commonly chosen to be determined by the product

$$R_{\mathrm{MT}}^{\mathrm{min}} K_{\mathrm{max}}$$

of the minimal muffin tin radius $R_{\mathrm{MT}}^{\mathrm{min}}$ of all atoms in the system and the maximum magnitude of the wave vector considered in the plane wave basis K_{max}. This makes intuitively sense since the potential in the interstitial region is more flat the larger one chooses $R_{\mathrm{MT}}^{\mathrm{min}}$ and the plane wave basis requires less plane waves to sufficiently describe the wave function. Conversely shrinking $R_{\mathrm{MT}}^{\mathrm{min}}$ means that K_{max} needs to increase in order to produce results of comparable quality, i.e., constant $R_{\mathrm{MT}}^{\mathrm{min}} K_{\mathrm{max}}$.

Furthermore local orbitals (LOs) can be added to the LAPW- and APW+lo-basis in order to improve the description of so-called *semi-core states*, i.e., states whose wave function is mainly contained in the muffin tin sphere but has a non-negligible value outside the muffin tin radius. These states can therefore not be considered pure core states. The LOs are added to the basis in the atomic region and are required to have zero value at the boundary between the interstitial and atomic regions. Lastly the LOs are not to be confused with the local orbitals of the APW+lo-basis.

As mentioned before `WIEN2k` uses by default fully relativistic solutions to the Dirac equation for core states and a mix of the APW+lo+LO- and linearized augmented plane wave (LAPW)+LO-basis. Using the same $R_{\mathrm{MT}}^{\mathrm{min}} K_{\mathrm{max}}$ the APW+lo-basis is considerably larger than the LAPW-basis. One can thus treat states that require a larger basis, such as d and f states, in the APW+lo-basis and keep using LAPW for the other states. This procedure allows to reduce $R_{\mathrm{MT}}^{\mathrm{min}} K_{\mathrm{max}}$ in comparison with a pure LAPW-calculation and reduces thus the computational costs while maintaining the accuracy.

Since the initial states of the L_2 and L_3-edge of bcc-iron are the spin-orbit split states $2p_{1/2}$ and $2p_{3/2}$, respectively, on needs to include the effects of spin-orbit coupling into the electronic structure calculation. `WIEN2k` allows to treat relativistic effects such as spin-orbit fully relativistically for core states and in a scalar relativistic approximation for valence states and local orbitals [27]. The procedure for obtaining a self-consistent relativistic calculation in `WIEN2k` is to first obtain a non-relativistic self-consistent density and to use this density as an input to the relativistic calculation. The relativistic calculation needs another initialization since the number of symmetry operations is often reduced in the relativistic calculation in comparison with the non-relativistic case.

3.2 COMPUTATIONAL DETAILS OF THE DFT SIMULATION

The first part of this section is focused on the description of the simulation parameters used to obtain a converged `WIEN2k`-simulation of bcc-iron: a bcc-lattice parameter of 2.8665 Å is used [28] and the muffin tin radius is set to $R_{\mathrm{MT}} = 2.3\,a_0$. In the initialization of the non-relativistic calculation the `PBE-GGA` exchange correlation potential of *Perdew, Burke and Ernzerhof* [29] is used and the energy-cutoff separating core and band states is set to -6.0 Ry. LOs are added for $3p$ semi-core states and the APWs+lo-basis is used for the $3p$-, $3d$-, and $4s$-states. A charge convergence criterion of 0.000 001 is used throughout all self-consistent calculations. The `GMAX` parameter is set to $15.0\,\mathrm{a_0}^{-1}$ and during the initialization of the relativistic calculation the magnetic moment is chosen to be aligned to the z-axis. The number of k-points N_k in the Brillouin zone (BZ) and the parameter $R_{\mathrm{MT}}K_{\mathrm{max}}$ are the main parameters governing the quality of the `WIEN2k`-simulation.

The second part of this section deals with the convergence test of the `WIEN2k`-simulation: the projected DOS is one of the main quantities influencing the overall quality of the calculation of the MDFF. Therefore the convergence of the DOS with respect to the number of k-points N_k in the BZ and the basis size given by the parameter $R_{\mathrm{MT}}K_{\mathrm{max}}$ is examined by comparing the resulting total DOS. The results of this convergence test are depicted in the subfigures of figure 3.1. All figures show a typical DOS of bcc-iron with the so-called *pseudo-gap* in the minority-spin channel (here spin-down with respect to the z-axis) and a magnetic moment arising from the asymmetry of the DOS with respect to the spin-direction. The convergence tests show that the DOS is well converged for $N_k \geq 10\,000$ and $R_{\mathrm{MT}}K_{\mathrm{max}} \geq 7.0$. The calculation using $N_k \geq 15\,000$ and $R_{\mathrm{MT}}K_{\mathrm{max}} = 8.5$ is chosen for subsequent calculations of the MDFF. The value of the total spin-magnetic moment per atom is in this calculation $m_S = 2.22\,\mu_{\mathrm{B}}$.

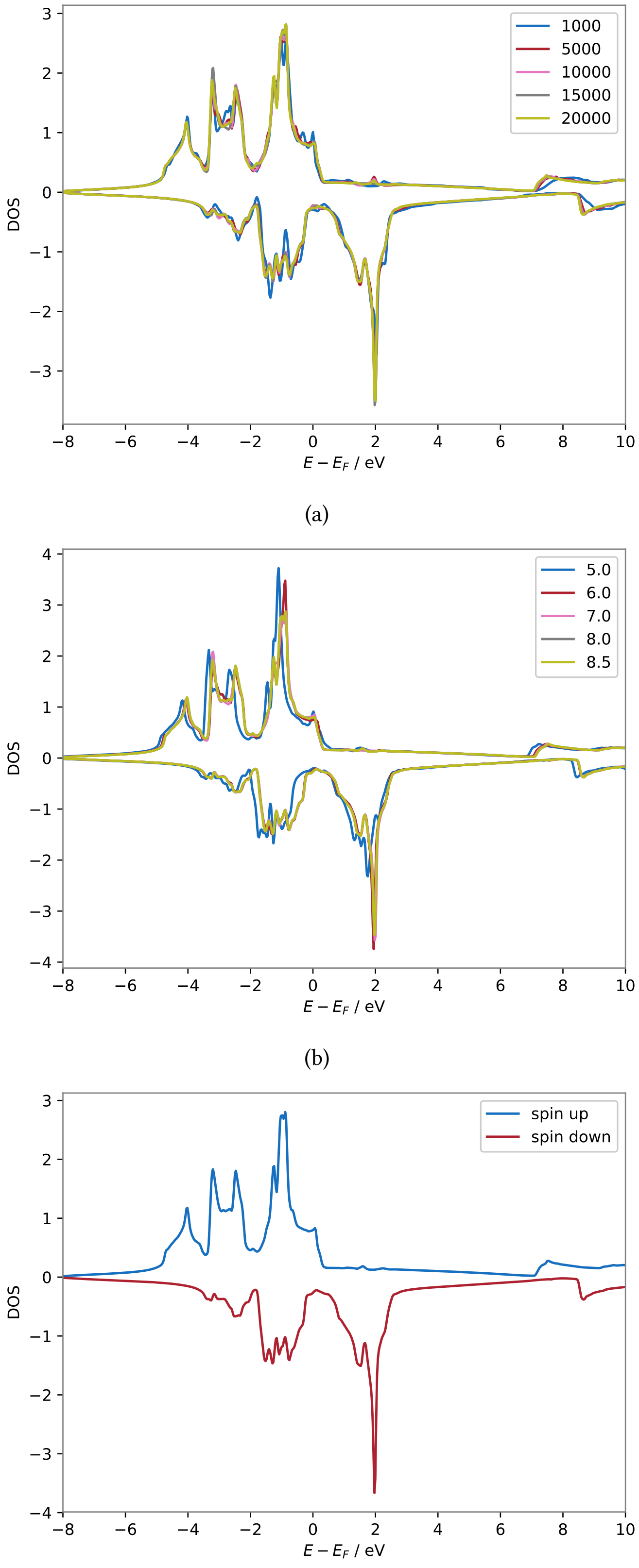

(a)

(b)

(c)

Figure 3.1: Visualization of the convergence behavior of the DOS of bcc-Fe with respect to the number of k-points in the BZ N_k (a) and the LAPW/APW-convergence parameter $R_{\mathrm{MT}}K_{\mathrm{max}}$ (b). (c) shows the DOS for $N_k = 15\,000$ and $R_{\mathrm{MT}}K_{\mathrm{max}} = 8.5\ \mathrm{a_0}^{-1}$ of the calculation used for the simulation of ELNES and EMCD. All calculations include spin-orbit coupling on the DOS is plotted around the Fermi energy E_F. Refer to the text of section 3.2 for further details on the other used parameters.

4

SIMULATION METHOD

This chapter deals with a description of the performed simulations. The general aim of the DDSCS-calculation and the subsequent postprocessing is to produce ELNES-spectra that reflect the state of the current theoretical understanding of the contributing processes. The extraction procedure of the EMCD-signal closely resembles the procedure performed on experimental spectra in order to observe its influence on the obtained EMCD-signal. Special emphasis is put on the analysis and discussion of non-dipole contributions to the measured signal.

This section is divided into three subsections: in subsection 4.1 the method of calculating the DDSCS is described and all simulation parameters are described. Thereafter the extraction procedure for the EMCD-signal is described in subsection 4.2. Subsection 4.3 deals with a description of how the ratio of orbital to spin-magnetic moment is extracted from the EMCD-signal.

4.1 COMPUTATIONAL PROCEDURE FOR CALCULATION OF THE DDSCS

Equations (2.44) and (2.50) are solved using an algorithm developed by *Rusz et al.* [30]. In a first step the cross-DOS is calculated for an energy range of 0 eV to 30 eV above the Fermi level using the parameters described and converged in section 3.2. This is a rather large energy range and the cross-DOS will suffer from linearization errors in the `WIEN2k`-basis for states far from the Fermi level (c.f. chapter 3).

The unoccupied part of the electronic structure of bcc-iron is thereby approximated by the unoccupied DFT-states. It should be noted at this point that this is an approximation since the Hohenberg-Kohn theorems hold only for the *ground state* electron density [24] and DFT is fundamentally a theory for the electronic ground state. However, the use of DFT states has a long tradition and many spectral features are well reproduced [31, 32]. Apart from the cross-DOS the radial wave functions of the core states are also taken from the converged `WIEN2k`-simulation.

In a next step the Bloch wave expansion according to equations (2.44)-(2.47) is calculated for thicknesses 1 nm to 50 nm. The EMCD-signal has been found to be strongest between 10 nm to 20 nm [10], which is as well chosen to be the range of thicknesses that the present work focuses on.

Furthermore the calculation makes another simplifying assumption for the momentum transfer vector $\mathbf{q}$ (and similarly $\mathbf{q}'$)

$$\mathbf{q} = \mathbf{k}^{(l)} - \mathbf{k}^{(j)} + \mathbf{h} - \mathbf{g} \approx \chi_{\text{out}} - \chi_{\text{in}} + \mathbf{h} - \mathbf{g}, \tag{4.1}$$

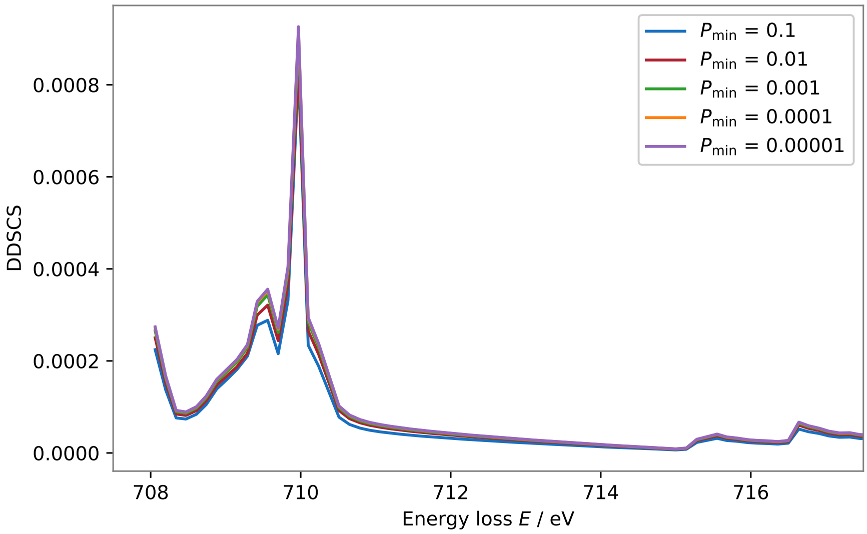

(a) L_3-edge

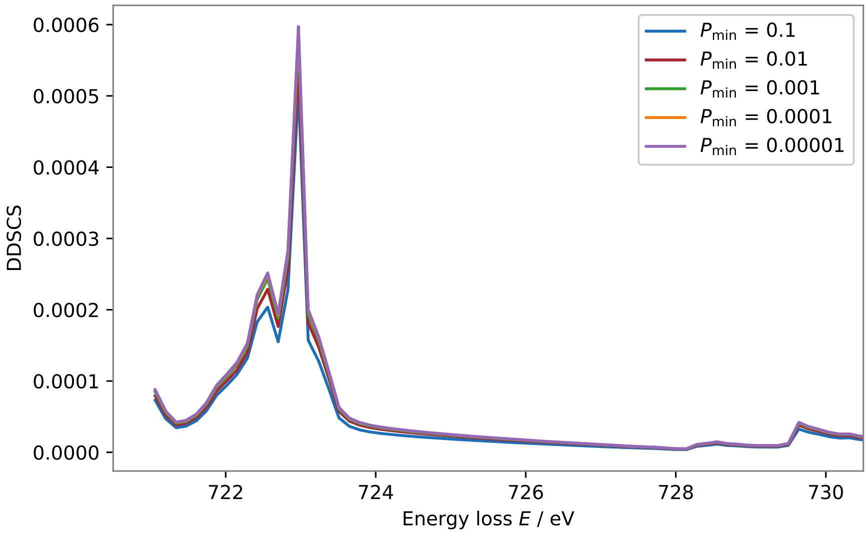

(b) L_2-edge

Figure 4.1: Convergence of the unbroadened DDSCS with respect to the Bloch wave cutoff P_{min} at the L_3-edge (subfigure (a)) and at the L_2-edge (subfigure (b)). These spectra are computed for a scattering angle of $(\theta_x, \theta_y) = (9.0, 9.0)$ and thickness 15 nm.

i.e., the change of the electron's wave vector in z-direction is neglected ($\gamma^{(j)} = 0$ in equation (2.23)).

The cut-off criterion for the Bloch wave expansion is given by the requirement that those Bloch waves are neglected for which the Bloch coefficients in equation (2.45) satisfy [30]

$$\left|Y^{jlj'l'}_{\mathbf{ghg'h'}}\right| < P_{\mathrm{min}}. \tag{4.2}$$

Rusz et al. found further that DPs are well converged for a choice of $P_{\mathrm{min}} = 0.0001$ [30] and this value is chosen for this work too. A convergence check of the entire diffraction pattern is not feasible due to limited computational resources. A convergence check of the DDSCS with respect to P_{min} is displayed in figure 4.1, which shows that the chosen value $P_{\mathrm{min}} = 0.0001$ delivers well converged spectra.

The incident beam is a single plane wave of energy $E_{\mathrm{kin}} = 200\,\mathrm{keV}$ beam, which corresponds to parallel illumination of the specimen. The bcc-iron crystal is tilted to an exact three beam case by an angle $\alpha \approx 10^\circ$ in the y-z-plane. The crystallographic [016]-direction is then parallel to the z-axis. For a bcc-structure reflections $\mathbf{g}_{hkl}$ satisfying $h + k + l =$ odd are forbidden and in the exact three beam case the Bragg spots

$$\begin{aligned} \mathbf{G} &\equiv \mathbf{g}_{200}, \\ \mathbf{0} &\equiv \mathbf{g}_{000}, \\ \text{and} \quad -\mathbf{G} &\equiv \mathbf{g}_{\bar{2}00} \end{aligned}$$

are excited. As in mentioned in section 3.2 the lattice constant of bcc-iron is $a = 2.8665\,\text{Å}$ and the length of $|\mathbf{G}|$ is thus

$$|\mathbf{G}| = 2 \cdot \frac{2\pi}{a} = 4.383\,\text{Å}^{-1}. \tag{4.3}$$

The corresponding scattering angle is

$$\theta_{\mathrm{G}} = 2\theta_{\mathrm{B}} \approx \frac{2\lambda}{2d} = \frac{2\lambda}{a} \approx 17.51\,\mathrm{mrad}, \tag{4.4}$$

θ_{B} is the Bragg angle and $d = \frac{a}{2} = \frac{2\pi}{|\mathbf{G}|}$ the spacing of lattice planes, which correspond to the $\mathbf{G}$-reflection. λ is the relativistic *de-Broglie* wave length of the electron, i.e,

$$\lambda = \frac{h}{p} = \frac{h}{m_e v}\sqrt{1 - \frac{v^2}{c_0^2}} = \frac{h}{m_e c_0}\left[\sqrt{\frac{(R + E_{\mathrm{kin}})^2}{R^2} - 1}\right]^{-1} \approx 2.51\,\mathrm{pm}, \tag{4.5}$$

where $v = c_0\sqrt{1 - \frac{R^2}{(R+E_{\mathrm{kin}})^2}}$ is the relativistic velocity of the beam electron and $R = m_e c_0^2$ its energy in the rest-frame.

For a given pixel and given set of energy losses, i.e., a final wave vector $\boldsymbol{\chi}_{\mathrm{out}}$, the convergence criterion in equation 4.2 limits the number of excited Bloch waves to a finite set. Thus only a finite set of vectors $\mathbf{g}, \mathbf{g}', \mathbf{h}, \mathbf{h}'$ enter equation 4.1 resulting in a finite set of momentum transfers $\mathbf{q}, \mathbf{q}'$. The MDFF is then evaluated for this finite set of momentum transfers using the electronic structure information from `WIEN2k` according to equation (2.50). In a last step the calculated MDFF and Bloch coefficients are used to compute the DDSCS according to equation 2.44.

The calculation of the Bloch coefficients, the MDFF and the final summation are performed by executing the programs `DYNDIF`, `MDFF` and `DYNDIF` in that order. The programs are developed by Dr. Ján Rusz at the Department of Physics and Astronomy at Uppsala University. The `MDFF`-code is modified for the present work to allow the output of all cross-terms for pairs of momentum transfers $\mathbf{q}, \mathbf{q}'$ as well as the imaginary part of the total MDFF and the 11 term. Similarly the `DYNDIF`-code is modified to be able to sum these cross terms to DDSCSs, which stem solely from the different diagonal and cross-terms as well as approximation levels described in section 2.1.4. Furthermore a collection of analysis tools is developed for the subsequent post-processing and analysis steps required for this work [33].

The result of these simulations is a data cuboid of edge-, energy- and thickness resolved diffraction patterns: the DDSCS is computed for a range of scattering angles θ_x, θ_y, energy losses E_j, $j \in \{L_2, L_3\}$ and thicknesses t:

$$\begin{aligned}
\theta_x, \theta_y &\in [-25\,\text{mrad}, 25\,\text{mrad}],\ \ 51 \times 51\text{–grid} \\
E_{L_3} &\in [708\,\text{eV}, 738\,\text{eV}],\ \ \text{step size } 0.13\,\text{eV} \\
E_{L_3} &\in [721\,\text{eV}, 751\,\text{eV}],\ \ \text{step size } 0.13\,\text{eV} \\
t &\in [1\,\text{nm}, 50\,\text{nm}],\ \ \text{step size } 0.5\,\text{nm}.
\end{aligned}$$

An edge-resolved DP is thus effectively formed at every value of E_j and t.

4.2 EXTRACTION OF THE EMCD-SIGNAL

Experimentally the EMCD-signal is commonly extracted by means of so-called *difference methods*. As their name suggests these methods yield the EMCD-signal as a difference between spectra captured at special detector positions in the DP. These detector positions are closely connected to the geometrical considerations for the diffraction pattern presented in section 2.1.3. At every detector position the detector covers a certain area of the diffraction pattern, whose size is determined by the collection angle of the detector, in order to obtain a sufficiently high count rate and the captured ELNES-spectrum stems thus from a range of scattering angles. The power-law background due to plural plasmon scattering is commonly removed from the measured spectra by fitting the pre-edge region (c.f. figure 2.1) to a function of the form of equation (2.1). Before extracting the EMCD-signal a so-called *post-edge normalization* is applied to the spectra processed in this way in order to account for differences in the count rate at the different detector positions. Lastly the difference of the post-edge normalized spectra is taken according to one of the difference methods and thus the EMCD-signal is obtained.

There are two principal approaches to the extraction of the EMCD-signal from a theoretical point of view: one can either use the real and imaginary part, or only the imaginary part of the MDFF to compute the DDSCS and thus the DP. The first extraction variant resembles more closely the experimental reality and will be called extracted EMCD (eEMCD) in the following. The second variant corresponds to the direct extraction of the "pure" magnetic signal since the imaginary part of the MDFF is in dipole approximation solely due to the presence of magnetic moments as described in section 2.1.1 and 2.1.3. The EMCD-signal obtained in this way will be termed pure EMCD (pEMCD) in the following. It should be noted here that the pEMCD represents an ideal case in which one has a complete cancellation of the real parts of the MDFF by means of the chosen difference method which is most certainly not fully attainable in an experiment. From a theoretical point of view it is however to be expected that eEMCD and pEMCD yield very similar results. It should be noted here that the terms eEMCD and pEMCD are not used in the literature and serve the sole purpose of a convenient terminology in this work.

eEMCD and pEMCD do not differ in anything other than the way the raw DDSCS is computed and the subsequent post processing steps are similar in both cases: In order to account for core-level broadening the raw DDSCS is convoluted with a Loentzian profile as detailed in section 4.2.1 below. The theoretical ELNES-spectrum at a certain thickness and detector position is obtained by summing the broadened spectra over the pixels covered by the detector. After post-edge normalization the spectra obtained in this way should closely resemble experimental ELNES-spectra after background removal and post edge normalization if all the processes contributing to the spectrum are addressed properly in the theory. The EMCD-signal is extracted from such spectra via a difference method as in the case of experimental spectra. The EMCD-signal obtained in this way should in theory be very close to experimentally obtained signals and allows for the investigation of the effects, which the post-edge normalization and difference method have on the theoretically expected EMCD-signal.

The following section deals with a brief description of the broadening of the raw DDSCS computed by the procedure detailed in section 4.1. Thereafter section 4.2.2 contains procedural details about the post-edge normalization and section 4.2.3 describes the three difference methods for the extraction of EMCD.

4.2.1 *Spectral broadening*

ELNES-spectra exhibit three distinct types of broadening: core-hole or core-level broadening, broadening of the excited state, and instrumental broadening [34]. The first two types are broadenings of electron energy levels due

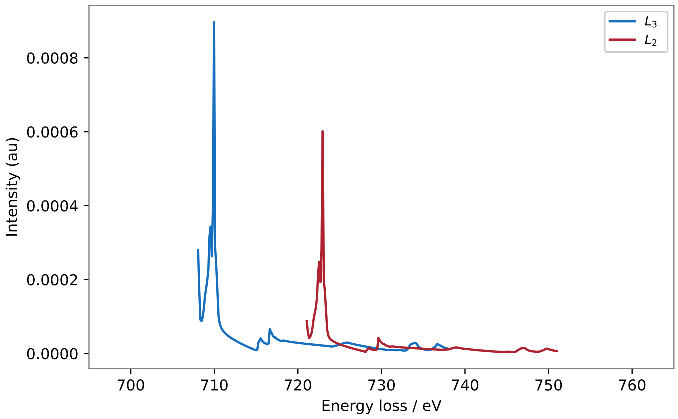

(a)

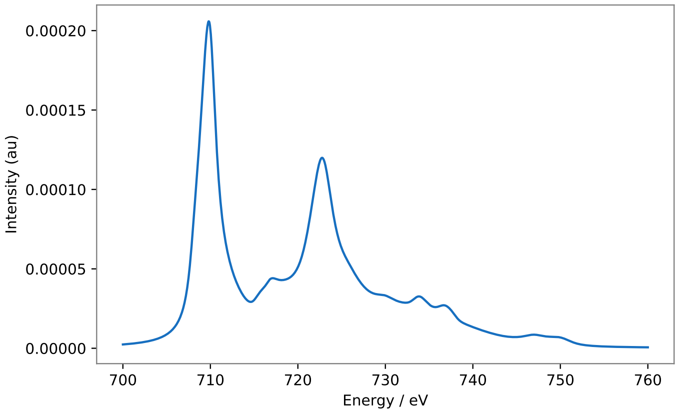

(b)

Figure 4.2: Visualization of the effect of spectral broadening on the calculated DDSCS: subfigure (a) displays the raw DDSCS at thickness 15 nm and scattering angle (9.0 mrad, 9.0 mrad). In subfigure (b) the broadened DDSCS is depicted. Refer to the main text of section 4.2.1 for details on the broadening.

to their finite-lifetime, which is usually taken into account by a convolution of the calculated raw DDSCS with a Lorentzian profile of the form

$$L(x; x_0, \gamma) = \frac{1}{\pi\gamma}\left[\frac{\gamma^2}{(x - x_0)^2 + \gamma^2}\right], \tag{4.6}$$

where γ specifies the half width at half maximum (HWHM) and x_0 is the position of the central maximum.

The broadening parameter for the excited state broadening, however, is energy dependent and different models exist on how to take it into account. A simple model increases the broadening parameter linearly with the electron energy loss [34]. Instrumental broadening on the other hand is caused by the finite energy spread of the electron beam in the TEM and can be modeled by a convolution of the spectrum with a Gaussian function [34]. In this work only core-level broadening with parameters $\gamma_2 = 1.2\,\text{eV}$ and $\gamma_3 = 0.7\,\text{eV}$ for L_2 and L_3 edge, respectively, is taken into account in order to keep the broadening model simple and free from experimental peculiarities. It should be noted that the chosen values for the broadening parameter have been recommended to Dr. Ján Rusz by Prof. Dr. Peter Oppeneer in private communication for the calculation of x-ray absorption near-edge structures (XANES)-spectra: they are larger than for pure core-level broadening but take to some degree other effects into account such as final state broadening. Given their independence on energy it is to be expected that the broadening of the ELNES-spectra is underestimated for large energies.

4.2.2 *Post-edge normalization*

Experimentally one needs a way to reduce the effect of differences in the count rate between different detector positions due to slight misorientations of the specimen and other effects. In order to achieve this result experimentalists resort to the procedure of post-edge normalization in which the energy loss integral over the mostly featureless post-edge region $[E_-, E_+]$ of an ELNES-spectrum is normalized to unity, i.e.

$$\frac{\partial\tilde{\sigma}}{\partial E} = \frac{\frac{\partial\sigma}{\partial E}}{\int_{E_-}^{E_+} \frac{\partial\sigma}{\partial E}\,\mathrm{d}E}, \tag{4.7}$$

where $\frac{\partial\tilde{\sigma}}{\partial E}$ is the post-edge normalized ELNES-spectrum. The definition of the *post-edge region* $[E_-, E_+]$ is to some extent arbitrary and often E_- is taken to be the beginning of the more or less constant part of the post-edge spectrum and E_+ the end of the measured energy loss window. The interested reader is referred to section 5.1 for an example of an experimental spectrum.

From a theoretical point of view the procedure of post-edge normalization implicitly assumes that the EMCD-signal is somewhat confined to a small region below the L_3 and L_2-edge and that the spectral intensity of the post-edge region is of a similar origin and shape in all four quadrants of the diffraction pattern. Any incomplete cancellation of the real part of the MDFF or contributions of non-dipole cross-terms can thus influence the eEMCD-signal.

Judging from figure 4.2 three choices for the post-edge normalization range are identified:

$$[730.0\,\mathrm{eV}, 740.0\,\mathrm{eV}] \tag{4.8}$$

$$[730.0\,\mathrm{eV}, 750.0\,\mathrm{eV}] \tag{4.9}$$

$$[740.0\,\mathrm{eV}, 750.0\,\mathrm{eV}]. \tag{4.10}$$

Both edges are almost entirely calculated for the first choice and it is thus the most justified choice. The second range has the advantage of covering the a larger interval and the normalization integral has thus a larger value. As a result the normalized spectra are in theory less sensitive to small differences in the exact choice of the normalization range. However, only the L_2-edge contributes for energy losses larger than about 740 eV, which has in consequence a greater weight on the normalization value. The last choice is the least justified choice for the calculation performed in this work since only edge is calculated in this interval and the numerical value of the post-edge integral is rather small, making the spectra more sensitive to the post-edge normalization. The influence of these choices for the post-edge normalization range on a range of signals is considered throughout chapter 5.

4.2.3 *Difference methods for EMCD extraction*

Generally one can extract EMCD via one of three methods in the three-beam case geometry: single up-down difference, single left-right difference or a double difference method. It should be noted that apart from the double difference method these terms are not commonly used in the literature and will in this work only be defined for convenience.

The definition of the directions ”up”, ”down”, ”left”, and ”right” is furthermore somewhat arbitrary and done here with respect to a standard diffraction pattern in the three-beam case of a systematic row of Bragg spots: the x-axis is taken to point along the systematic row and go through the three Bragg spots. ”Right” is then the direction of the positive and ”left” the direction of the negative x-axis. The y-axis is perpendicular to the direction of the systematic row of Bragg spots and for a right-handed coordinate system ”up” corresponds to the positive and ”down” to the negative y-axis. Due to the tilt of the specimen the only true mirror plane of the diffraction pattern is the y-z-plane in the two- and three-beam case, whereas the x-z-plane is not a true mirror plane.

The naming scheme of *Thersleff at al.* is adopted for the four distinct detector positions in the three-beam case [7]: pp, pm, mp, and mm. The single up-down difference is the only method one can use in the two-beam case geometry and was as such used in the first successfully reported EMCD measurement [2]. In the three-beam case the up-down difference eEMCD-signal becomes

$$\Delta\sigma_{\mathrm{ud}}(E) \equiv \mathrm{eEMCD}_{\mathrm{ud}}(E) = \sigma(pp, E) - \sigma(pm, E), \tag{4.11}$$

where

$$\sigma(pp,E)=\left.\frac{\partial\sigma}{\partial E}\right|_{pp}=\int_{\Omega(pp)}\frac{\partial^2\sigma}{\partial\Omega\partial E}\,\mathrm{d}\Omega\,, \tag{4.12}$$

where Ω_{pp} is the scattering angle covered by the detector at position pp in the diffraction pattern. Since the DDSCS is a linear function of the MDFF one can split the signal at the detector up according to

$$\sigma(pp,E)=\sigma_{\mathrm{re}}(pp,E)+\sigma_{\mathrm{im}}(pp,E), \tag{4.13}$$

where $\sigma_{\mathrm{re}}(pp,E)$ and $\sigma_{\mathrm{im}}(pp,E)$ are the energy-integrated DDSCS due to the real part imaginary of the MDFF, respectively. The pEMCD-signal reads thus in the case of the up-down difference method

$$\Delta\sigma_{\mathrm{ud,im}}(E)\equiv\mathrm{pEMCD}_{\mathrm{ud}}(E)=\sigma_{\mathrm{im}}(pp,E)-\sigma_{\mathrm{im}}(pm,E) \tag{4.14}$$

The single left-right difference reads on the other hand

$$\Delta\sigma_{\mathrm{lr}}(E)\equiv\mathrm{eEMCD}_{\mathrm{lr}}(E)=\sigma(pp,E)-\sigma(mp,E). \tag{4.15}$$

Generally, an EMCD-signal extracted by means of the double difference method is more stable with respect to small misalignments of the specimen and it is thus the preferred extraction method today [5]. The eEMCD-signal reads in this case

$$\begin{aligned}\Delta\sigma_{\mathrm{dd}}(E)&\equiv\mathrm{eEMCD}_{\mathrm{dd}}(E)\\&=[\sigma(pp,E)+\sigma(mm,E)]-[\sigma(pm,E)+\sigma(mp,E)]\,.\end{aligned} \tag{4.16}$$

The expressions for the pEMCD- and eEMCD-signal carry over top the left-right and double difference method as

$$\Delta\sigma_{\mathrm{lr,im}}(E)\equiv\mathrm{pEMCD}_{\mathrm{lr}}(E)=\sigma_{\mathrm{im}}(pp,E)-\sigma_{\mathrm{im}}(pm,E) \tag{4.17}$$

$$\begin{aligned}\Delta\sigma_{\mathrm{dd,im}}(E)\equiv&\mathrm{pEMCD}_{\mathrm{dd}}(E)\\=&[\sigma_{\mathrm{im}}(pp,E)+\sigma_{\mathrm{im}}(mm,E)]\\&-[\sigma_{\mathrm{im}}(pm,E)+\sigma_{\mathrm{im}}(mp,E)].\end{aligned} \tag{4.18}$$

4.3 EXTRACTION OF THE RATIO OF ORBITAL AND SPIN MAGNETIC MOMENT

Using sum rules for EMCD [35–37] one finds for the ratio of the orbital magnetic moment m_L to the spin magnetic moment m_S

$$\frac{m_L}{m_S}=-\frac{2}{3}\frac{\int_{L_3+L_2}\Delta\sigma(E)\,\mathrm{d}E}{2\int_{L_3+L_2}\Delta\sigma(E)\,\mathrm{d}E-3\int_{L_3}\Delta\sigma(E)\,\mathrm{d}E}=\frac{2q}{9p-6q}, \tag{4.19}$$

where

$$p=\int_{L_3}\Delta\sigma(E)\,\mathrm{d}E\,, \tag{4.20}$$

$$q=\int_{L_3+L_2}\Delta\sigma(E)\,\mathrm{d}E\,. \tag{4.21}$$

$\Delta\sigma(E)$ is thereby the EMCD-signal. Experimentally q is determined by averaging the energy-integrated EMCD-signal according to

$$q = \frac{1}{E_{q+} - E_{q-}} \int_{E_{q-}}^{E_{q+}} \Delta\sigma(E)\,\mathrm{d}E\,. \tag{4.22}$$

over an interval $[E_{q-}, E_{q+}]$ of the post-edge region. A common choice is to set $[E_{q-}, E_{q+}] \equiv [E_-, E_+]$, i.e., to use the same interval for post-edge normalization and q-averaging.

The m_L/m_S-ratio is a quantity that can be directly compared to experiments and it should thus be a good indicator for the influence of non-dipole transitions in practice.

The extracted value of the m_L/m_S-ratio depends also on the extraction procedure and experimental values of 0.22 to 0.02, 0.12 to 0.10 and 0.08 have been reported for the single up-down, single left-right and double difference method, respectively [6]. The value for the double difference method is thereby slightly larger in comparison with m_L/m_S-ratios obtained from other measurement techniques such as XMCD or neutron scattering [5]. Simulations have yielded values of 0.19 to −0.11, 0.071 to 0.003 and 0.036 for the up-down, left-right and double difference methods, respectively [6].

5

SIMULATION RESULTS

This chapter deals with the computational results of this work and their discussion. The aim is to investigate the effect of non-dipole transitions on the (extracted) eEMCD-signal. The procedure is thereby the following: First the main features of simulated spectra at different approximation levels of the MDFF are compared with experiment in section 5.1.

Thereafter edge-resolved energy-integrated maps of the pEMCD- and eEMCD-signal are compared to each other in section 5.2 in order to spot differences in the angular distribution of the signals that might be attributable to non-dipole effects.

Section 5.3 continues with the investigation of non-dipole effects by considering the energy-dependence of the contributions of the strongest cross terms to the pEMCD- and eEMCD-signal.

The ratio of the orbital magnetic moment to the spin magnetic moment m_L/m_S is one of the key quantities that are directly accessible from the EMCD-signal as described in section 4.3. Computing m_L/m_S as a function of approximation level and experimental parameters should enable one to quantify the effect of non-dipole terms on the EMCD-signal and possibly on how to avoid them. The results of such calculations are included in subsection 5.4.

It will, however, become apparent that the shape of the post-edge region of the calculated spectra is of such form that experimental procedures such as the choice of the post-edge normalization region and the averaging range for determining the q-parameter (c.f. equation (4.22)) have a much stronger influence on the value of the extracted m_L/m_S-ratio than it is seen in experiments. Furthermore it is found that the calculated DDSCS exhibits a phenomenon that shall be called an *apparent anisotropy* which stems from an incomplete cancellation of the real part of the MDFF. The apparent anisotropy is analyzed and discussed further in section 5.5.

5.1 SIMULATED ELNES-SPECTRA AND EMCD-SIGNALS: GENERAL FEATURES

This section is dedicated to the description of some general features of the calculated ELNES-spectra and the extracted EMCD-signal. Emphasis is thereby put on similarities and differences to experimental spectra. Figure 5.1 displays two experimental ELNES-spectra of the L_3- and L_2-edge of bcc-iron measured by *Thersleff et al.* at a thickness of 50 nm using a convergent electron beam [7]. Furthermore a collection angle β = 8.5 mrad is used and the EMCD-signal is extracted by the double difference method. The *even* spectrum corresponds to the spectrum measured at the detector positions *pp*=(17.0 mrad,

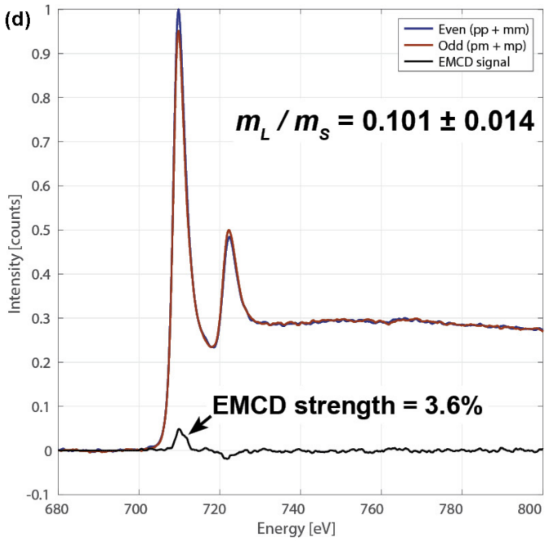

Figure 5.1: Example of ELNES-spectra for the L_3- and L_2-edge of bcc-iron and the extracted EMCD-signal measured in a double difference geometry. Refer to the main text for further details. Reprinted figure with permission from *Thersleff et al.*, Phys. Rev. B **94**, 134430 [7]. Copyright 2016 by the American Physical Society.

17.0 mrad) and *mm* (c.f. section 4.2). The *odd* spectrum is on the other hand measured at positions *pm* and *mp*.

The even and the odd spectra show a sharp onset of the L_3 edge at about 708 eV in figure 5.1. The intensity of the L_3-edge is larger in the even spectrum than in the odd spectrum. At the L_2-edge the odd spectrum is more intense than the even one but the difference is smaller than at the L_3-edge. These differences between both spectra give rise to the EMCD-signal, which is obtained as the difference of both spectra as explained in section 4.2. The EMCD-signal is stronger at the L_3-edge than at the L_2-edge, where it is of magnitude comparable to the noise, which is a common observation in experiments.

The last feature of the experimental spectrum that is of importance for the remainder of this chapter is the shape and intensity of the post-edge region of the spectrum. It is somewhat featureless and nearly constant up to about 765 eV. The relative intensity of the post edge region is in comparison to the cumulative intensity below the L_3- and L_2-edge is as a result relatively large and choosing a post-edge normalization range of [730 eV, 740 eV] shouldn't give much different results than choosing it as [730 eV, 750 eV].

After considering some of the features commonly seen in experiments the attention is in the following put on the simulated spectra: figure 5.2 and figure 5.3 display simulated spectra calculated in dipole and in lamb3-approximation of the MDFF, respectively. The simulated spectra show similarly the L_3 and L_2-edge as the two main peaks and reproduce the differing peak heights well. However, the general shape differs quite substantially from the spectra depicted in figure 5.1. The onset of the L_3-edge is less sharp in comparison with these experimental spectra. The Lorentz broadening function is said to have *heavy tails*, i.e., it falls rather slowly to zero far away from the central maximum.

Another apparent difference is the appearance of a smaller intermediate peak between the L_3- and L_2-edge peak. This peak in the simulation is explained by the features of the DOS for energies 7 eV to 8 eV above the Fermi level in both spin-channels. The DOS has a rather large peak in this energy range according to figure 3.1c and contributes a peak to the raw DDSCS of the L_3-edge at an energy loss of about 715 eV to 717 eV as depicted in figure 4.2.

Another difference between experimental spectrum and simulation regards the post-edge region. In the simulations the postedge region is characterized by a decreasing background as the electron loss energy increases. On top of this decreasing background two peaks are superposed at energy losses between 730 eV to 740 eV. The shape of the experimental spectrum is in contrast nearly constant over a large part of the post-edge region as described before.

Comparing the subfigures of figure 5.2 and 5.3 one notes that the spectral shape is similar for the dipole- and lamb3-approximation. The spectra show as well similar features such as the peaks between the L_3- and L_2-edge and in the post-edge region.

The post-edge normalization achieves in figures 5.2b, 5.2c, 5.3b, and 5.3c that the spectra for even and odd detector positions coincide in the post-edge region for energy losses above about 735 eV. It does thereby not matter much if the normalization region is chosen as [730.0 eV, 740.0 eV] or [730.0 eV, 750.0 eV].

Turning to the discussion of the EMCD-signal one notes that the shape and relative intensity of the pEMCD-signal is not changed much by applying a post-edge normalization. The eEMCD-signal on the other hand is strongly affected by applying a post-edge normalization: In the case without normalization the pEMCD-signal and eEMCD-signal agree well at the L_2 edge. Applying the post-edge normalization shifts the eEMCD-signal upwards and the negative valued signal at the L_2-edge disappears almost entirely. This is independent of the exact choice the post-edge normalization region. A similar observation is made at the L_3-edge, where the positive signal at the L_3-edge gets enhanced by the post-edge normalization. At the L_3-edge, however, the agreement between the pEMCD- and eEMCD-signals is worse than at the L_2 edge. In the region between the edges the eEMCD-signal is furthermore larger and has a different shape compared to the pEMCD-signal.

The pEMCD-signals have very similar shape and relative intensity for dipole- and lamb3-approximations of the MDFF. The eEMCD-signal is similar to the pEMCD-signal in strength and general shape in the case of no applied post-edge normalization. However, by applying a post-edge normalization the eEMCD-signal in dipole approximation is mainly shifted upwards and the dip in the signal at the L_2-edge weakens a bit and in lamb3-approximation the signal at the L_2-edge is almost entirely suppressed. The signal at the L_3-

edge is on the other hand greatly enhanced by post-edge normalization. A poor cancellation of non-dipole terms by the post-edge normalization could explain these large differences between the dipole and lamb3-approximation with respect to the post-edge normalization.

The emphasis has so far been on the differences between the pEMCD- and eEMCD-signals. However comparing the shape of the pEMCD- and eEMCD-signal in dipole and lamb3 approximation (figures 5.2, 5.3) to the shape of the experimental EMCD-signal depicted in figure 5.1 one notes that the agreement between the shape of the signals is closest in the case of an applied post-edge normalization and lamb3-approximation: in the experimental and the simulated signals the signal at the L_2-edge is suppressed. Perhaps this is the first step to an explanation of the origin of the suppressed L_2-edge feature often seen in experiments. The signal at the L_3 edge, however, is a lot stronger in the simulation than in experiment. It should be noted here that it is a reassuring result that the most realistic simulation (lamb3, applied post-edge normalization) comes closest to the experiment but a couple of open issues remain, first and foremost the shape of the post-edge region and the magnitude of the post-edge integral in (4.7).

The reason for the different shapes of the post-edge region is not clear at the moment and one could improve upon the description of the post-edge region in several ways, all of which are aimed at increasing the relative ELNES-intensity in the post-edge region: as noted before the broadening scheme could be revised by adding an additional energy-dependent broadening as explained in section 4.2.1. Furthermore the description of the unoccupied cross-DOS could be improved upon by, e.g., adding additional LOs above the Fermi level to the LAPW-basis in the electronic structure calculation. Lastly the cross-DOS post-edge region could be calculated for a larger energy range at the cost of an increased linearization error in LAPW for these high-lying post-edge states.

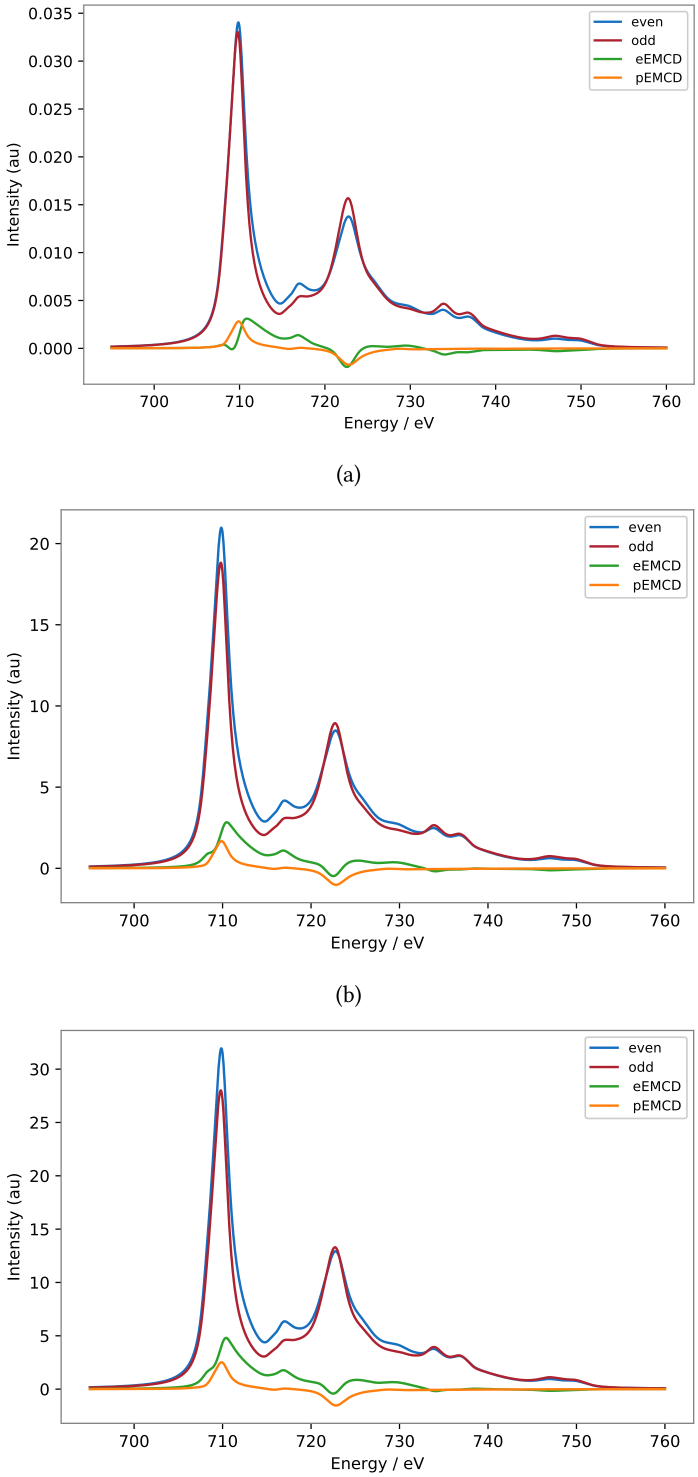

(a)

(b)

(c)

Figure 5.2: Simulated spectra for a dipole approximation of the MDFF at thickness 15 nm: in subfigure (a) no post-edge normalization is applied. In subfigure (b) and (c) the post-edge normalization range is set to [730.0 eV, 740.0 eV] and [730.0 eV, 750.0 eV], respectively. The spectra are labeled in the same way as in figure 5.1 for easier comparison. The collection angle is set to 8.0 mrad and the *pp* detector position is set to a scattering angle of (17.0 mrad, 17.0 mrad). *pm*, *mp*, and *mm* follow accordingly.

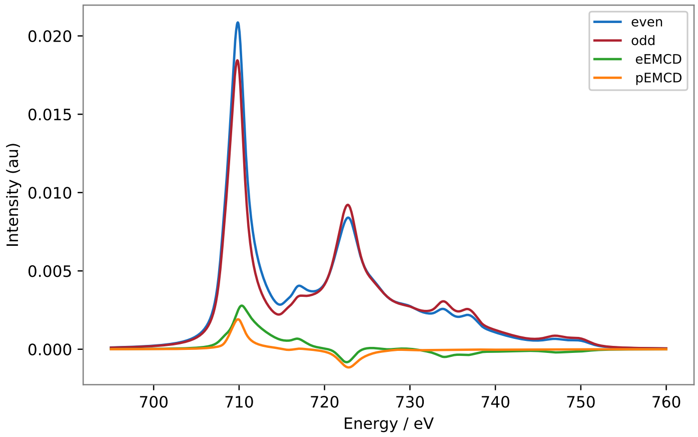

(a) no penorm

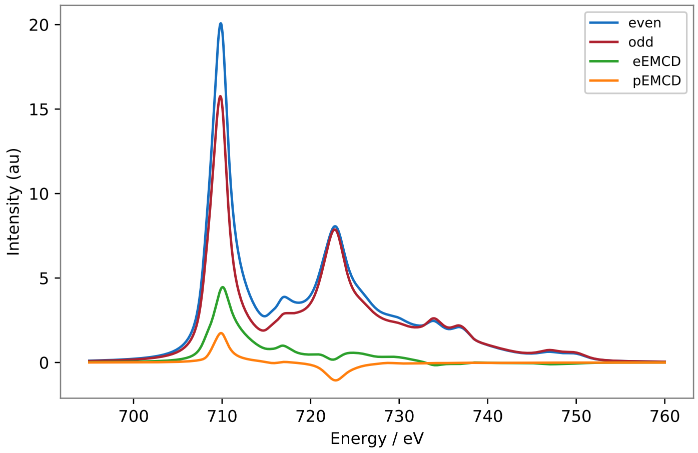

(b) [730.0 eV, 740.0 eV]

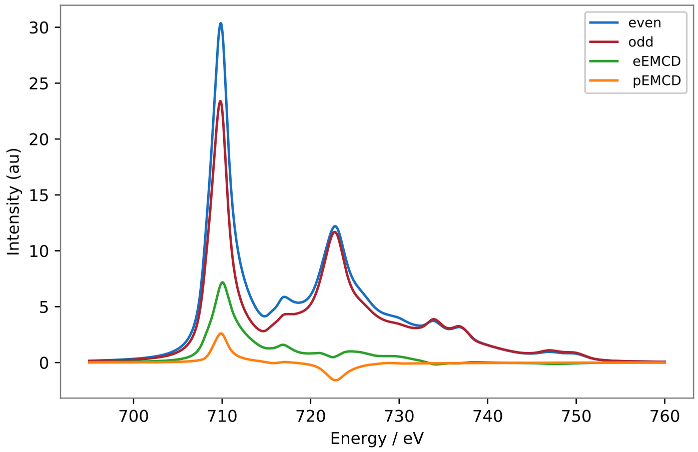

(c) [730.0 eV, 750.0 eV]

Figure 5.3: Simulated spectra, eEMCD- and pEMCD-signal for a lamb3-approximation of the MDFF at thickness 15 nm: no post-edge normalization is applied in subfigure (a). In subfigure (b) and (c) the post-edge normalization range is set to [730.0 eV, 740.0 eV] and [730.0 eV, 750.0 eV], respectively. Refer to the caption figure 5.2 for other details.

5.2 MAPS OF THE ENERGY-INTEGRATED EMCD-SIGNAL

Edge-resolved maps of the unbroadened energy-integrated pEMCD-signal extracted from the 11-diagonal term of the MDFF and from the MDFF in dipole-, and lamb3-approximation are depicted in figure 5.4 at a thickness of 15 nm. Maps of the unbroadened energy-integrated pEMCD-signal for thicknesses 10 nm and 20 nm are displayed in figures A.1 and A.2 in appendix A.1. These maps show the strength of the pEMCD-signal as a function of the scattering angle (θ_x, θ_y).

The pure EMCD (pEMCD)-signal at the L_3-edge is in comparison to the signal at the L_2-edge of opposite sign in the four quadrants of the diffraction pattern. It varies furthermore smoothly with respect to the scattering angle and is strongest for scattering angles lying on or close to the Thales circle. The signal localizes with increasing thickness around the center position of the Thales circle and an additional narrow region of non-zero EMCD-signal starts to appear at a thickness of 20 nm. These findings are in very good agreement with results from other calculations [38, p. 210].

The maps of the pure EMCD (pEMCD)-signal extracted from the dipole-approximated MDFF, the 11-term and the lamb3-approximation to the MDFF are visually almost indistinguishable. Upon close inspection the signal seems to be generally a bit stronger in dipole-approximation than in the case of the bare 11-term and the lamb3-approximation. The pure EMCD (pEMCD)-signal due to the 11-term is visually indistinguishable from the pure EMCD (pEMCD)-signal due to the lamb3-approximation. This means that the imaginary part of the MDFF is almost solely attributable to the dipole or 11-term and non-dipole terms do not contribute substantially in lamb3-approximation.

Figure 5.5 displays edge-resolved maps of the energy-integrated, unbroadened eEMCD-signal calculated for the same parameters as in figure 5.4. Appendix A.1 contains additionally maps of the unbroadened energy-integrated eEMCD-signal for thicknesses 10 nm and 20 nm, which are displayed in figures A.3 and A.4, respectively.

The maps of the unbroadened energy-integrated pEMCD-signal at the L_3-edge are to be discussed: in comparison with the pEMCD-signal in figure 5.4 the eEMCD-signal is much stronger at across all approximation-levels of the MDFF. The shape of the signal is furthermore much different. It exhibits a pronounced x-shaped feature at the center of the maps which connects at larger scattering angles with a region of stronger signal, which are similar in shape to the regions seen in the maps of the pEMCD-signal.

At the L_2-edge the eEMCD-signal is overall much weaker than it is at the L_3-edge. It exhibits furthermore four dot-shaped features at the center of the maps. These features are not connected to the regions of stronger signal close to the Thales circle, which are similar in shape to the regions seen in figure 5.4. However, one notes that the sign between the four dot-shaped features and the eEMCD-signal differs in all four quadrants of the diffraction plane. The dots have the same sign in the quadrants as the EMCD-signal at the L_3-edge has.

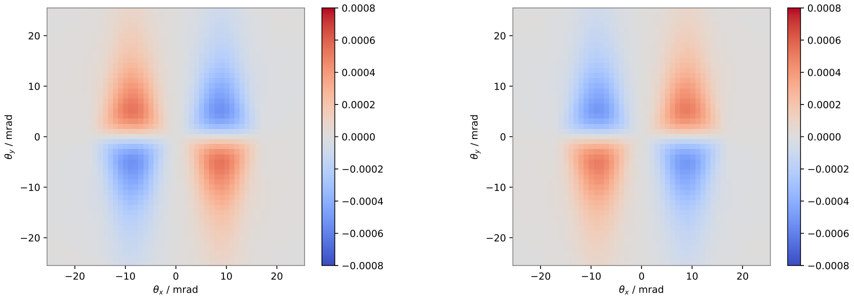

(a) dipole-approximation @ L_3-edge

(b) dipole-approximation @ L_2-edge

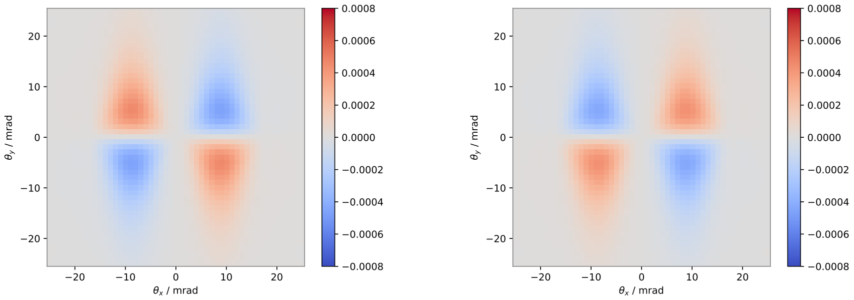

(c) 11-diagonal term @ L_3-edge

(d) 11-diagonal term @ L_2-edge

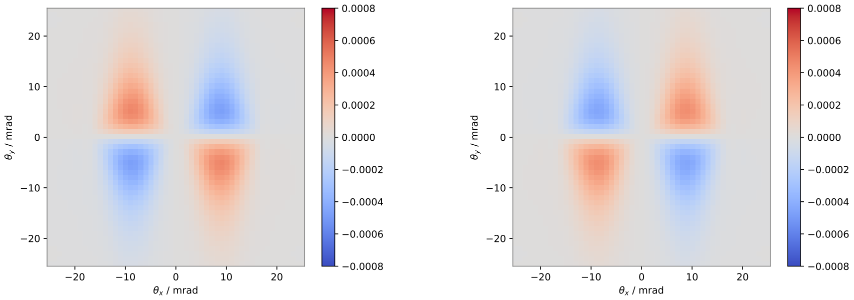

(e) lamb3-approximation @ L_3-edge

(f) lamb3-approximation @ L_2-edge

Figure 5.4: Edge-resolved comparison of maps of the unbroadened energy-integrated pEMCD-signal computed using different approximation levels of the MDFF as indicated in the captions of the subfigures. All maps are calculated using the double difference method at thickness 15 nm.

The maps of the unbroadened energy-integrated pEMCD-signal look very similar in shape for all considered approximation levels in figure 5.4. The signal calculated using the dipole-approximation seems to be the strongest, especially for large scattering angles in y-direction.

These results for the pEMCD-signal show overall that the calculated DDSCS data-cuboid contains an anisotropy due to the imaginary part of the MDFF, i.e., it contains an EMCD-signal. The eEMCD-signal is furthermore found to be substantially different from the pEMCD-signal. The difference between both types of EMCD-signal can be attributed to an incomplete cancellation of the real part of MDFF in the dipole- and 11-term, since no cross terms contributes to these signals. In section 5.5 this *apparent anisotropy* of the real part of the MDFF is analyzed in more detail.

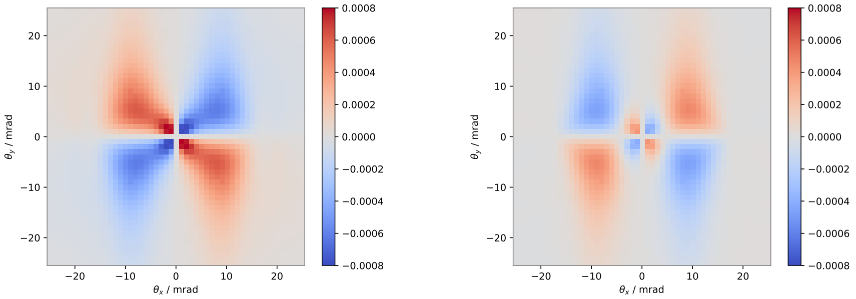

(a) dipole-approximation @ L_3-edge (b) dipole-approximation @ L_2-edge

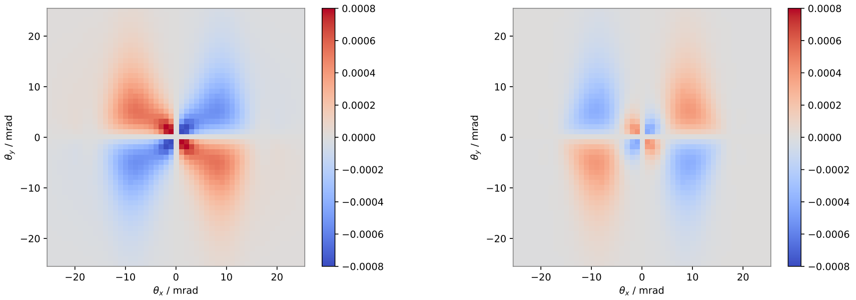

(c) 11-diagonal term @ L_3-edge (d) 11-diagonal term @ L_2-edge

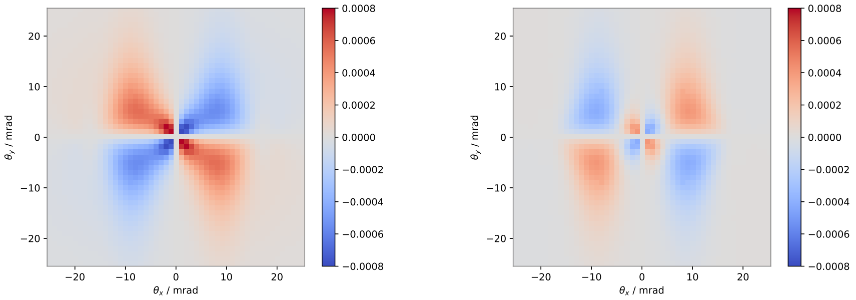

(e) lamb3-approximation @ L_3-edge (f) lamb3-approximation @ L_2-edge

Figure 5.5: Edge-resolved comparison of maps of the unbroadened energy-integrated eEMCD-signal computed using different approximation levels of the MDFF as indicated in the captions of the subfigures. All maps are calculated using the double difference method at thickness 15 nm.

5.3 NON-DIPOLE CONTRIBUTIONS TO THE EMCD-SIGNAL

In figure 5.6 the contributions of the main cross terms of the MDFF to the eEMCD-signal are compared to the lamb3- and dipole-approximations for the difference methods discussed in section 4.2.3. The detector is thereby centered around scattering angle θ_x, θ_y =(9.0, 9.0) in the diffraction pattern and covers a collection angle of β = 5.0 mrad. In general all difference methods show a signal of similar overall shape for the 11 cross term and in dipole- and lamb3-approximation. The signal for the double difference method is thereby about twice as strong as it is for the other two methods.

At closer inspection, however, one notes a difference for the 01 term: it contributes substantially over a wide range of energy-losses to the signal at the L_2-edge for the single up-down method. Using the single left-right difference method removes this contribution of the 01 term to a large extent and it is practically canceled out by the double difference method. This suggests that the 01 cross term exhibits an asymmetry under mirroring on the x-axis. But it is more or less symmetric under mirroring at the y-axis.

The 13 cross term on the other hand contributes substantially at the L_3-edge for all difference methods which suggests that it has similar symmetry properties as the EMCD-signal itself. It should be mentioned that the contributions due to all calculated cross terms other than 01 an 13 are basically zero at detector position $\theta_x, \theta_y = (9.0, 9.0)$ and they are thus not shown in figure 5.6. This is interesting insofar as that the 13 term contributes more strongly than for example the 12 term that could be anticipated to be larger due to being of lower order in λ, λ'.

The dipole- and 11-term coincide over the whole range of energies but in close vicinity around the minimum and maximum of the signal for the single up-down difference. This behavior has been observed before [10]. Moving to the single left-right difference, the difference between the dipole- and 11-term remains around the minimum and maximum of the signal. Both signals start to differ additionally in the region between the edges. In the case of the double difference method on the other hand, dipole and 11-term coincide everywhere but in close vicinity around the L_3-edge.

Considering the lamb3-signal one notes that the signal coincides with the 11 term at the L_2-edge for the double difference method. At the L_3 edge, however, a difference between the lamb3-signal and the 11 contribution of similar relative magnitude to the difference in the case of the single left-right difference method remains. The lamb3-signal is furthermore always smaller than the dipole-signal but the difference is small except for the close vicinity of the L_2 and L_3-edge for the single left-right and double difference method.

These results suggest the double difference method is effectively suppressing the effects of non-dipole transitions at the L_2 edge for a detector centered around scattering angle $\theta_x, \theta_y = (9.0, 9.0)$ and collection angle of β = 5.0 mrad. This result is not too surprising given that the double difference method is considered to be superior to the other two methods as mentioned in section 4.2.3. It might, however, shed new light on the more fundamental reasons of why that is the case. The double difference method does not deliver a satisfactory suppression of the 13 cross term at the L_3 edge for the considered detector centered around scattering angle $\theta_x, \theta_y = (9.0, 9.0)$ and collection angle of $\beta = 5.0\,\mathrm{mrad}$, however. Lastly it remains to be seen how influential the difference between the dipole- and lamb3-approximations is in the evaluation of the m_L/m_S-ratio in section 5.4 before a conclusive answer can be given to the question of which approximation one should use in the future for highly precise calculations and experiments.

Figure 5.7 is to be discussed to the end of this section, where the largest contributions of all cross terms are compared to the dipole-approximation and the lamb3-approximations at detector position $\theta_x, \theta_y = (17.0, 17.0)$ and collection angle $\beta = 5.0\,\mathrm{mrad}$. More cross terms contribute to for the single up-down and the single left-right difference method and their relative contribution across all difference methods is much larger compared to figure 5.6. However, moving then from the single up-down to the single left-right to the double difference method the contributions of the cross terms 01 and 12 are successively diminished and the same terms as in figure 5.6 contribute to the signal. The relative magnitude of the signal due to the 13 cross term is a lot larger compared with figure 5.6 and it does as well contribute substantially at the L_2-edge.

Dipole- and lamb3-approximation differ significantly at this detector position, especially at the L_2 edge where the lamb3-signal is strongly suppressed with respect to the dipole-approximation and the 11-term. This might be part of the explanation why the L_2 edge is often seen to be suppressed in experiments as detailed in section 5.1 and suggests furthermore that at least the lamb3-approximation is required for precise calculations at large scattering angles. This result is not too surprising either given that the dipole approximation according to equation 1.1 requires the product $\mathbf{q} \cdot \hat{\mathbf{R}}$ to be small. It is thus expected to perform worse than the Rayleigh expansion at larger scattering angles and these results suggest that the difference is substantial. It remains to be seen, however, how this effects the extraction of the m_L/m_S-ratio in section 5.4.

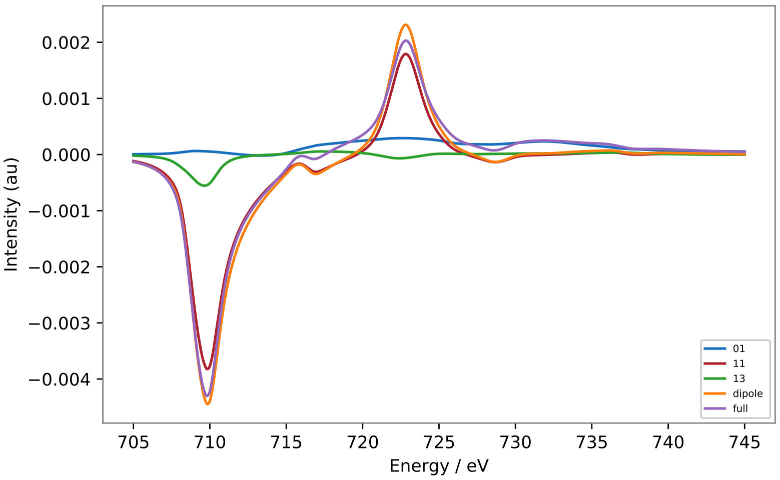

(a) single up-down difference

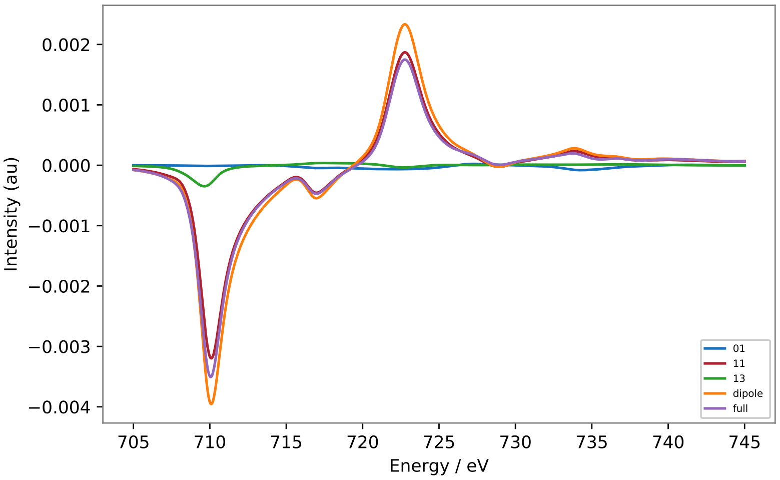

(b) single left-right difference

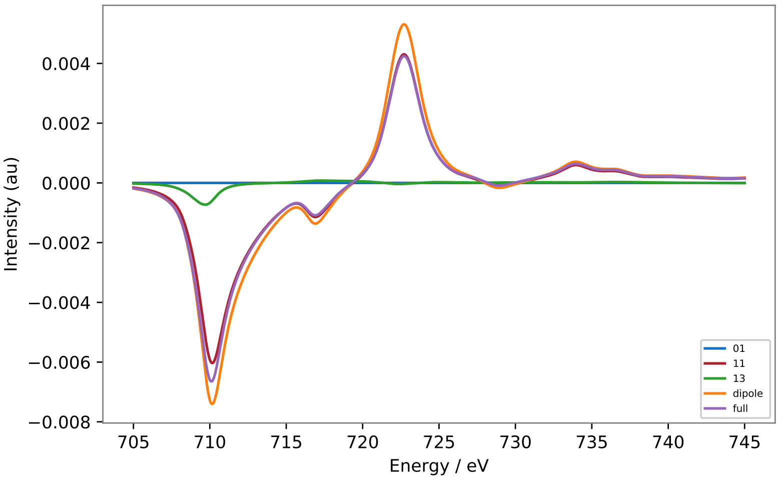

(c) double difference method

Figure 5.6: Comparison of the contributions of the main cross terms to the eEMCD-signal and the eEMCD-signal in dipole- and lamb3-approximation for different extraction methods at thickness 15 nm. The *pp* detector is centered around scattering angle $\theta_x, \theta_y = (9.0, 9.0)$ in the diffraction pattern and the collection angle is $\beta = 5.0$ mrad. No post-edge normalization is applied and the legend key *full* refers to the lamb3-approximation.

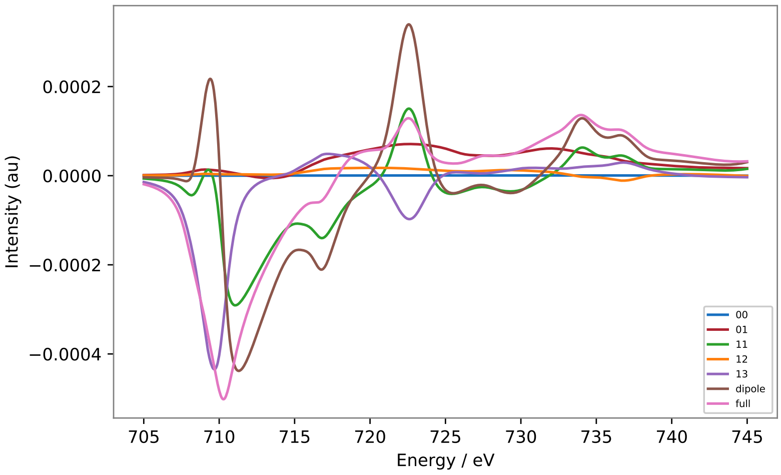

(a) single up-down difference

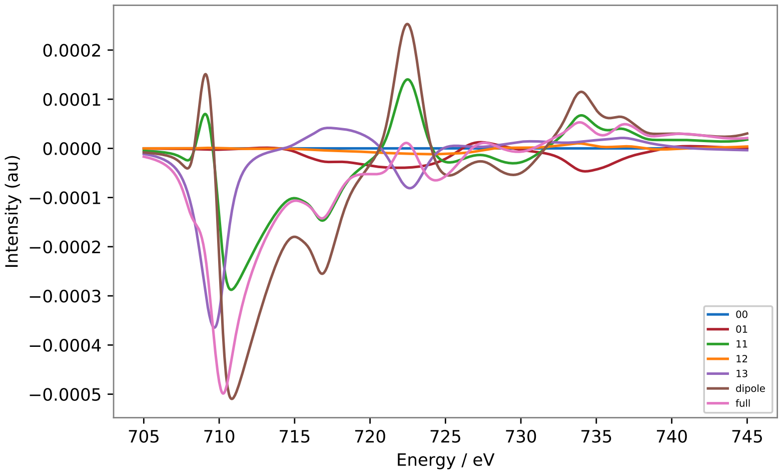

(b) single right-left difference

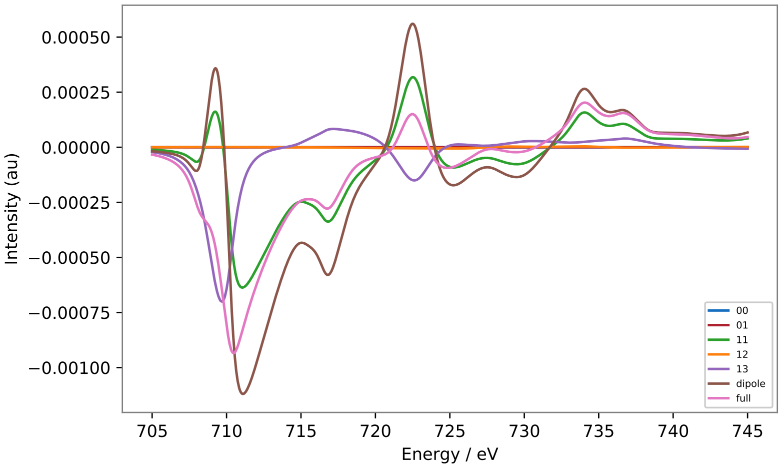

(c) double difference method

Figure 5.7: Comparison of the contributions of the main cross terms to the eEMCD-signal and the eEMCD-signal in dipole- and lamb3-approximation for different extraction methods at thickness 15 nm. The *pp* detector is centered around scattering angle $\theta_x, \theta_y = (17.0, 17.0)$ in the diffraction pattern and the collection angle is $\beta = 5.0$ mrad. No post-edge normalization is applied and the legend key *full* refers to the lamb3-approximation.

5.4 MAPS OF THE m_L/m_S-RATIO

In order to quantify the strength of the EMCD-signal and compare the influence of non-dipole transitions on the extraction of the magnetic signal maps of the m_L/m_S-ratio are calculated. The quantities that are varied include within each figure the detector collection angle $0 \leq \beta \leq 8$ and the post-edge normalization ranges, for which the ranges singled out in section 4.2.2 are considered. Apart from these parameters thicknesses of 10 nm to 20 nm are considered and three choices of the averaging range of q (c.f. equation (4.22)) are evaluated. Lastly three approximation levels to the MDFF are taken into account: dipole- and lamb3-approximation, and the 11-term. It is not instructive to consider all computed maps in this section and the majority of these maps is contained in appendix A.2. The maps of the m_L/m_S-ratio computed from the pEMCD- and eEMCD-signal are presented and discussed in subsections 5.4.1 and 5.4.2, respectively. In both subsections only the double difference method is featured and maps for the other difference methods are included in appendix A.2.

5.4.1 *m_L/m_S-ratio computed from pEMCD-signal*

Figures 5.8, 5.10, and 5.9 display m_L/m_S-maps computed from the pEMCD-signal in dipole-approximation and lamb3-approximation as well as computed from the 11-term of the MDFF, respectively. Overall a good agreement with the literature values of the m_L/m_S-ratio listed in section 4.3 is found.

In dipole-approximation the m_L/m_S-ratio does not depend strongly on the the scattering angle, i.e., the center position of the detector, or the detector size. In the case of the 11-term the m_L/m_S-ratio increases slightly at the boundaries of the calculated region of detector positions. These variations are slightly damped by an increased detector size. In comparison with the results for the dipole-approximation this means that the different shape of the 11-term has a (small) influence on the extracted m_L/m_S-ratio. In lamb3-approximation the m_L/m_S-ratio exhibits slightly lower values than the 11-term does within a narrow band that is almost parallel to the y-axis at the x-coordinate of $\mathbf{G}$. This means that (small) contributions from cross terms or higher-order diagonal terms affect the m_L/m_S-ratio compared. The effect of increased detector size is again a dampening of the variations.

Seemingly all maps exhibit a strong dependence of the numerical value of the m_L/m_S-ratio on the post-edge normalization range. However the averaging range for q (c.f. equation (4.22)) is equal to the post-edge normalization range in figures 5.8, 5.9, and 5.10 as it is often done in experiments. In order to single out the effect of the post-edge normalization the q-averaging range is kept at [745.0 eV, 750.0 eV] in figure 5.11.

Comparing the maps displayed in figure 5.11 to the ones in figure 5.10 one notes that the q-averaging range has a much bigger influence on the m_L/m_S-ratio extracted from the pEMCD-signal than the post-edge normalization range has.

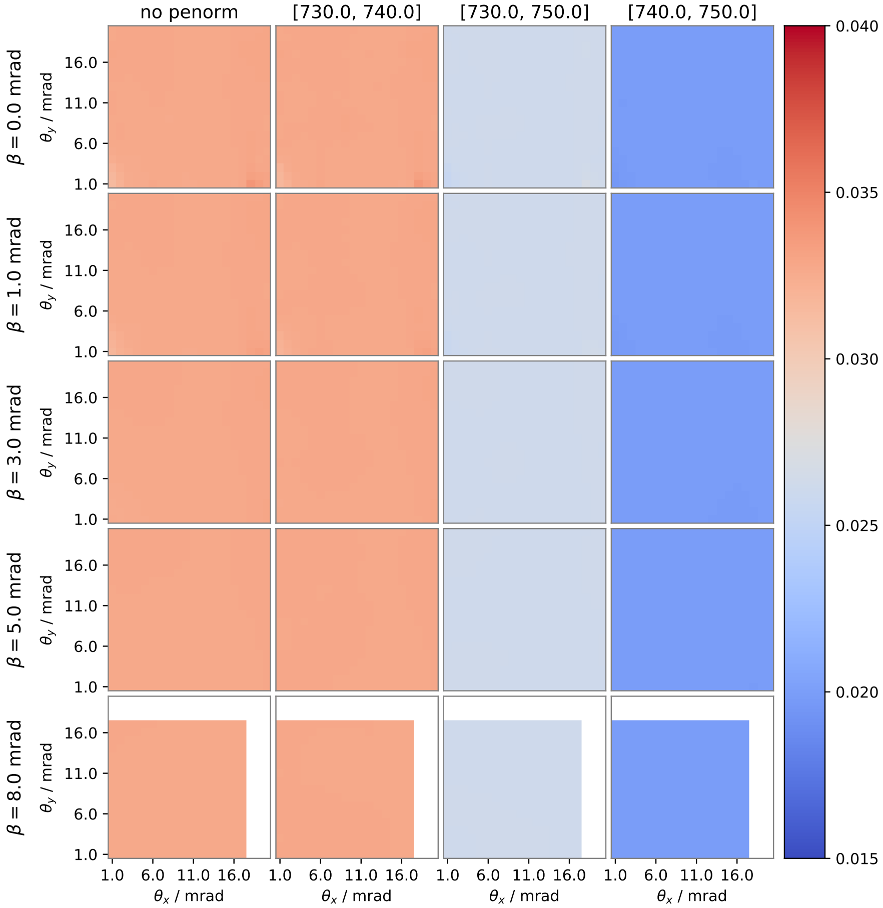

Figure 5.8: m_L/m_S-map calculated from the pEMCD-signal in dipole approximation at thickness of 15 nm and extracted by the double difference method: rows correspond to different detector collection angles β and columns to different post-edge normalization ranges. The first row (collection angle β=0.0 mrad) corresponds to the m_L/m_S-ratio at the exact pixel position, i.e. no integration over pixel is performed. The *no penorm*-tag indicates that no post-edge normalization was performed in the first column. The average of the energy integrated pEMCD for determination of q is taken over the post-edge normalization range (c.f. equation 4.19). In the case of no post-edge normalization the average is taken over the interval [730.0 eV, 740.0 eV]. Each pixel corresponds within a given map to the *pp* center-position (θ_x, θ_y) of the detector in the diffraction pattern. The value of the m_L/m_S-ratio is encoded as indicated by the color bar. White pixel correspond to values which lie outside of the bounds of the color bar or which are not computed due to only a partly overlap of the detector with the calculated region of the diffraction pattern.

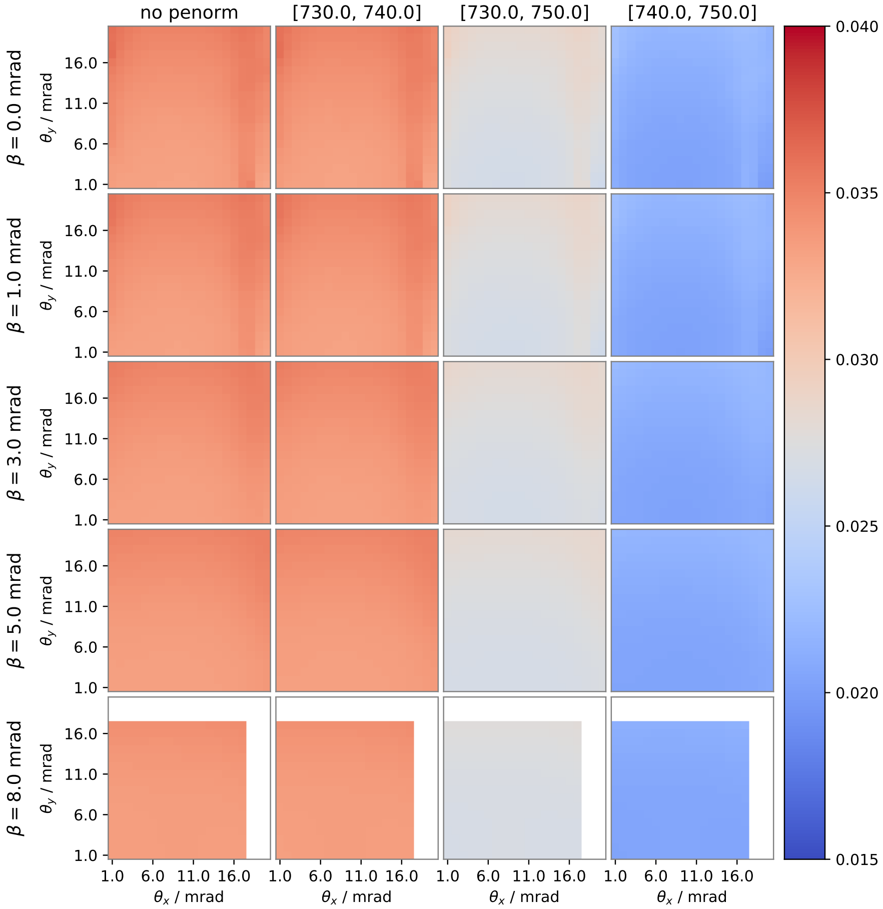

Figure 5.9: m_L/m_S-map calculated from the pEMCD-signal obtained from the 11-term of the MDFF at thickness of 15 nm and extracted by the double difference method. Refer to the caption of figure 5.8 for a detailed description of the technicalities of these maps.

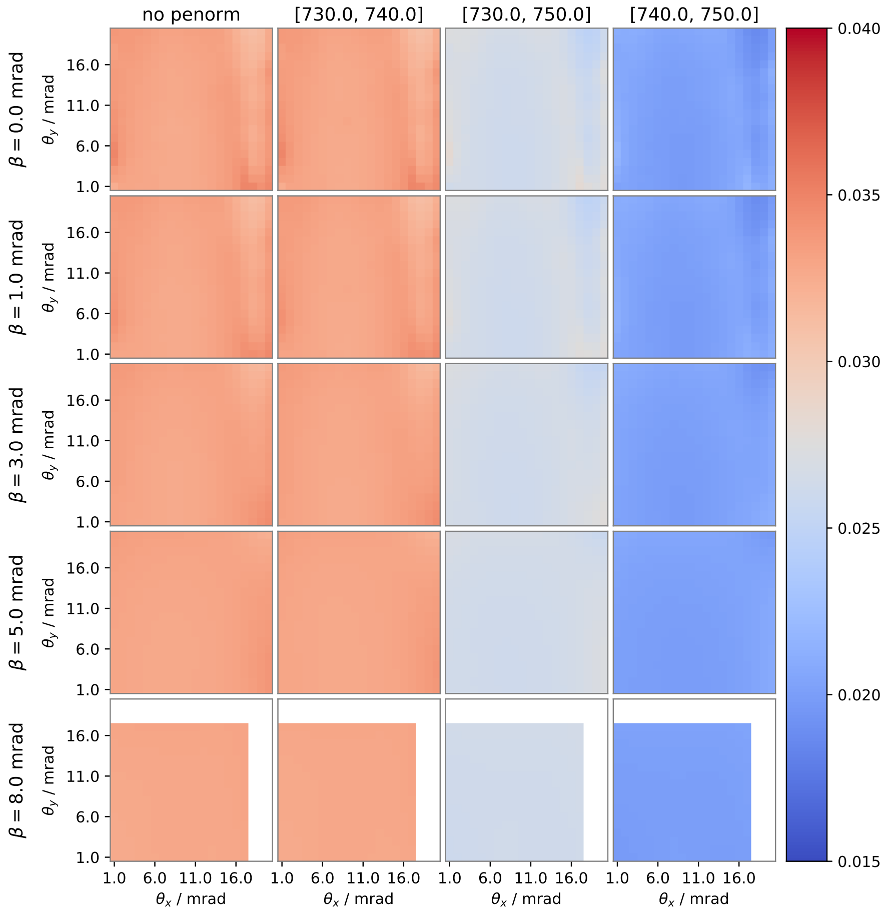

Figure 5.10: m_L/m_S-map calculated from the pEMCD-signal in lamb3-approximation at thickness of 15 nm and extracted by the double difference method. Refer to the caption of figure 5.8for a detailed description of the technicalities of these maps.

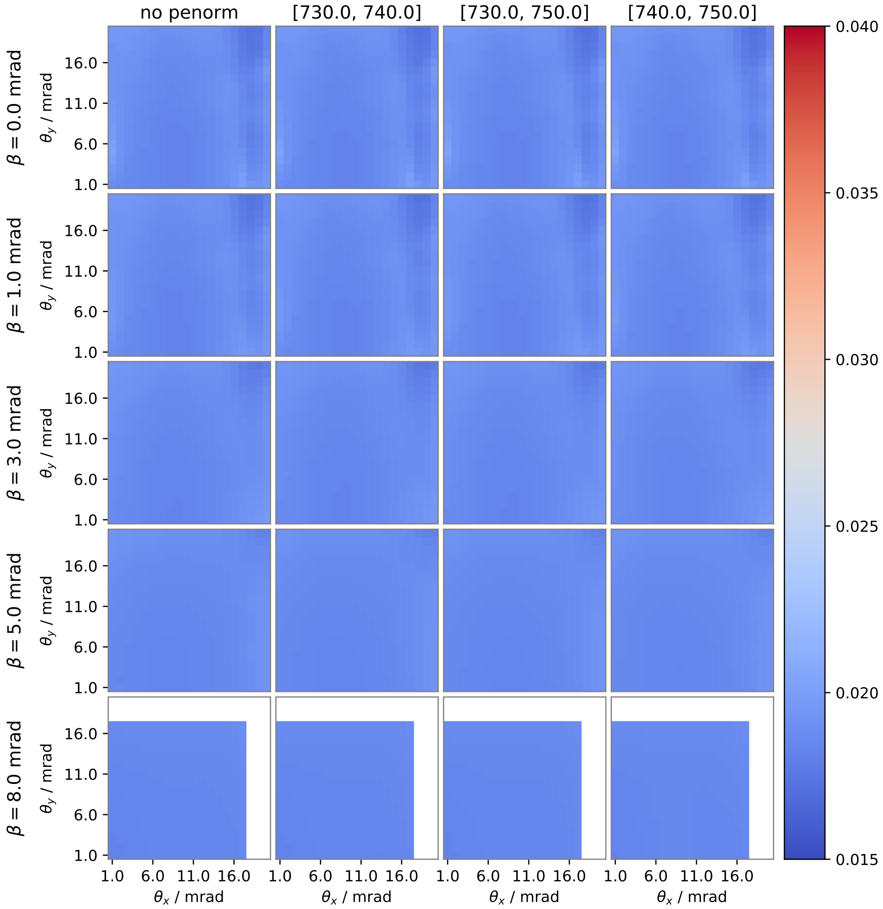

Figure 5.11: m_L/m_S-maps for the same parameters as figure 5.10 except that the q-averaging range (c.f. equation (4.19)) is set to [745 eV, 750 eV].

5.4.2 m_L/m_S-ratio computed from eEMCD-signal

Figures 5.12, 5.13, 5.14, and 5.15 contain maps of the m_L/m_S-ratio calculated for the same parameters and cases as figures 5.8, 5.9, 5.10 and 5.11 discussed in the previous section. It is apparent that the post-edge normalization has a large influence on the obtained m_L/m_S-ratio since a band of m_L/m_S-ratios is found in the case of no applied post-edge normalization, which is suppressed by the post-edge normalization procedure. Within this band the values of the m_L/m_S-ratio are comparable in magnitude to literature values listed in section 4.3.

Given the shape of these maps a discussion of non-dipole effects is not possible: The post-edge normalization has a much larger influence on the m_L/m_S-ratio than any non-dipole effect and the remainder of this chapter is thus focused on the post-edge normalization.

It is found here that the m_L/m_S-ratio is very sensitive to the choice of post-edge normalization for the pEMCD-signal. Experimentally the m_L/m_S-ratio depends on the choice for the post-edge normalization range but it is less sensitive to it.

As described in section 5.1, a major difference between the simulated and the experimental spectra regards the shape and magnitude of the spectrum in the post-edge region. The experimental spectra show a featureless, in good approximation constant post-edge region, whereas the theoretical spectra show a decreasing post-edge region exhibiting some spectral features. The integral over the post-edge region is furthermore in relation to the integral over the edge region considerably smaller in the simulated spectra than in the experimental one. As a result of these differences in the properties of the post-edge region, the simulated spectra are much more sensitive to the procedure of post-edge normalization than the experimental ones.

There are two options one might explore to move forward from this result. The first one is of empirical nature and orients itself on the procedure of *double step background* subtraction used in experiments. On the theoretical side one could *add* instead of subtract such a double-step background in order to obtain a post-edge region that is more in line with experimental reality. Such a procedure has been carried out with success in the past [39] but it lacks rigorous theoretical justification and would go beyond the scope of this thesis.

Alternatively one could go back to the fundamental processes that shape the post-edge region and improve their description in the present computational approach. Several possibilities on how this could be done have been proposed in section 5.1.

The large differences between the maps of the m_L/m_S-ratio presented in this section and the maps for the pEMCD-signal presented in the previous section cannot only be explained by effect of post-edge normalization as the maps of the eEMCD-signal show in the case of no applied post-edge normalization. These differences can only come from an incomplete cancellation of the real part of the MDFF. In section 5.2 this phenomenon was termed apparent anisotropy and more light will be shed on this in the next section.

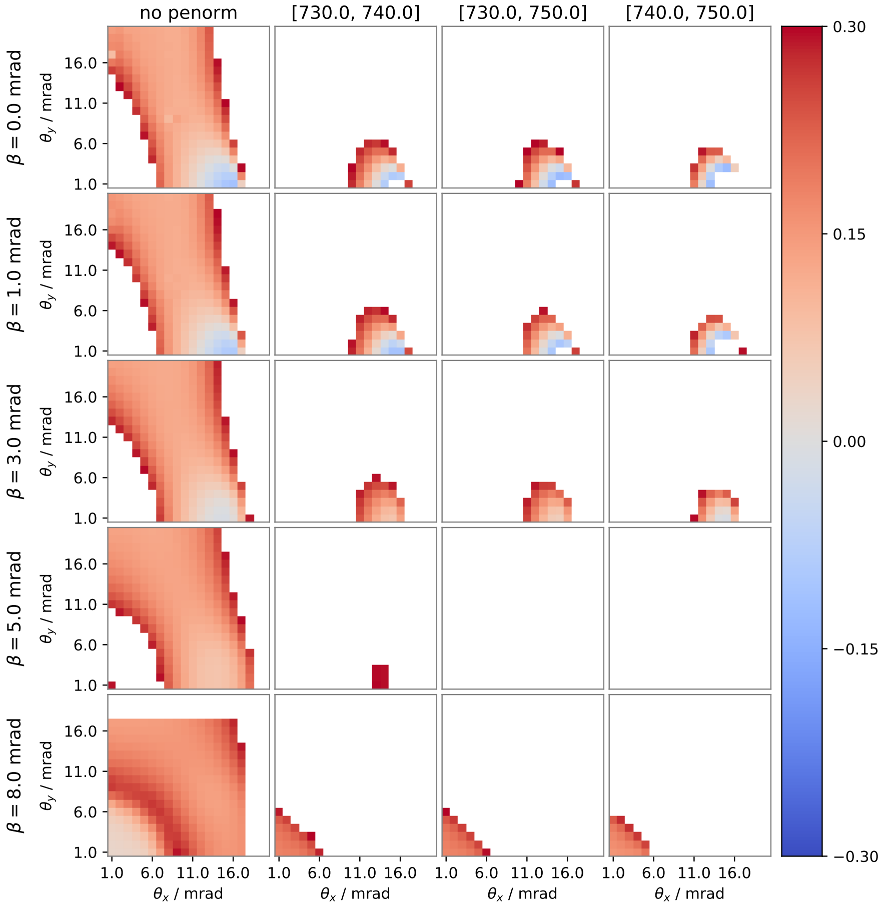

Figure 5.12: m_L/m_S-map calculated from the eEMCD-signal in dipole approximation at thickness of 15 nm and extracted by the double difference method. Refer to the caption of figure 5.8 for a detailed description of the technicalities of these maps. The q-averaging range (c.f. equation (4.19)) is equal to the post-edge normalization range except for the column, in which no post-edge normalization is applied and it is set to [730 eV, 740 eV].

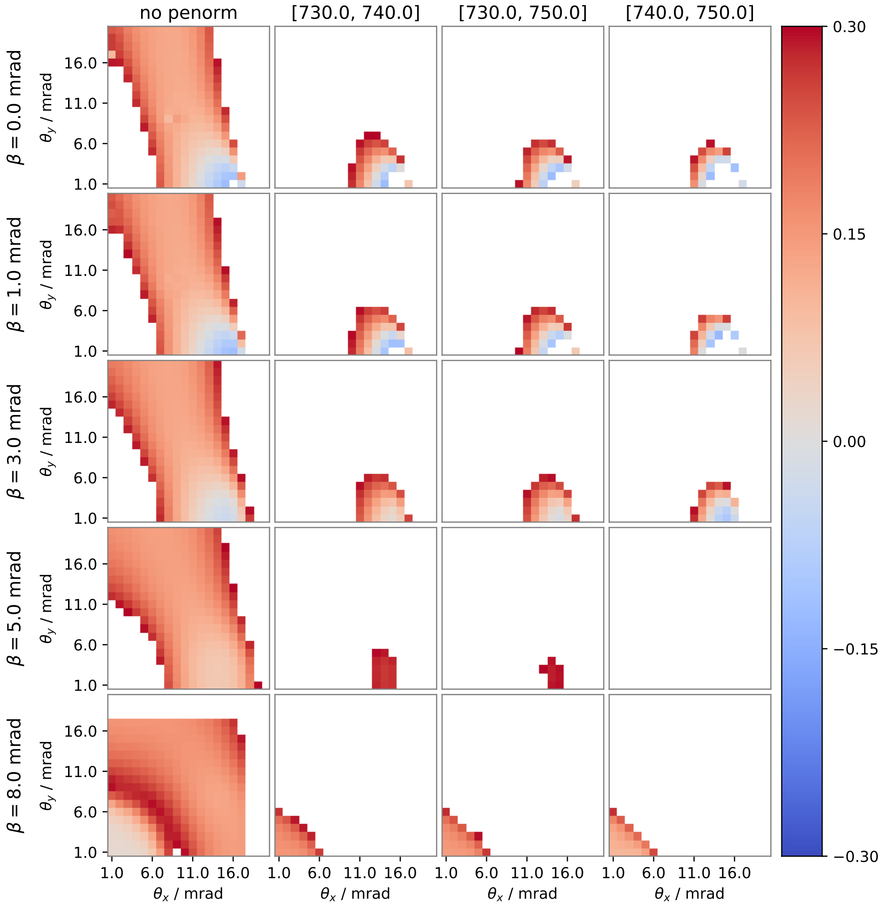

Figure 5.13: m_L/m_S-map calculated from the eEMCD-signal obtained from the 11-term at thickness of 15 nm and extracted by the double difference method. Refer to the caption of figure 5.8 for a detailed description of the technicalities of these maps. The q-averaging range (c.f. equation (4.19)) is equal to the post-edge normalization range except for the column, in which no post-edge normalization is applied and it is set to [730 eV, 740 eV].

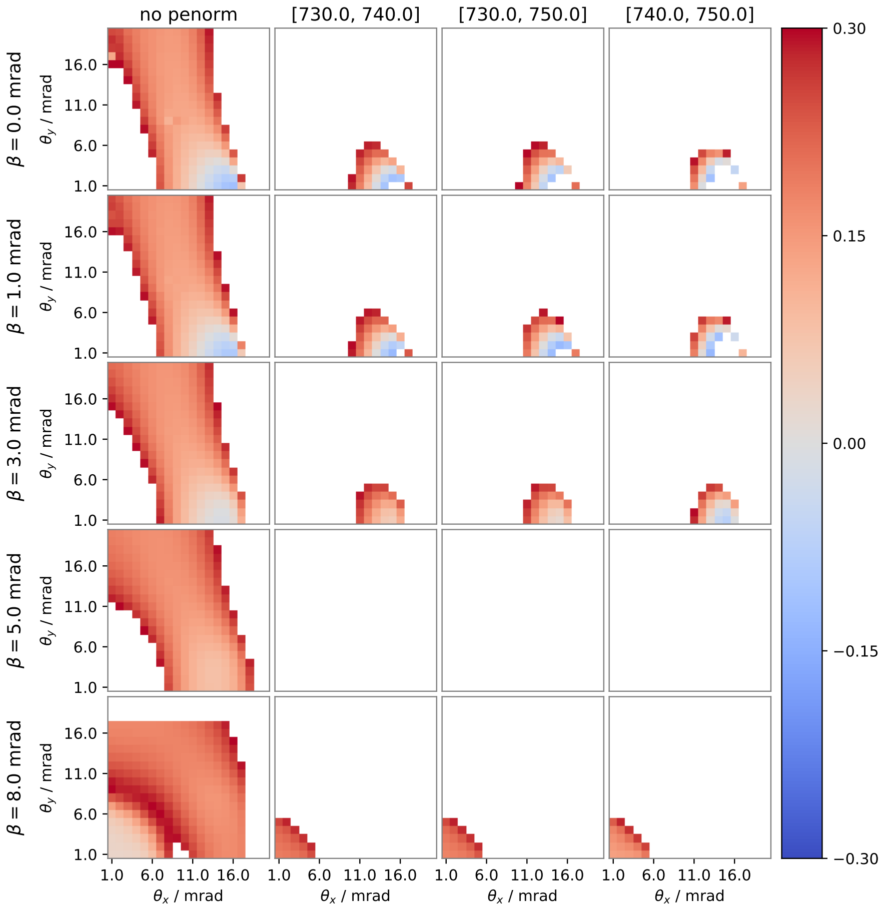

Figure 5.14: m_L/m_S-map calculated from the eEMCD-signal in lamb3-approximation at thickness 15 nm and extracted by the double difference method. Refer to the caption of figure 5.8for a detailed description of the technicalities of these maps. The q-averaging range (c.f. equation (4.19)) is equal to the post-edge normalization range except for the column, in which no post-edge normalization is applied and it is set to [730 eV, 740 eV].

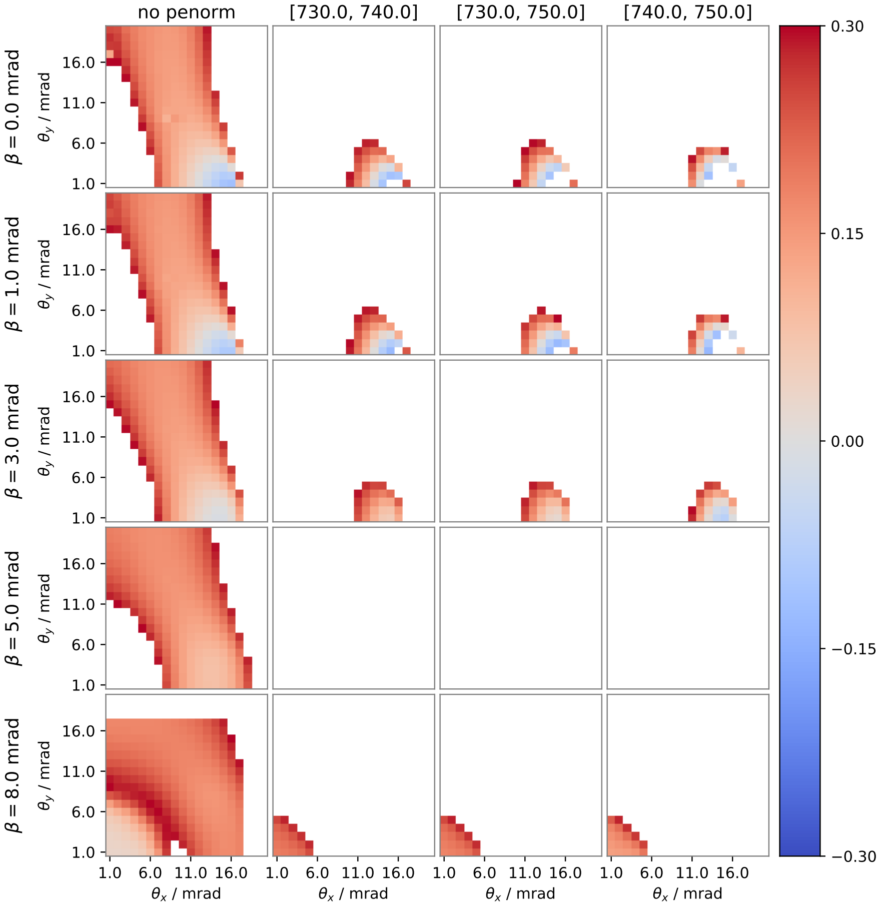

Figure 5.15: m_L/m_S-map calculated from the eEMCD-signal in lamb3-approximation for the same parameters as figure 5.14 except that the q-averaging range (c.f. equation (4.19)) is set to [745 eV, 750 eV]

5.5 APPARENT ANISOTROPY OF THE REAL PART OF THE MDFF

This section is dedicated to a more detailed analysis of what is named an *apparent anisotropy* in section 5.2. This term is chosen here since the contribution of the real part of the MDFF is generally believed to be somewhat isotropic. It would thus cancel out in equation (2.37) or contribute weakly in comparison with the imaginary part. The large difference between the pEMCD- and eEMCD-signal seen in section 5.2 and plotted in figure 5.16 suggest that this is not necessarily the case.

The energy-integrated DDSCS due to the real part of the MDFF,

$$\Delta\sigma^{\epsilon}_{\mathrm{dd,re}} = \int \mathrm{d}E\,\Delta\sigma^{\epsilon}_{\mathrm{dd}}(E) - \int \mathrm{d}E\,\Delta\sigma_{\mathrm{dd,im}}(E) \tag{5.1}$$

shows a strong contribution around the center of the diffraction pattern at both edges $\epsilon \in \{L_2, L_3\}$ in figure 5.16. The relative sign of this contribution in the four quadrants of the map is similar for both edges. The eEMCD-signal is thus enhanced at the L_3-edge with respect to the pEMCD-signal. At the L_2-edge, however, the differing relative sign of the pEMCD-signal and $\Delta\sigma_{\mathrm{dd,re}}$ reduces the strength of the eEMCD-signal.

The edge-resolved relative strength $\Delta\sigma^{j}_{\mathrm{dd,re}}/\Delta\sigma^{j}_{\mathrm{dd,im}}$ of the contribution $\Delta\sigma^{j}_{\mathrm{dd,re}}$ to the eEMCD-signal is displayed in figure 5.17 at thickness 15 nm for different approximation levels of the MDFF. The maps show that the relative strength ranges from −2.0 to 2.0 throughout the diffraction plane at both edges: at the center of the maps, where the direct beam is located, the real part contribution dominates the contribution of the imaginary part. Moving out of the center the absolute value of the relative strength of real and imaginary part contributions decreases to around 0.5 to 1.0, depending on the edge. A broad oval region of smaller relative strength forms around the center of the map. The imaginary part contributions are in this region of comparable magnitude to the contributions of the real part. The oval region extends furthermore in x-direction to the position of the $+\mathbf{G}$- and $-\mathbf{G}$-reflections in the DP. In y-direction its extent is larger and goes beyond the range of calculated scattering angles.

At the L_3-edge these maps of the relative strength $\Delta\sigma^{j}_{\mathrm{dd,re}}/\Delta\sigma^{j}_{\mathrm{dd,im}}$ of $\Delta\sigma^{j}_{\mathrm{dd,re}}$ show lower relative strengths in the mentioned oval region compared to the L_2-edge. Furthermore these maps show at the L_3-edge, that a narrow band of very low relative strength forms at the boundary of regions of large and lower relative strength at all approximation levels. The eEMCD-signal is dominated by the imaginary part contributions at these positions and the magnetic signal contained in the imaginary part is thus expected to be less disturbed by contributions from the real part.

A similarly shaped region of lower relative strength is found at the L_2-edge. In comparison with the L_3-edge the relative strength has, however, a larger magnitude throughout the whole region. The eEMCD-signal is thus more strongly influenced by the real part contribution at the L_2-edge than it is at the L_3-edge. This might therefore be another part required to understand

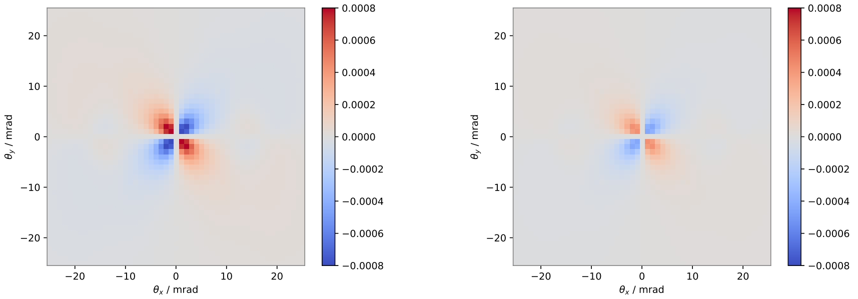

(a) dipole-approximation @ L_3-edge (b) dipole-approximation @ L_2-edge

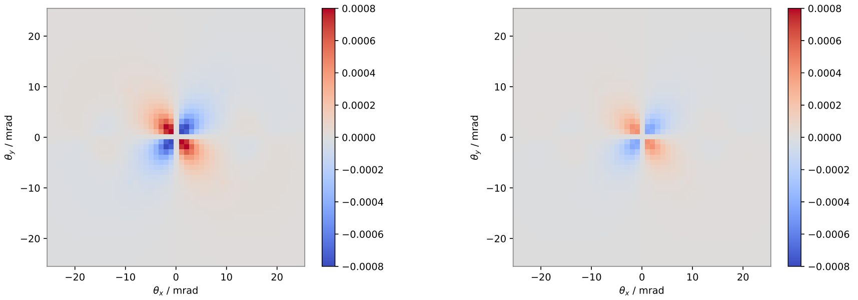

(c) 11-diagonal term @ L_3-edge (d) 11-diagonal term @ L_2-edge

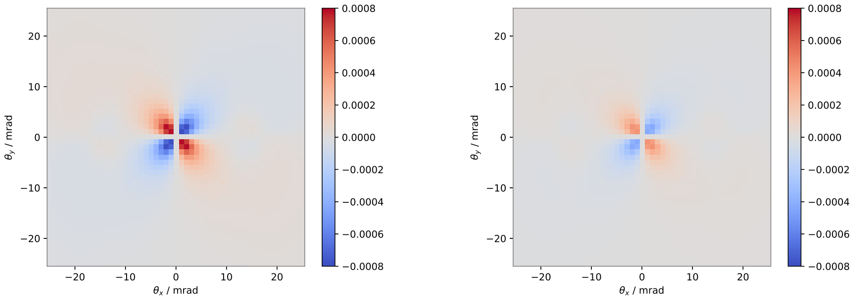

(e) lamb3-approximation @ L_3-edge (f) lamb3-approximation @ L_2-edge

Figure 5.16: Maps showing the contribution to the eEMCD-signal, which is attributable to the real part of the MDFF, i.e., maps showing the difference between the maps shown in figure 5.5 and 5.4 the pEMCD-signal for the following approximations to the MDFF: dipole approximation, computed from the 11-term, and in lamb3-approximation at the L_3- and L_2-edge at thicknesses 15 nm.

the origin of the often weak signal at the L_2-edge in experiments (c.f. section 5.1 and 5.3).

It is furthermore found that the shape of the region of lower relative strength $\Delta\sigma^{j}_{\mathrm{dd,re}}/\Delta\sigma^{j}_{\mathrm{dd,im}}$ of $\Delta\sigma^{j}_{\mathrm{dd,re}}$ correlates to some extent with the shape of the region of a lower m_L/m_S-ratio in figures 5.12, 5.12, 5.12 and 5.15. This observation suggests that the m_L/m_S-ratio is sensitive to the relative magnitudes of real and imaginary part contributions.

Considering figures A.46 and A.47 it is found that the edge-resolved relative strength $\Delta\sigma^{L_j}_{\mathrm{dd,re}}/\Delta\sigma^{L_j}_{\mathrm{dd,im}}$ is strongly thickness-dependent. At a thickness of 10 nm the region of low relative strength $\Delta\sigma^{j}_{\mathrm{dd,re}}/\Delta\sigma^{j}_{\mathrm{dd,im}}$ is broad and extends to the edges of the calculated region of scattering angles. In the corners of these maps, however, that eEMCD-signal is dominated by the real part contributions.

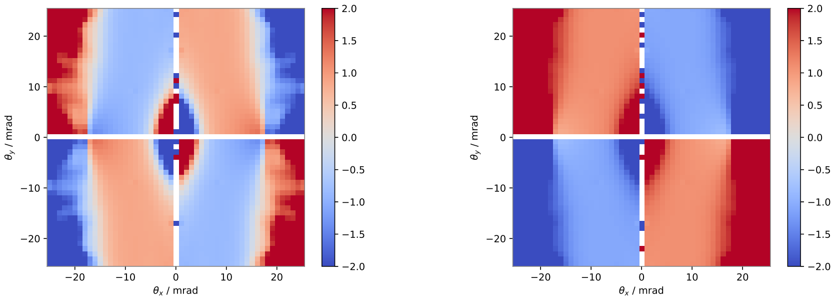

(a) dipole-approximation @ L_3-edge

(b) dipole-approximation @ L_2-edge

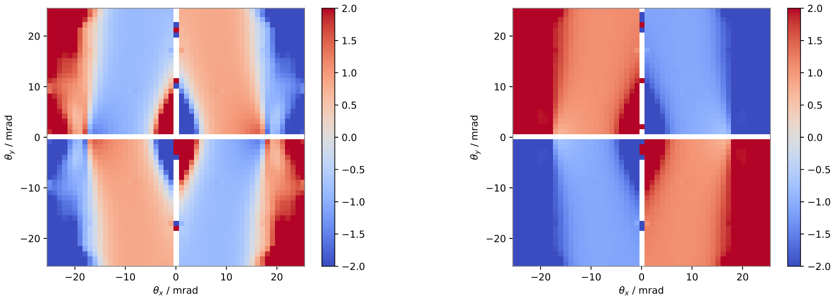

(c) 11-diagonal term @ L_3-edge

(d) 11-diagonal term @ L_2-edge

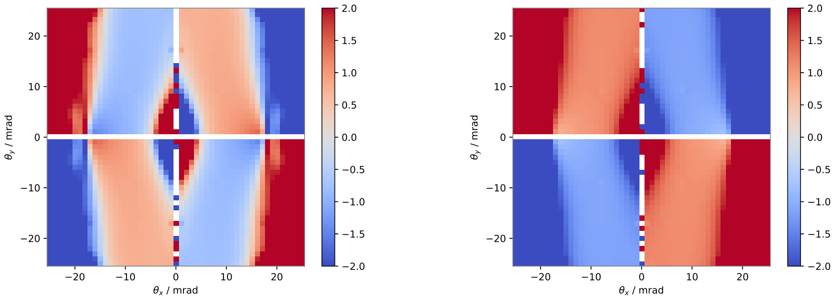

(e) lamb3-approximation @ L_3-edge

(f) lamb3-approximation @ L_2-edge

Figure 5.17: Edge-resolved maps of the relative strength of the contribution due to the real part of the MDFF to the energy-integrated eEMCD-signal $\Delta\sigma^{L_j}_{\mathrm{dd,re}}/\Delta\sigma^{L_j}_{\mathrm{dd,im}}$ for selected approximation levels of the MDFF at thicknesses 15 nm.

6

CONCLUSION

ELNES-spectra of the L_3 and L_2-edge of bcc-iron are simulated in this work in order to study the influence of non-dipole terms on the EMCD-signal, which can be extracted from these spectra. This work distinguishes between the pEMCD-signal and the eEMCD-signal. Both signals were initially anticipated to be comparable in magnitude but a somewhat large difference between both is found in the performed simulation. This apparent anisotropy has not been reported in the literature and its cause remains unclear in the present work.

A conclusive quantitative answer to the initially posed problem of the influence of non-dipole terms on the extraction of EMCD remains to be found in the case of the eEMCD-signal because of the not anticipated influence of the post-edge normalization range and the apparent anisotropy in this work. Both effects have a much stronger influence on the eEMCD-signal than non-dipole terms have md any further research needs to address both effects properly before proceeding with the investigation of non-dipole effects. However, the 13-term can already be singled out for further investigation based on its found contributions to the eEMCD-signal.

The pEMCD-signals on the other hand do not show a strong effect attributable to non-dipole terms. Only small differences in the m_L/m_S-ratio are found at large scattering angles, which are weakened by practicable detector sizes. The pEMCD-signal remains, however, a quantity that is only accessible in theoretical treatments and any simulation trying to get closer to the experimental results needs to be based upon the eEMCD-signal.

As a byproduct of these investigations some deeper insight into one of the reasons why the double difference method is superior to the other extraction methods has been found. The double difference method reduces the effect of the 01- and 12-terms on the eEMCD-signal.

The calculated eEMCD-signals show in parts a lowering or suppression of the eEMCD-signal at the L_2-edge and two contributing effects are identified as the apparent anisotropy of the real part of the MDFF and the contribution due to the 13-term at large scattering angles. These effects might provide an explanation for the weak EMCD-signal often observed experimentally at the L_2-edge in the future if it is investigated further.

In conclusion this Master thesis is a progress report on the road towards a deeper understanding of the effect of non-dipole terms on the extraction of EMCD and it opened up unanticipated questions regarding a proper theoretical description of the post-edge region and the physical origin of the apparent anisotropy.

REFERENCES

[1] C. Hébert and P. Schattschneider. "A proposal for dichroic experiments in the electron microscope." In: *Ultramicroscopy* 96.3 (2003). Proceedings of the International Workshop on Strategies and Advances in Atomic Level Spectroscopy and Analysis, pp. 463–468. ISSN: 0304-3991. DOI: 10.1016/S0304-3991(03)00108-6.

[2] P. Schattschneider et al. "Detection of magnetic circular dichroism using a transmission electron microscope." In: *Nature* 441 (2006), pp. 486–488. DOI: 10.1038/nature04778.

[3] P. Schattschneider et al. "Detection of magnetic circular dichroism on the two-nanometer scale." In: *Phys. Rev. B* 78 (10 2008), p. 104413. DOI: 10.1103/PhysRevB.78.104413.

[4] P. Schattschneider et al. "Magnetic circular dichroism in EELS: Towards 10nm resolution." In: *Ultramicroscopy* 108.5 (2008), pp. 433–438. ISSN: 0304-3991. DOI: 10.1016/j.ultramic.2007.07.002.

[5] H. Lidbaum et al. "Quantitative Magnetic Information from Reciprocal Space Maps in Transmission Electron Microscopy." In: *Phys. Rev. Lett.* 102 (3 Jan. 2009), p. 037201. DOI: 10.1103/PhysRevLett.102.037201.

[6] H. Lidbaum et al. "Reciprocal and real space maps for EMCD experiments." In: *Ultramicroscopy* 110.11 (2010), pp. 1380–1389. ISSN: 0304-3991. DOI: 10.1016/j.ultramic.2010.07.004.

[7] T. Thersleff et al. "Detection of magnetic circular dichroism with subnanometer convergent electron beams." In: *Phys. Rev. B* 94 (13 Oct. 2016), p. 134430. DOI: 10.1103/PhysRevB.94.134430.

[8] M. Uchida and A. Tonomura. "Generation of electron beams carrying orbital angular momentum." In: *Nature* 464 (2010), p. 737. DOI: 10.1038/nature08904.

[9] J. Verbeeck, H. Tian, and P. Schattschneider. "Production and application of electron vortex beams." In: *Nature* 467 (2010), p. 301. DOI: 10.1038/nature09366.

[10] J. Rusz, S. Rubino, and P. Schattschneider. "First-principles theory of chiral dichroism in electron microscopy applied to $3d$ ferromagnets." In: *Phys. Rev. B* 75 (21 2007), p. 214425. DOI: 10.1103/PhysRevB.75.214425.

[11] D. B. Williams and C. B. Carter. *Transmission Electron Microscopy. Part 1: Basics.* 2nd ed. Springer, 2009. ISBN: 9780387765006.

[12] D. Pohl et al. "Atom size electron vortex beams with selectable orbital angular momentum." In: *Scientific Reports* 7.1 (2017), p. 934. ISSN: 2045-2322. DOI: 10.1038/s41598-017-01077-9.

[13] M. Nord. Ed. by (. ”Magnunor”). June 17, 2017. URL: https://commons.wikimedia.org/wiki/File:Electron_energy_loss_spectrum_feature_overview.svg (visited on 10/14/2018).

[14] R. F. Egerton. “Electron energy-loss spectroscopy in the TEM.” In: *Reports on Progress in Physics* 72.1 (2009), p. 016502.

[15] M. Inokuti. “Inelastic Collisions of Fast Charged Particles with Atoms and Molecules—The Bethe Theory Revisited.” In: *Rev. Mod. Phys.* 43 (3 1971), pp. 297–347. DOI: 10.1103/RevModPhys.43.297.

[16] H. J. Kohl and H. H. Rose. “Theory of Image Formation by Inelastically Scattered Electrons in the Electron Microscope.” In: ed. by P. W. Hawkes. Vol. 65. Advances in Electronics and Electron Physics. Academic Press, 1985, pp. 173–227. DOI: 10.1016/S0065-2539(08)60878-1.

[17] N. W. Ashcroft and N. D. Mermin. *Solid State Physics.* 1976. ISBN: 9780030839931.

[18] E. J. Kirkland. *Advanced Computing in Electron Microscopy.* second Edition. Springer, 2010. ISBN: 978-1-4419-6532-5. DOI: 10.1007/978-1-4419-6533-2.

[19] A. P. Hitchcock. “Near Edge Electron Energy Loss Spectroscopy: Comparison to X-ray Absorption.” In: *Japanese Journal of Applied Physics* 32.S2 (1993), p. 176.

[20] J. Yuan and N. K. Menon. “Magnetic linear dichroism in electron energy loss spectroscopy.” In: *Journal of Applied Physics* 81.8 (1997), p. 5087. DOI: 10.1063/1.364480.

[21] P. Blaha et al. *WIEN2k. An Augmented Plane Wave + Local Orbitals Program for Calculating Crystal Properties.* Ed. by K. Schwarz. Austria: Technische Universität Wien, 2001. ISBN: 3-9501031-1-2.

[22] K. Schwarz and P. Blaha. “Solid state calculations using WIEN2k.” In: *Computational Materials Science* 28.2 (2003). Proceedings of the Symposium on Software Development for Process and Materials Design, pp. 259–273. ISSN: 0927-0256. DOI: 10.1016/S0927-0256(03)00112-5.

[23] K. Schwarz. “DFT calculations of solids with LAPW and WIEN2k.” In: *Journal of Solid State Chemistry* 176.2 (2003). Special issue on The Impact of Theoretical Methods on Solid-State Chemistry, pp. 319–328. ISSN: 0022-4596. DOI: https://doi.org/10.1016/S0022-4596(03)00213-5.

[24] P. Hohenberg and W. Kohn. “Inhomogeneous Electron Gas.” In: *Phys. Rev.* 136 (3B Sept. 1964), B864–B871. DOI: 10.1103/PhysRev.136.B864.

[25] W. Kohn and L. J. Sham. “Self-Consistent Equations Including Exchange and Correlation Effects.” In: *Phys. Rev.* 140 (4A Sept. 1965), A1133–A1138. DOI: 10.1103/PhysRev.140.A1133.

[26] S. Cottenier. *Density Functional Theory and the family of (L)APW-methods: a step-by-step introduction.* 2013. URL: http://www.wien2k.at/reg_user/textbooks.

[27] P. Novák. *Calculation of spin-orbit coupling.* 1997. URL: http://susi.theochem.tuwien.ac.at/reg_user/textbooks/novak_lecture_on_spinorbit.pdf.

[28] F. Cardarelli. *Materials Handbook. A Concise Desktop Reference.* 2nd ed. London: Springer, 2008. ISBN: 978-1-84628-669-8.

[29] J. P. Perdew, K. Burke, and M. Ernzerhof. "Generalized Gradient Approximation Made Simple." In: *Phys. Rev. Lett.* 77 (18 Oct. 1996), pp. 3865–3868. DOI: 10.1103/PhysRevLett.77.3865.

[30] J. Rusz, S. Muto, and K. Tatsumi. "New algorithm for efficient Bloch-waves calculations of orientation-sensitive ELNES." In: *Ultramicroscopy* 125 (2013), pp. 81–88. ISSN: 0304-3991. DOI: 10.1016/j.ultramic.2012.09.009.

[31] P. Rez et al. "Review of methods for calculating near edge structure." In: *Ultramicroscopy* 59.1 (1995). Proceedings of the 2nd international workshop on Electron Energy Loss Spectroscopy and Imaging, pp. 159–167. ISSN: 0304-3991. DOI: 10.1016/0304-3991(95)00025-V.

[32] C. Hébert, J. Luitz, and P. Schattschneider. "Improvement of energy loss near edge structure calculation using Wien2k." In: *Micron* 34.3 (2003). Zeitler Festschrift, pp. 219–225. ISSN: 0968-4328. DOI: 10.1016/S0968-4328(03)00030-1.

[33] P. Zeiger. *temtools. Software to analyse TEM simulations and diffraction patterns.* https://gitlab.com/pzeiger/temtools. 2018.

[34] C. Hébert. "Practical aspects of running the WIEN2k code for electron spectroscopy." In: *Micron* 38.1 (2007), pp. 12–28. ISSN: 0968-4328. DOI: 10.1016/j.micron.2006.03.010.

[35] J. Rusz et al. "Sum rules for electron energy loss near edge spectra." In: *Phys. Rev. B* 76 (6 Aug. 2007), p. 060408. DOI: 10.1103/PhysRevB.76.060408.

[36] L. Calmels et al. "Experimental application of sum rules for electron energy loss magnetic chiral dichroism." In: *Phys. Rev. B* 76 (6 Aug. 2007), p. 060409. DOI: 10.1103/PhysRevB.76.060409.

[37] B. Loukya et al. "Electron magnetic chiral dichroism in CrO2 thin films using monochromatic probe illumination in a transmission electron microscope." In: *Journal of Magnetism and Magnetic Materials* 324.22 (2012), pp. 3754–3761. ISSN: 0304-8853. DOI: 10.1016/j.jmmm.2012.06.012.

[38] P. Schattschneider. *Linear and Chiral Dichroism in the Electron Microscope.* 1st ed. Pan Stanford Publishing, 2012. ISBN: 9789814267489.

[39] S. Muto, K. Tatsumi, and J. Rusz. “Parameter-free extraction of EMCD from an energy-filtered diffraction datacube using multivariate curve resolution.” In: *Ultramicroscopy* 125 (2013), pp. 89–96. ISSN: 0304-3991. DOI: `10.1016/j.ultramic.2012.09.008`.

APPENDIX

This appendix contains additional figures, which were calculated for this work but did not make it into the main text. Section A.1 contains more maps of the energy-integrated EMCD-signal for thicknesses of 10 nm and 20 nm. Section A.2 contains similarly additional maps of the m_L/m_S-ratio and section A.3 additional maps showing the apparent anisotropy.

A.1 ADDITIONAL MAPS OF THE ENERGY-INTEGRATED EMCD-SIGNAL

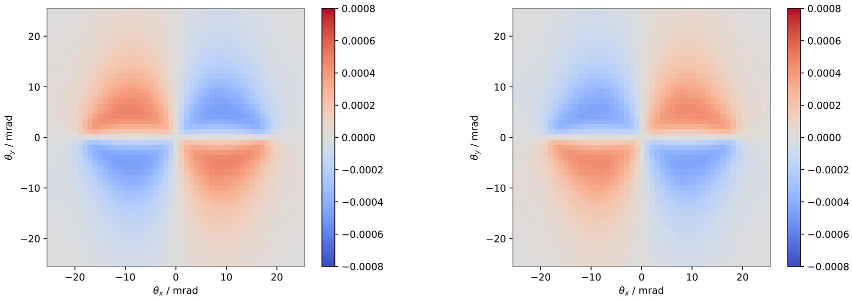

(a) dipole-approximation @ L_3-edge (b) dipole-approximation @ L_2-edge

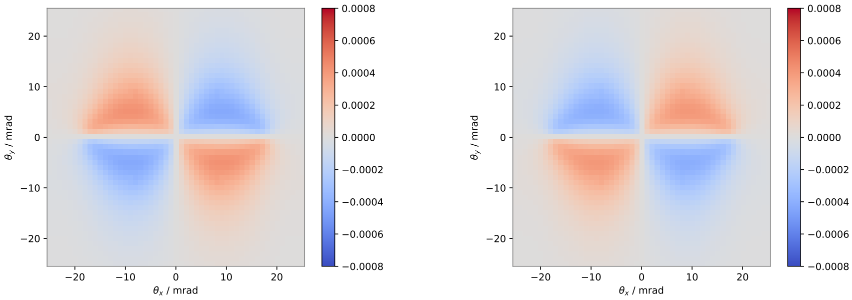

(c) 11-diagonal term @ L_3-edge (d) 11-diagonal term @ L_2-edge

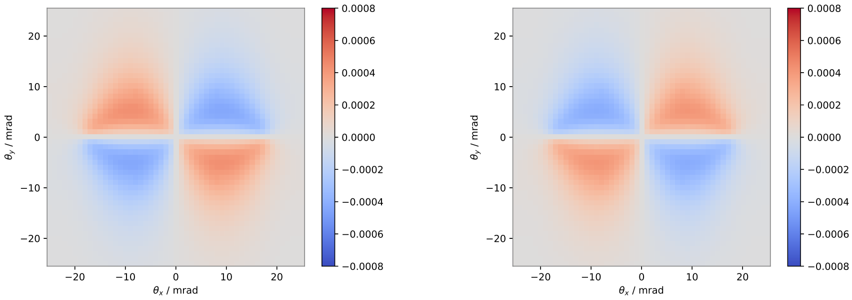

(e) lamb3 approximation @ L_3-edge (f) lamb3-approximation @ L_2-edge

Figure A.1: Edge-resolved comparison of maps of the unbroadened energy-integrated pEMCD-signal computed using different approximation levels of the MDFF as indicated in the captions of the subfigures. All maps are calculated using the double difference method at thickness 10 nm.

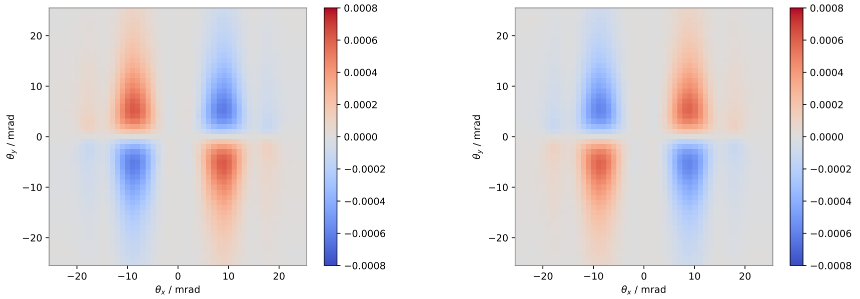

(a) dipole-approximation @ L_3-edge (b) dipole-approximation @ L_2-edge

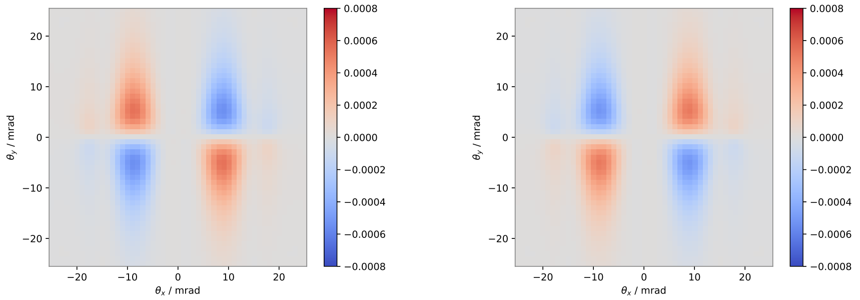

(c) 11-diagonal term @ L_3-edge (d) 11-diagonal term @ L_2-edge

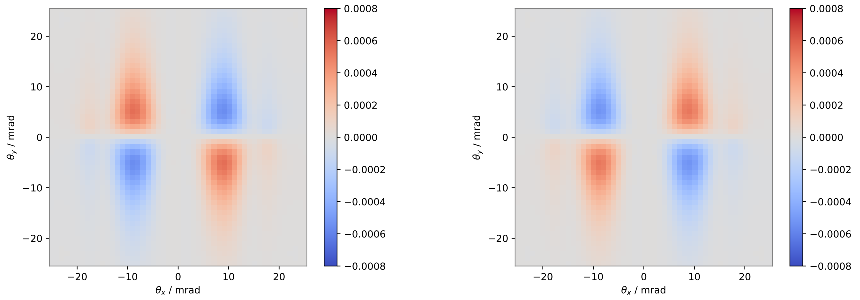

(e) lamb3-approximation @ L_3-edge (f) lamb3-approximation @ L_2-edge

Figure A.2: Edge-resolved comparison of maps of the unbroadened energy-integrated pEMCD-signal computed using different approximation levels of the MDFF as indicated in the captions of the subfigures. All maps are calculated using the double difference method at thickness 20 nm.

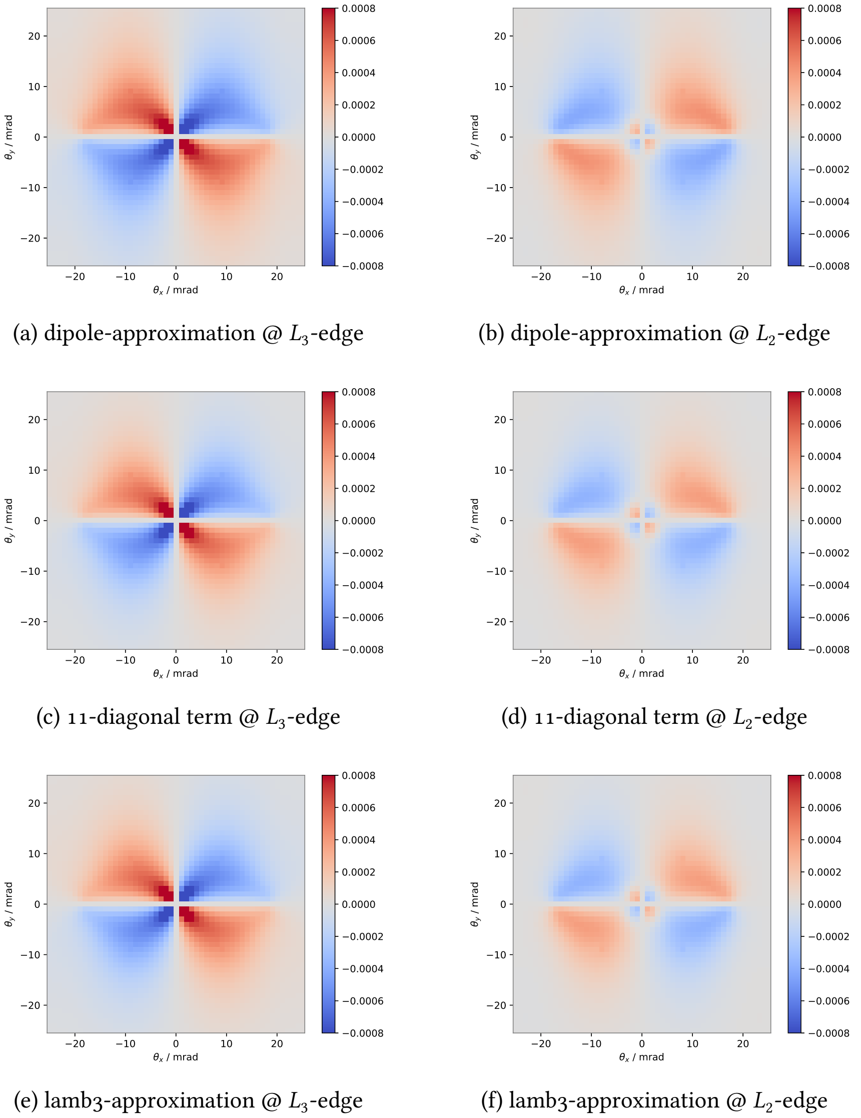

(a) dipole-approximation @ L_3-edge (b) dipole-approximation @ L_2-edge

(c) 11-diagonal term @ L_3-edge (d) 11-diagonal term @ L_2-edge

(e) lamb3-approximation @ L_3-edge (f) lamb3-approximation @ L_2-edge

Figure A.3: Comparison of maps of the eEMCD-signal in dipole approximation, computed from the 11-term, and in lamb3-approximation at the L_3- and L_2-edge at thicknesses 10 nm.

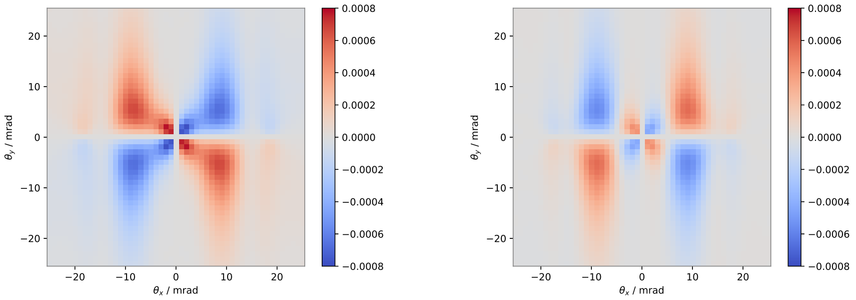

(a) dipole-approximation @ L_3-edge (b) dipole-approximation @ L_2-edge

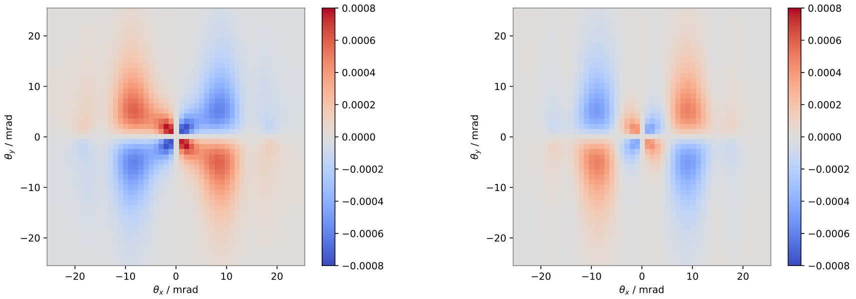

(c) 11-diagonal term @ L_3-edge (d) 11-diagonal term @ L_2-edge

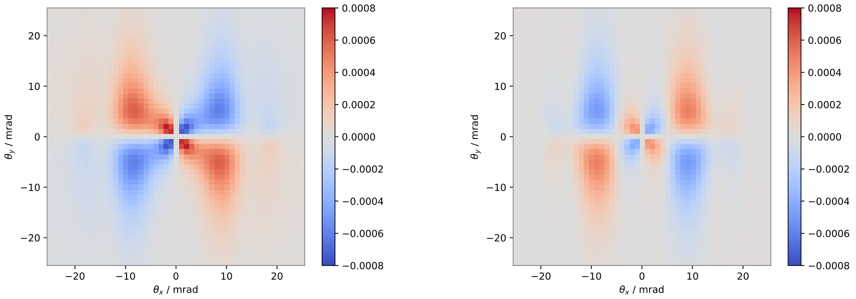

(e) lamb3-approximation @ L_3-edge (f) lamb3-approximation @ L_2-edge

Figure A.4: Comparison of maps of the eEMCD-signal in dipole approximation, computed from the 11-term, and in lamb3-approximation at the L_3- and L_2-edge at thicknesses 20 nm.

A.2 ADDITIONAL m_L/m_S-MAPS

For reference purposes this section of the appendix lists some additional maps of the m_L/m_S-ratio. Subsection A.2.1 lists additional maps for the pEMCD-signal and subsection A.2.1 for the eEMCD-signal.

A.2.1 *pEMCD*

Maps of the m_L/m_S-ratio for the double difference methods are depicted in the figures in A.2.1.1. Refer to sections 4 and 5.4 for more information on the calculation procedure.

A.2.1.1 *Double difference method*

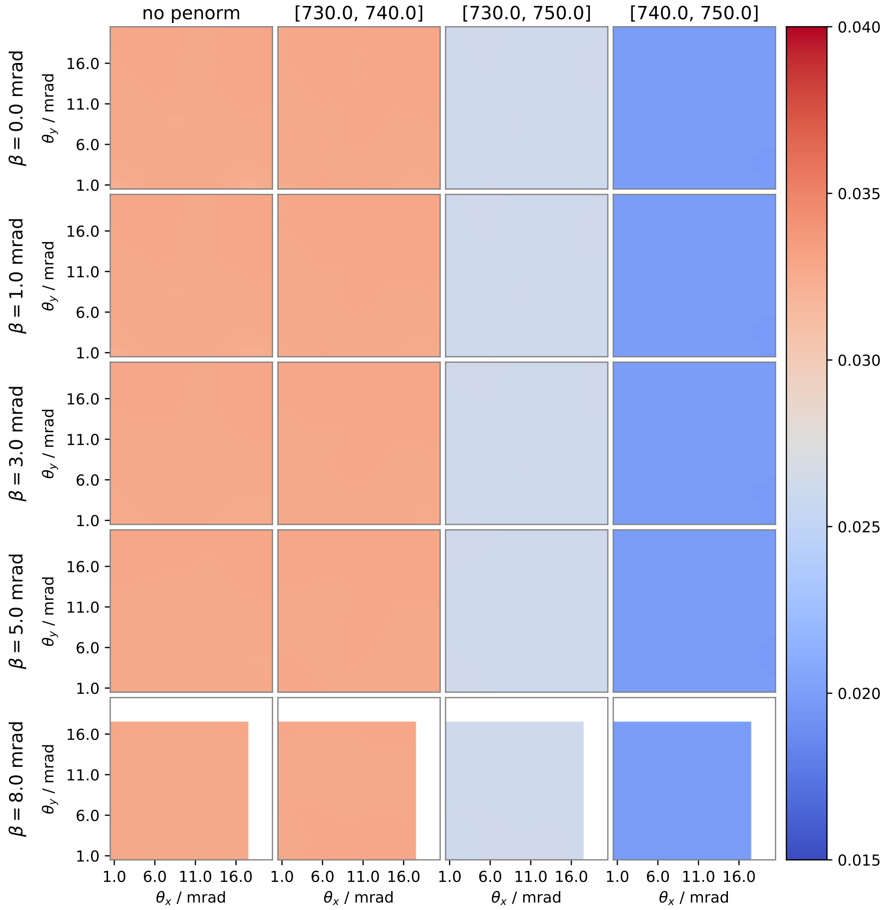

Figure A.5: m_L/m_S-maps comparing the effects of detector size and post-edge normalization range. Maps are computed from the pEMCD-signal in dipole approximation at thickness 10 nm using the double difference method. The averaging range for determination of q is equal to the post-edge normalization range.

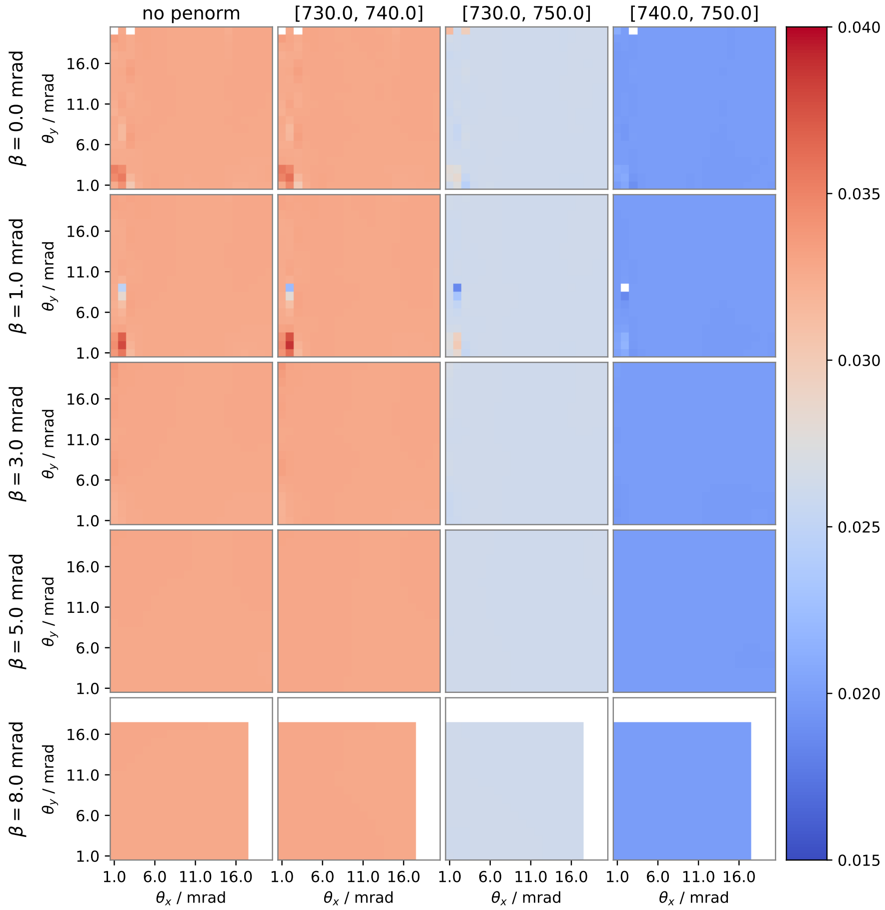

Figure A.6: m_L/m_S-maps comparing the effects of detector size and post-edge normalization range. Maps are computed from the pEMCD-signal in dipole approximation at thickness 20 nm using the double difference method. The averaging range for determination of q is equal to the post-edge normalization range.

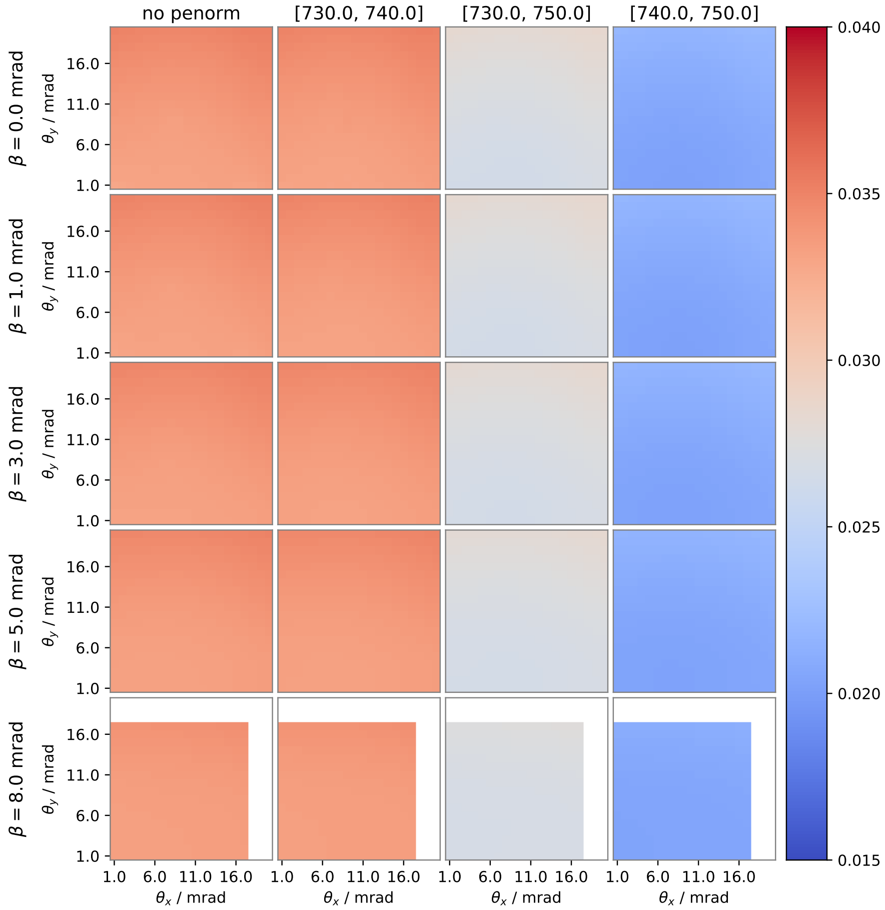

Figure A.7: m_L/m_S-maps comparing the effects of detector size and post-edge normalization range. Maps are computed from the pEMCD-signal for the 11-term at thickness 10 nm using the double difference method. The averaging range for determination of q is equal to the post-edge normalization range.

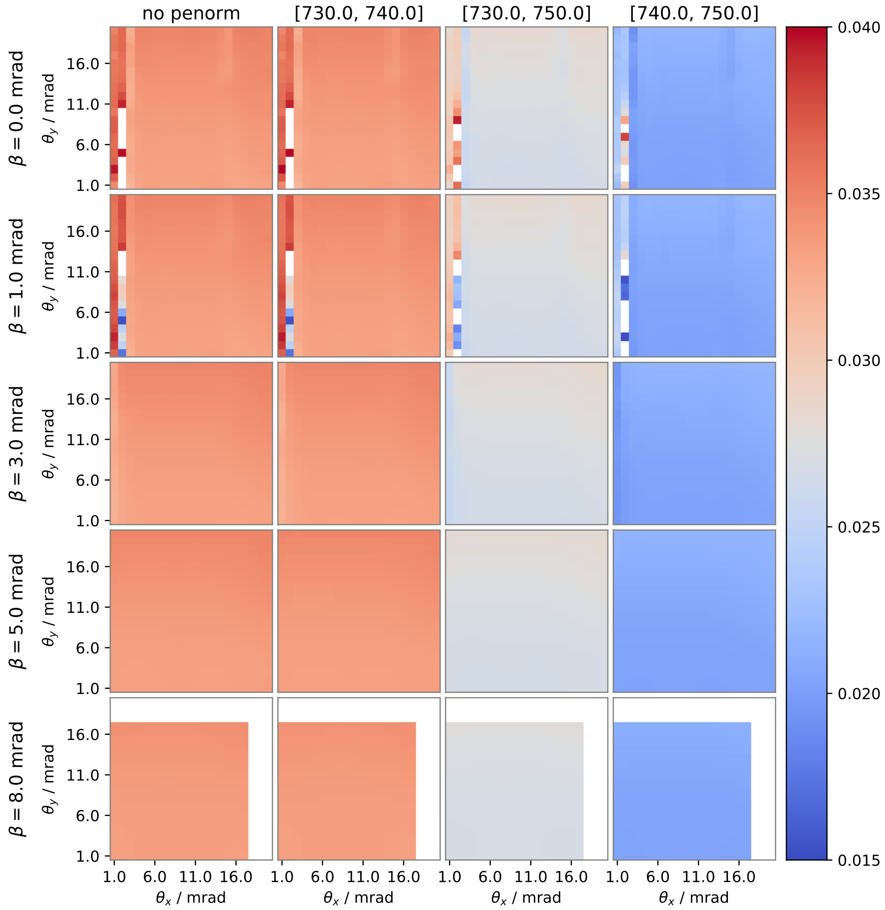

Figure A.8: m_L/m_S-maps comparing the effects of detector size and post-edge normalization range. Maps are computed from the pEMCD-signal for Rayleigh expansion up to third order at thickness 20 nm using the double difference method. The averaging range for determination of q is equal to the post-edge normalization range.

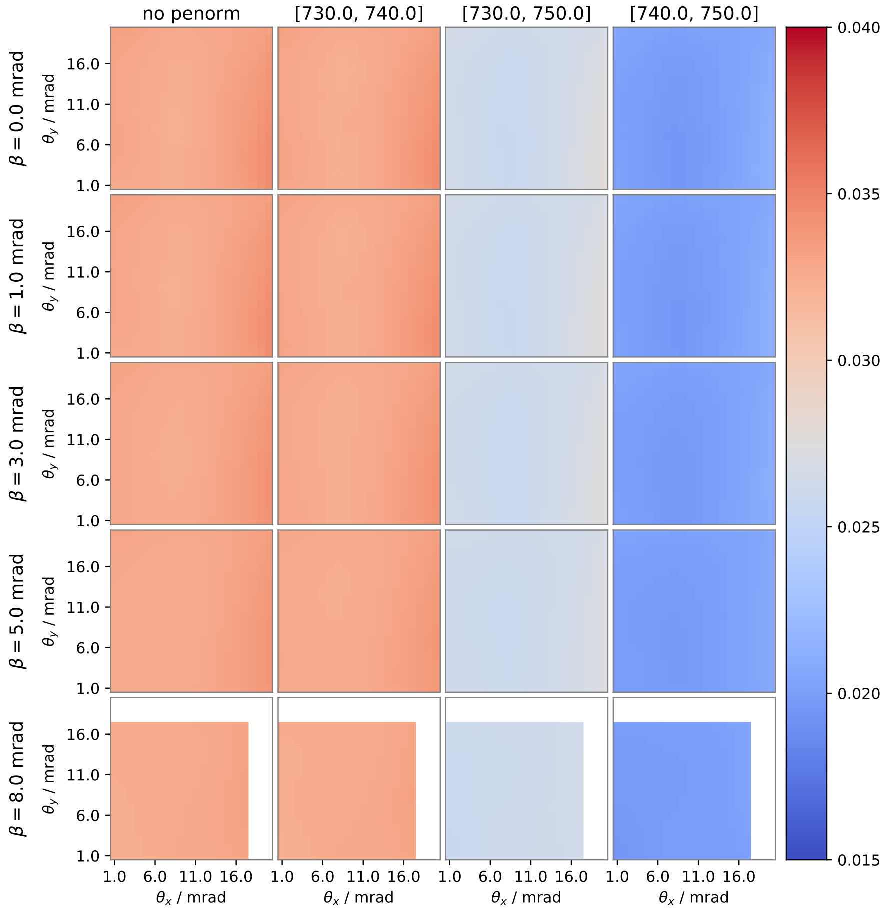

Figure A.9: m_L/m_S-maps comparing the effects of detector size and post-edge normalization range. Maps are computed from the pEMCD-signal for Rayleigh expansion up to third order at thickness 10 nm using the double difference method. The averaging range for determination of q is equal to the post-edge normalization range.

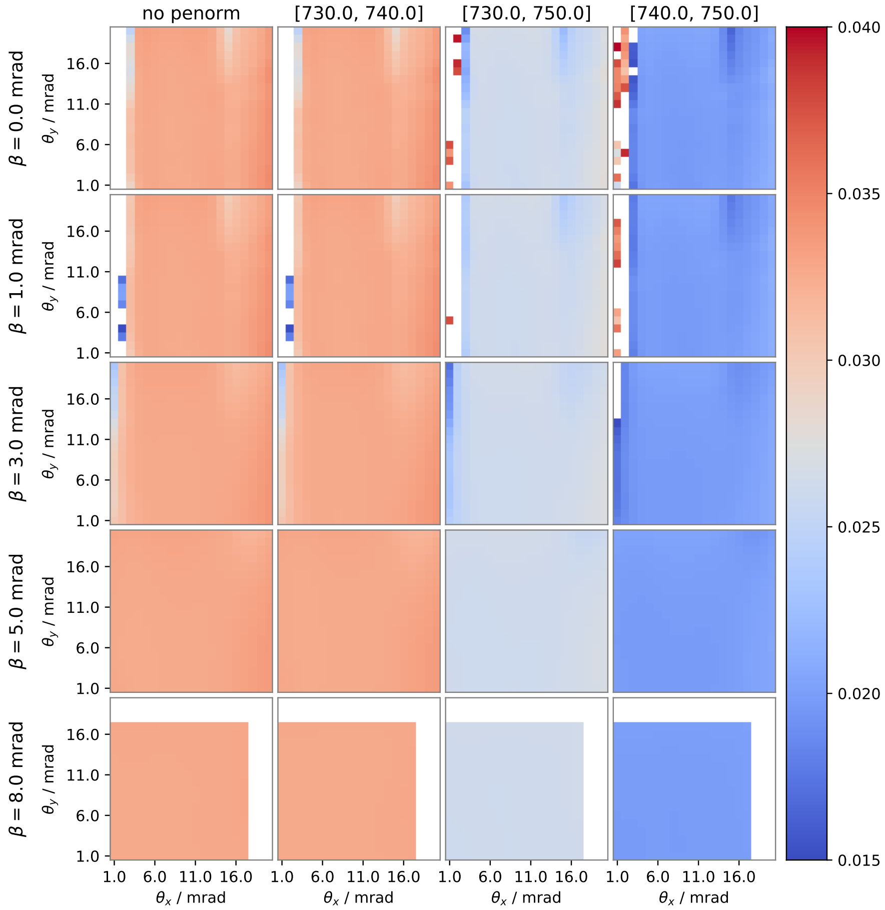

Figure A.10: m_L/m_S-maps comparing the effects of detector size and post-edge normalization range. Maps are computed from the pEMCD-signal for Rayleigh expansion up to third order at thickness 20 nm using the double difference method. The averaging range for determination of q in is equal to the post-edge normalization range.

A.2.1.2 *m_L/m_S-averaging range for q:* 745 eV *to* 750 eV

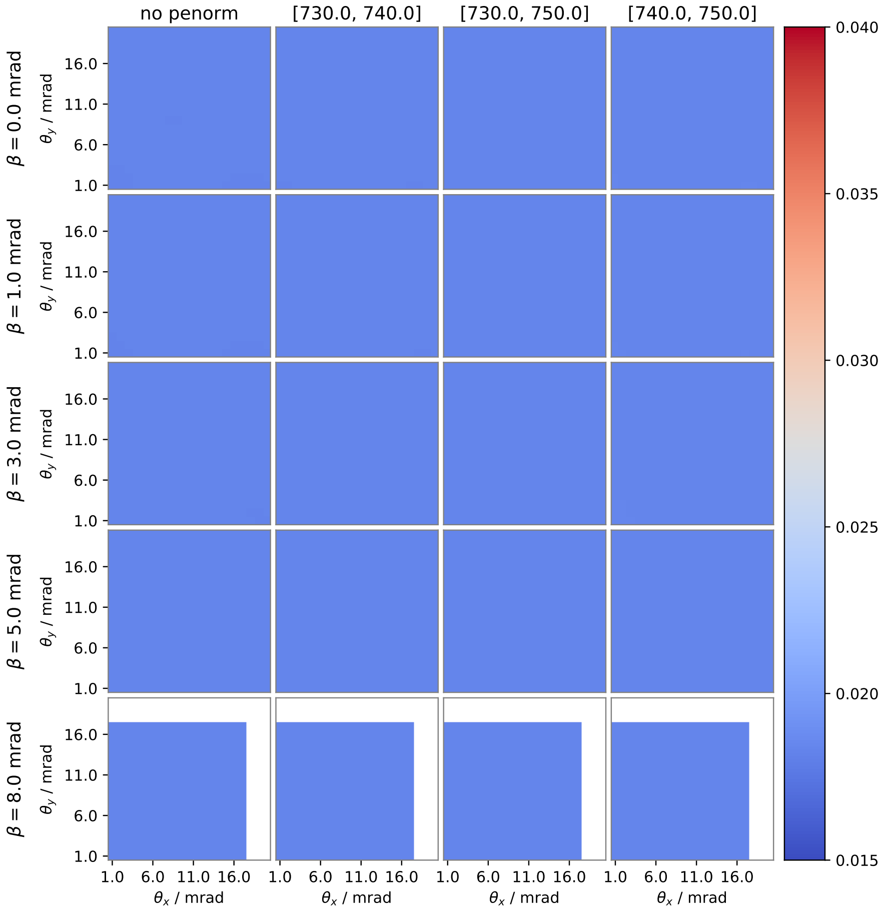

Figure A.11: m_L/m_S-maps comparing the effects of detector size and post-edge normalization range. Maps are computed in dipole approximation at thickness 10 nm using the double difference method from the pEMCD-signal. The averaging range for determination of q is [745 eV, 750 eV].

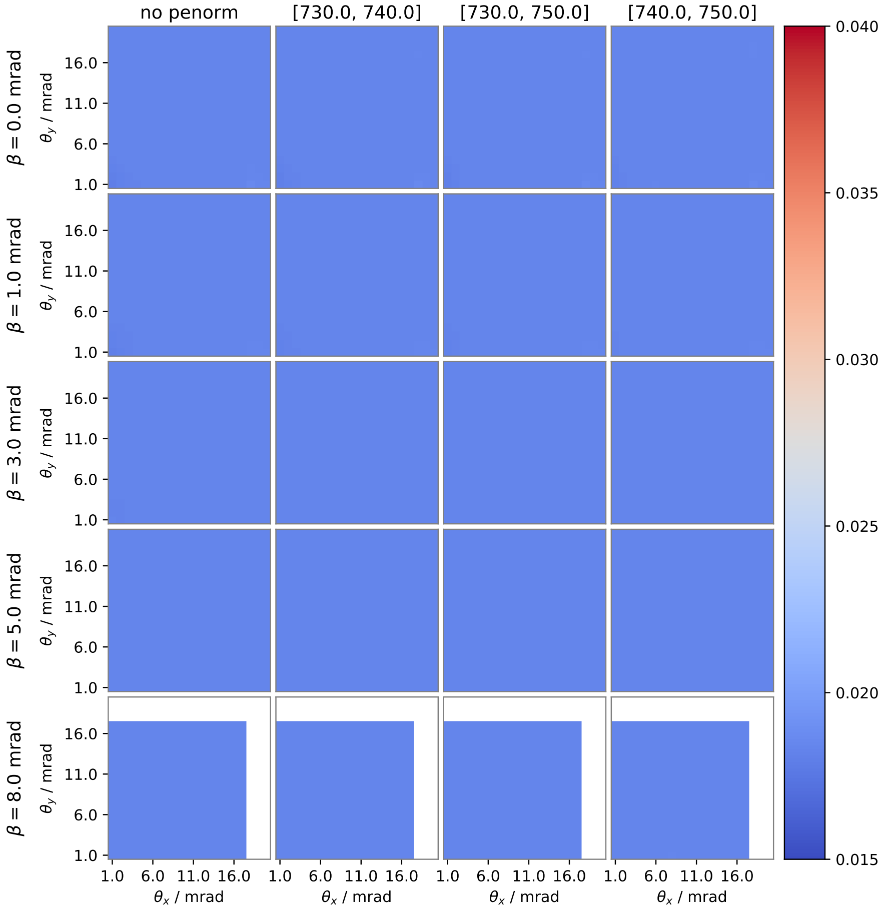

Figure A.12: m_L/m_S-maps comparing the effects of detector size and post-edge normalization range. Maps are computed in dipole approximation at thickness 15 nm using the double difference method from the pEMCD-signal. The averaging range for determination of q is [745 eV, 750 eV].

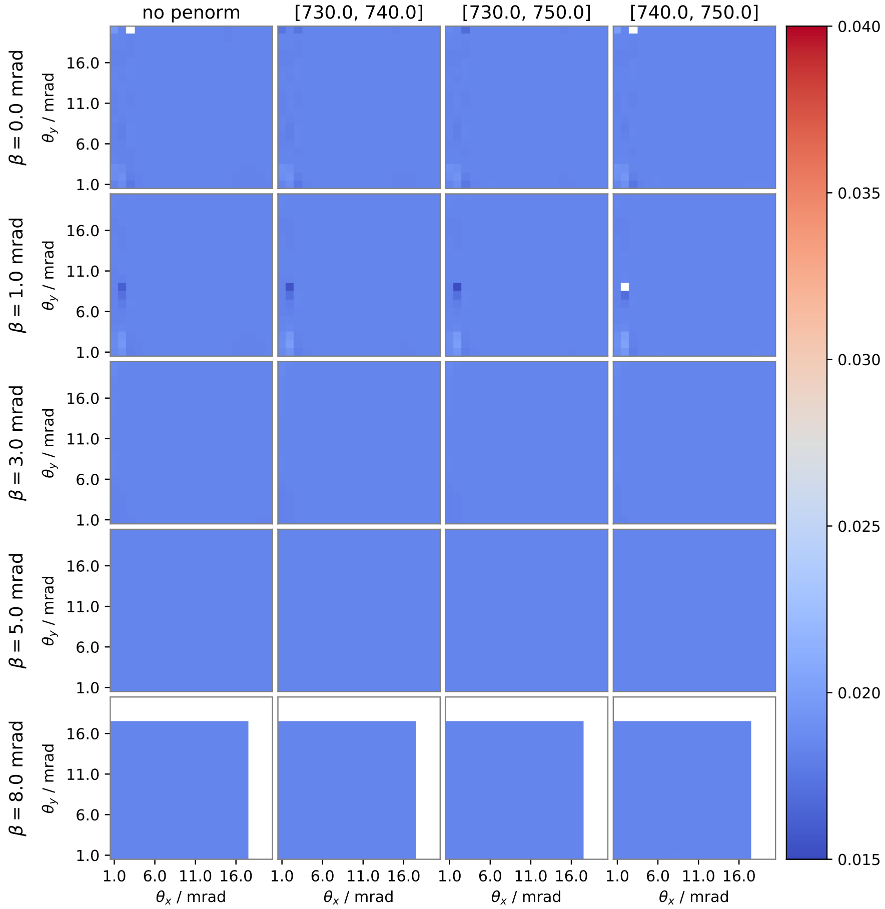

Figure A.13: m_L/m_S-maps comparing the effects of detector size and post-edge normalization range. Maps are computed from the pEMCD-signal in dipole approximation at thickness 20 nm using the double difference method. The averaging range for determination of q is [745 eV, 750 eV].

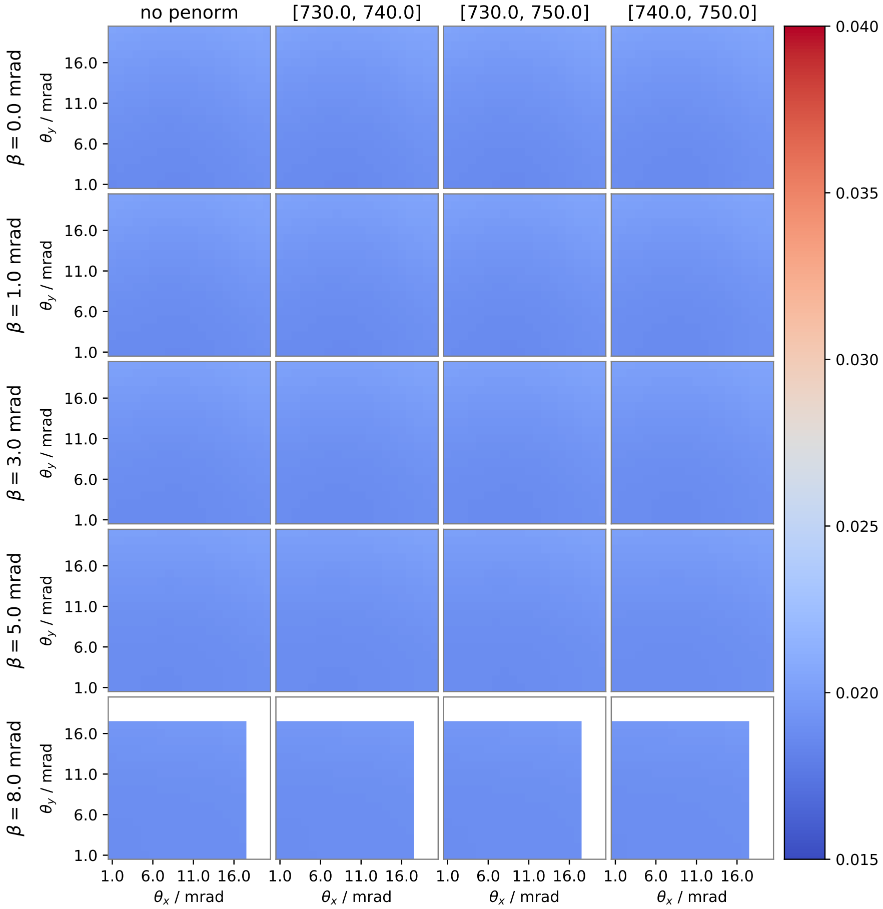

Figure A.14: m_L/m_S-maps comparing the effects of detector size and post-edge normalization range. Maps are computed from the pEMCD-signal of the $\lambda = \lambda' = 1$-term at thickness 10 nm using the double difference method. The averaging range for determination of q is [745 eV, 750 eV].

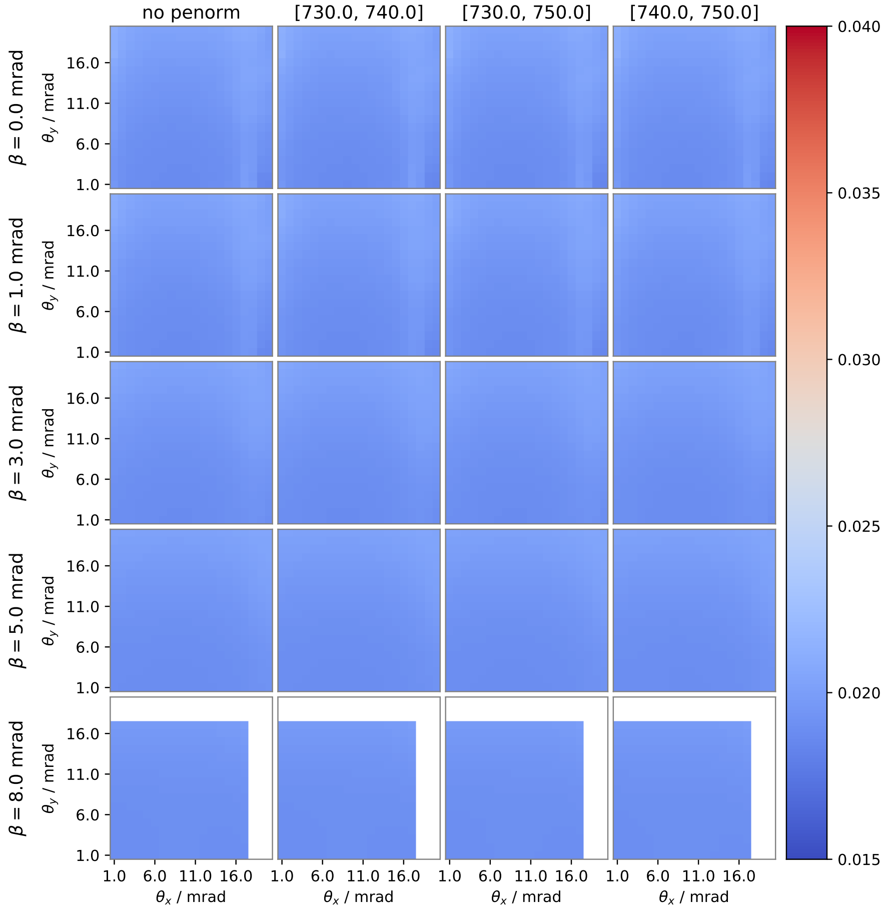

Figure A.15: m_L/m_S-maps comparing the effects of detector size and post-edge normalization range. Maps are computed from the pEMCD-signal of the $\lambda = \lambda' = 1$-term at thickness 15 nm using the double difference method. The averaging range for determination of q is [745 eV, 750 eV].

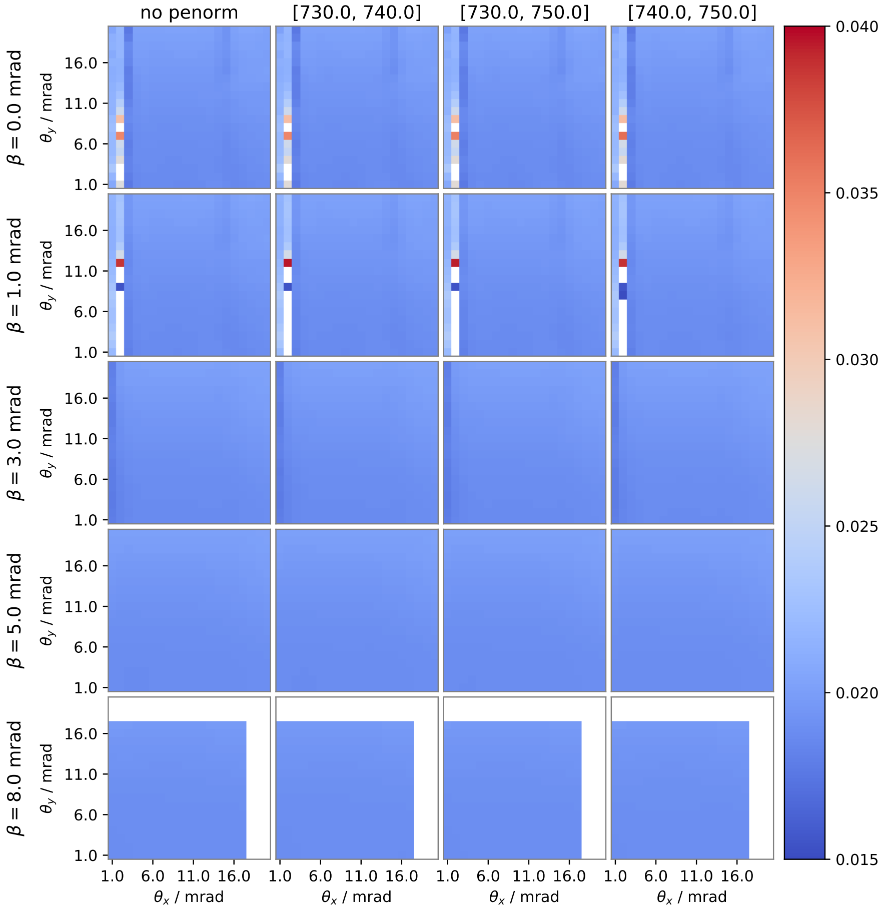

Figure A.16: m_L/m_S-maps comparing the effects of detector size and post-edge normalization range. Maps are computed from the pEMCD-signal of the $\lambda = \lambda' = 1$-term at thickness 20 nm using the double difference method. The averaging range for determination of q is [745 eV, 750 eV].

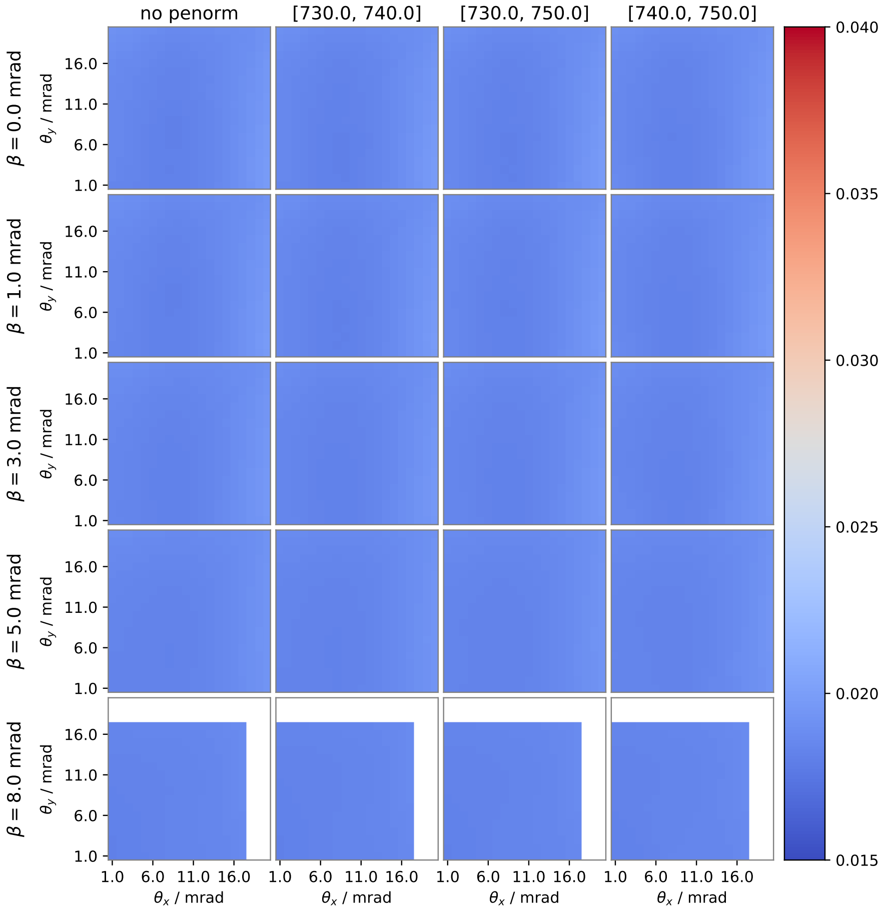

Figure A.17: m_L/m_S-maps comparing the effects of detector size and post-edge normalization range. Maps are computed from the pEMCD-signal for Rayleigh expansion up to third order at thickness 10 nm using the double difference method. The averaging range for determination of q is [745 eV, 750 eV].

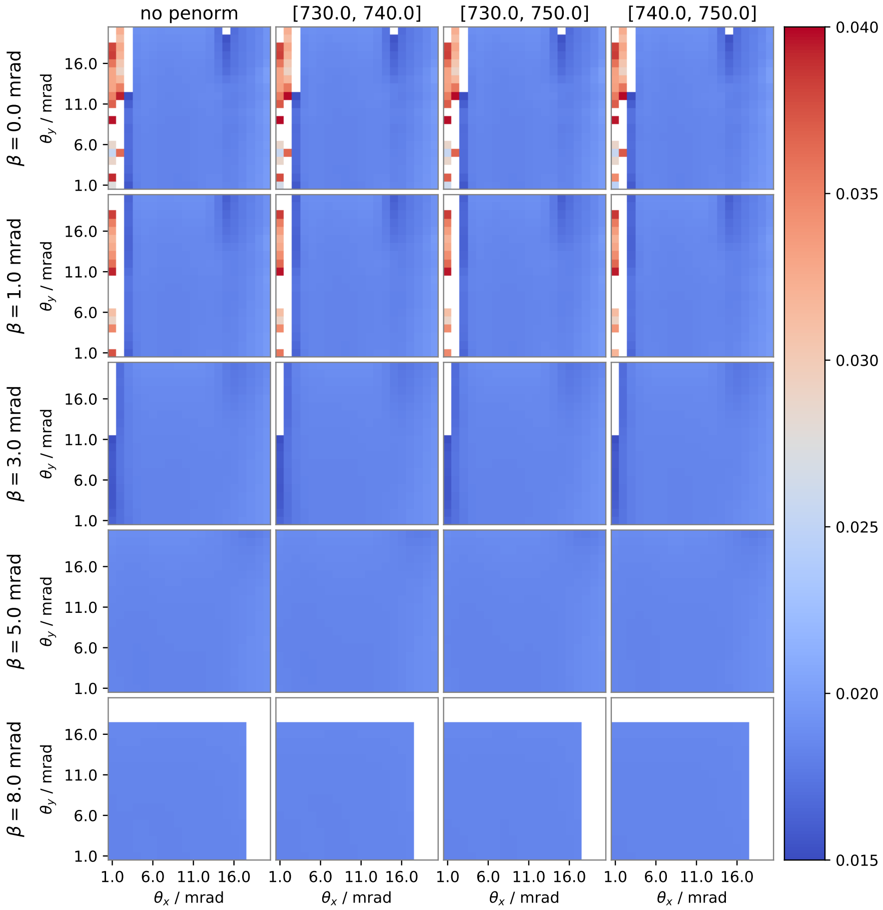

Figure A.18: m_L/m_S-maps comparing the effects of detector size and post-edge normalization range. Maps are computed from the pEMCD-signal for Rayleigh expansion up to third order at thickness 20 nm using the double difference method. The averaging range for determination of q is [745 eV, 750 eV].

A.2.1.3 m_L/m_S-averaging range for q: [750 eV, 760 eV]

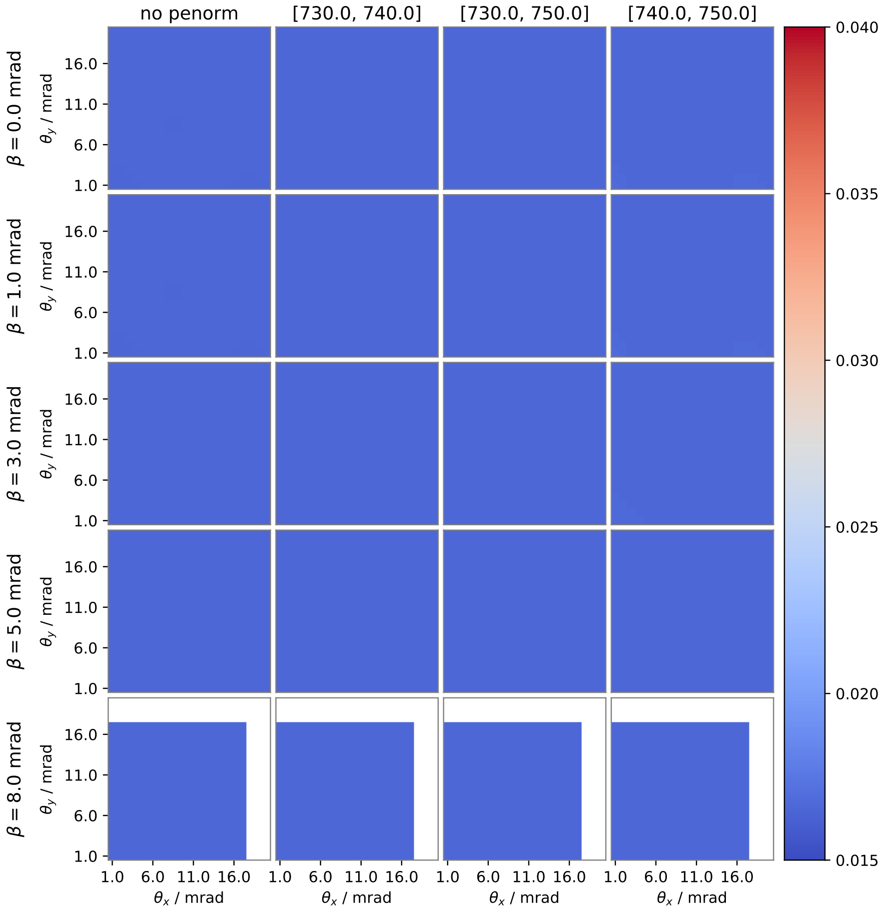

Figure A.19: m_L/m_S-maps comparing the effects of detector size and post-edge normalization range. Maps are computed in dipole approximation at thickness 10 nm using the double difference method from the pEMCD-signal. The averaging range for determination of q is [750 eV, 760 eV].

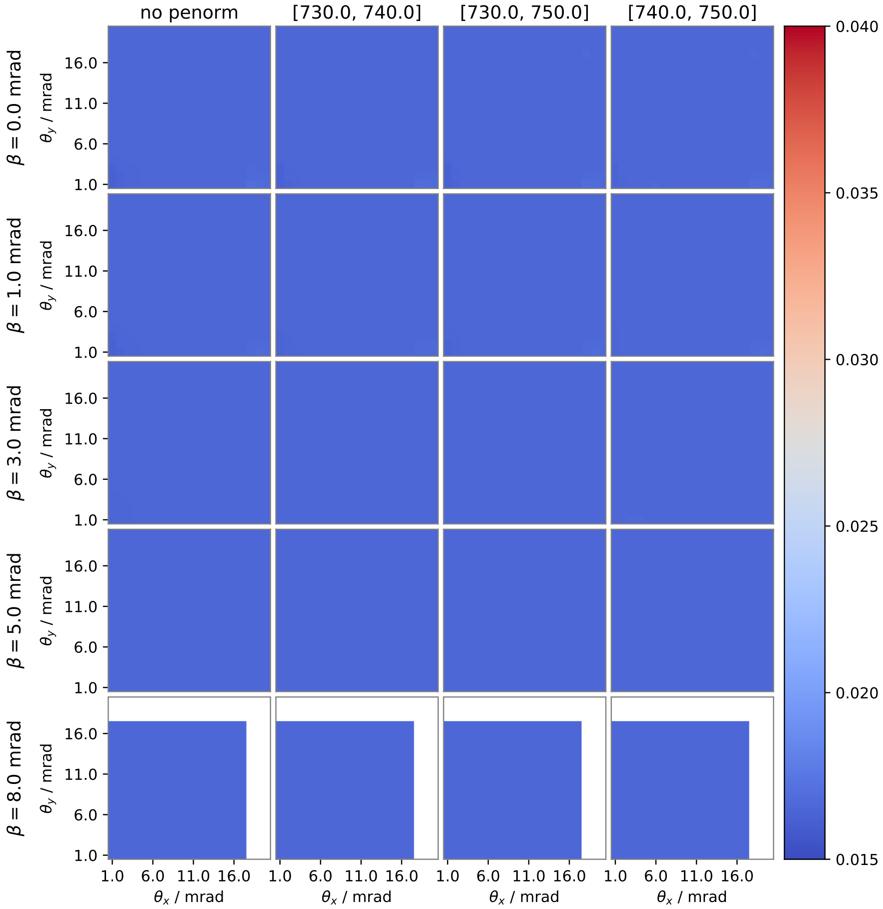

Figure A.20: m_L/m_S-maps comparing the effects of detector size and post-edge normalization range. Maps are computed in dipole approximation at thickness 15 nm using the double difference method from the pEMCD-signal. The averaging range for determination of q is [750 eV, 760 eV].

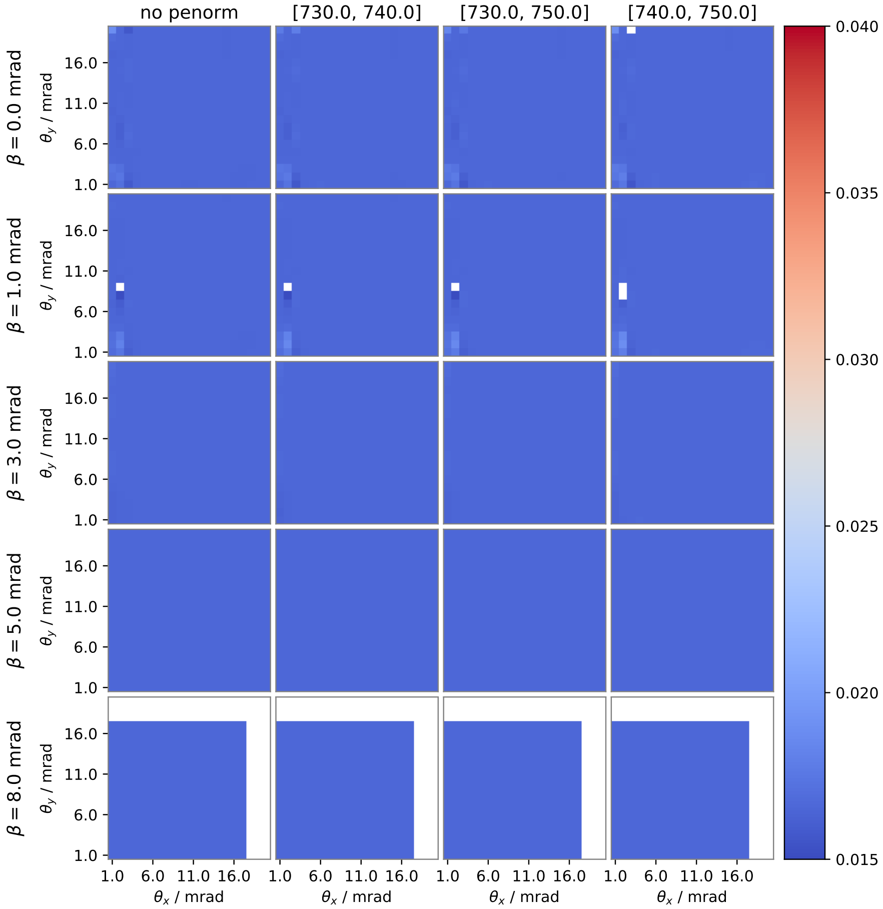

Figure A.21: m_L/m_S-maps comparing the effects of detector size and post-edge normalization range. Maps are computed in dipole approximation at thickness 20 nm using the double difference method from the pEMCD-signal. The averaging range for determination of q is [750 eV, 760 eV].

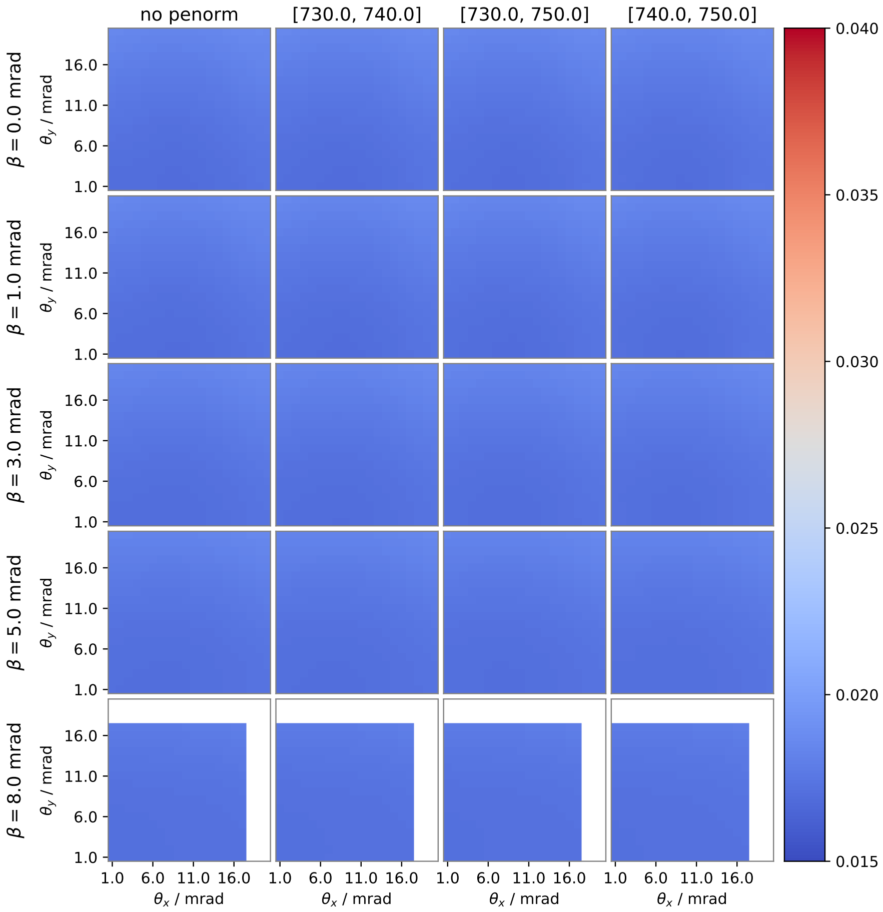

Figure A.22: m_L/m_S-maps comparing the effects of detector size and post-edge normalization range. Maps are computed in dipole approximation at thickness 10 nm using the double difference method from the pEMCD-signal. The averaging range for determination of q is [750 eV, 760 eV].

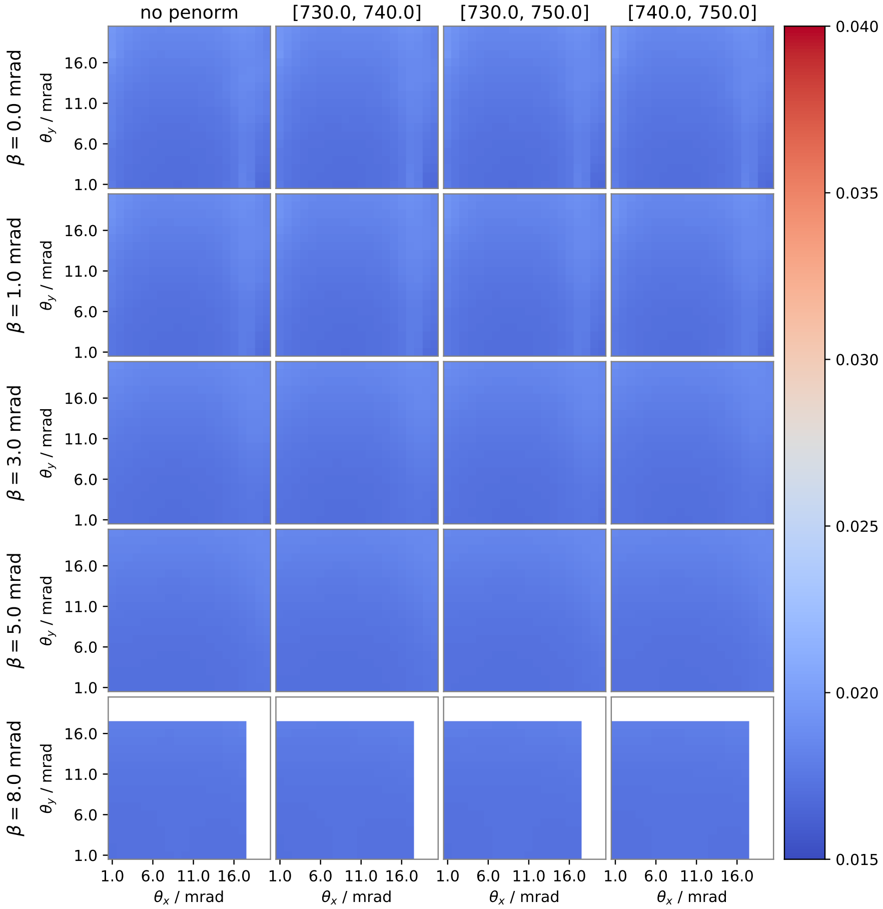

Figure A.23: m_L/m_S-maps comparing the effects of detector size and post-edge normalization range. Maps are computed in dipole approximation at thickness 15 nm using the double difference method from the pEMCD-signal. The averaging range for determination of q is [750 eV, 760 eV].

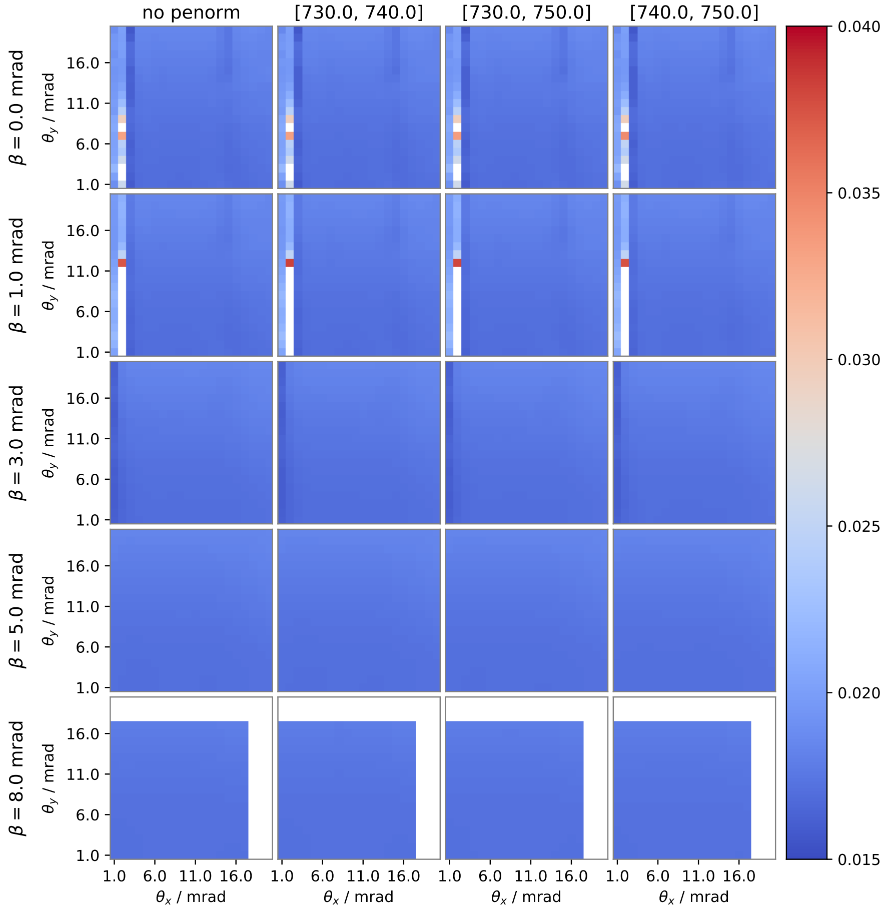

Figure A.24: m_L/m_S-maps comparing the effects of detector size and post-edge normalization range. Maps are computed in dipole approximation at thickness 20 nm using the double difference method from the pEMCD-signal. The averaging range for determination of q is [750 eV, 760 eV].

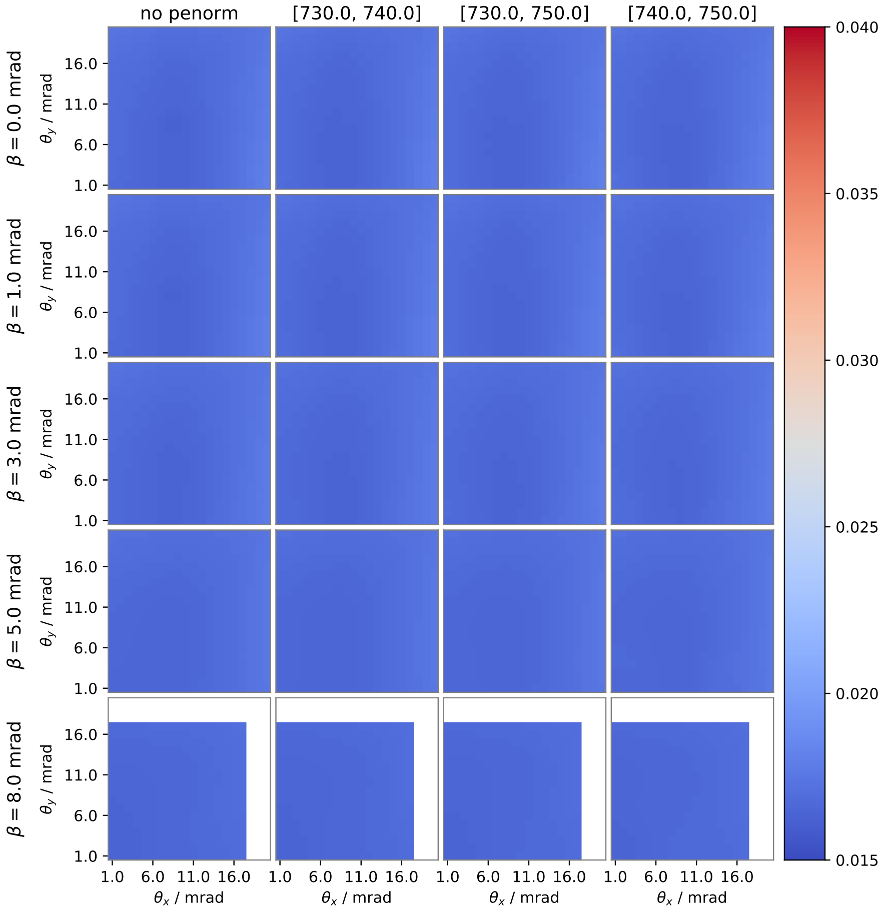

Figure A.25: m_L/m_S-maps comparing the effects of detector size and post-edge normalization range. Maps are computed for Rayleigh expansion up to third order at thickness 10 nm using the double difference method from the pEMCD-signal. The averaging range for determination of q is [750 eV, 760 eV].

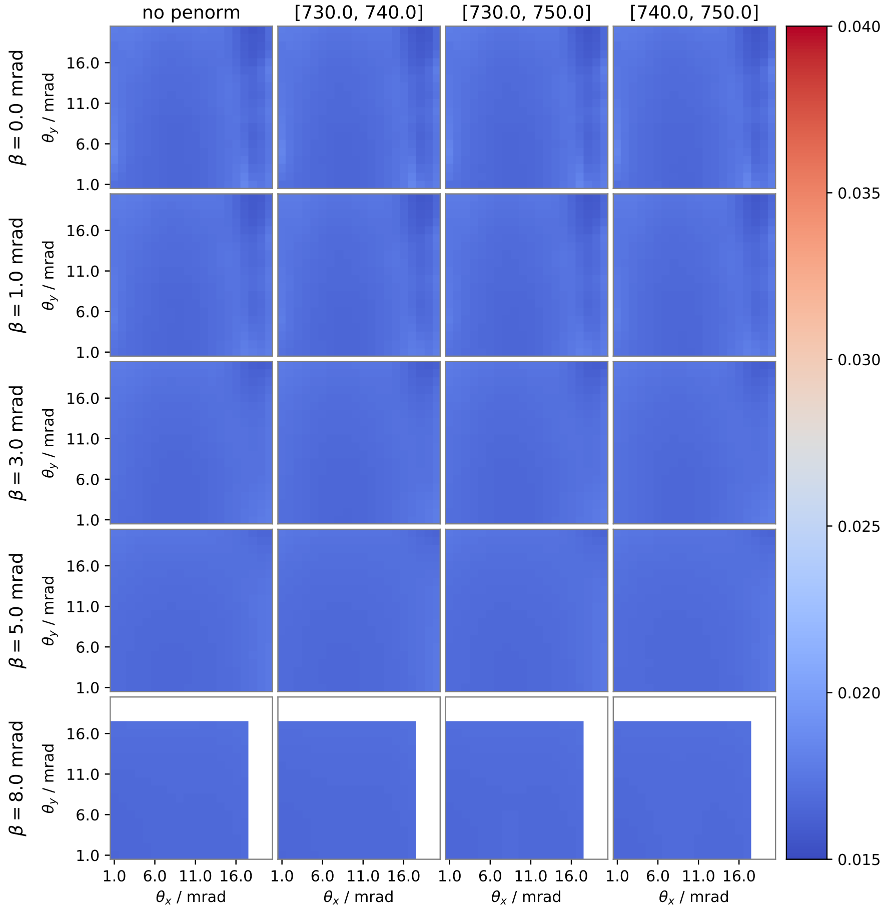

Figure A.26: m_L/m_S-maps comparing the effects of detector size and post-edge normalization range. Maps are computed in dipole approximation at thickness 15 nm using the double difference method from the pEMCD-signal. The averaging range for determination of q is [750 eV, 760 eV].

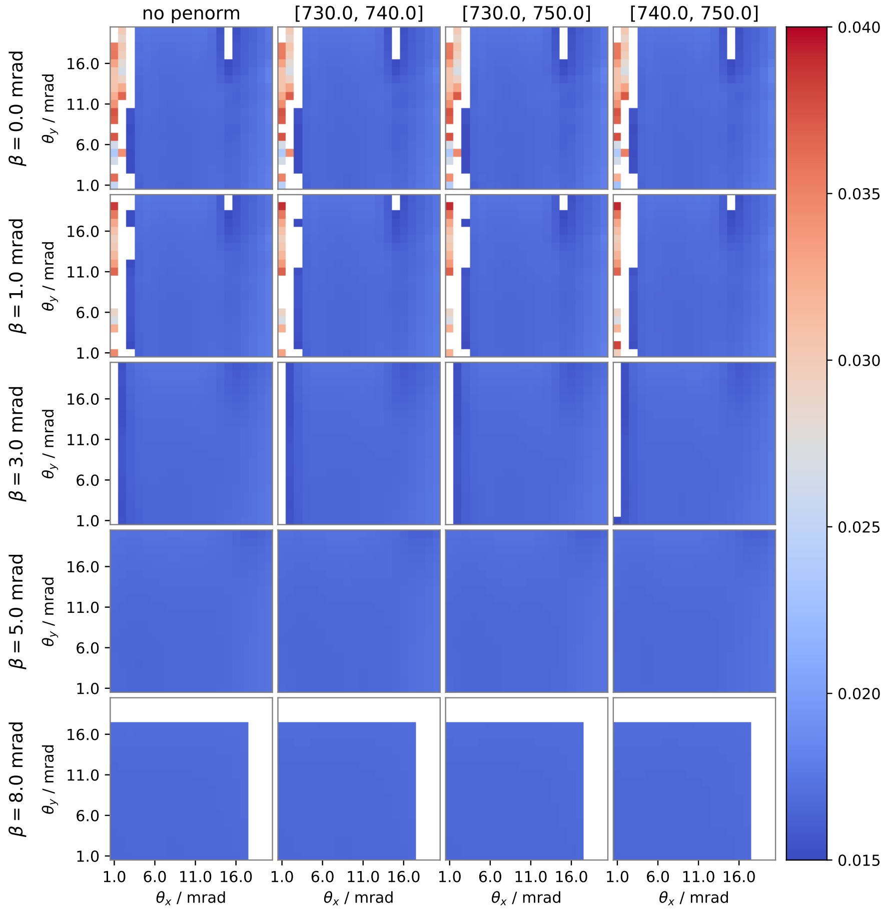

Figure A.27: m_L/m_S-maps comparing the effects of detector size and post-edge normalization range. Maps are computed for Rayleigh expansion up to third order at thickness 20 nm using the double difference method from the pEMCD-signal. The averaging range for determination of q is [750 eV, 760 eV].

A.2.2 *eEMCD*

Maps of the m_L/m_S-ratio for the double, up-down, and right-left difference methods are depicted in the figures in subsections A.2.2.1, A.2.2.3, and A.2.2.2, respectively. Refer to sections 4 and 5.4 for more information on the calculation procedure.

A.2.2.1 *Double difference method*

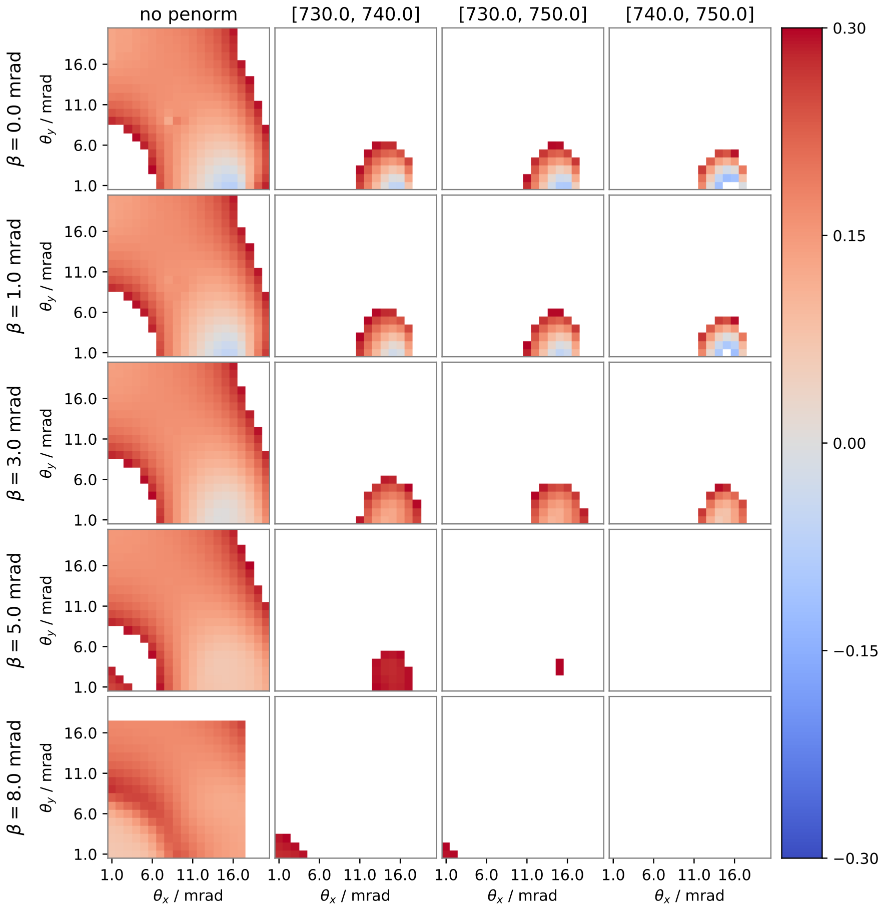

Figure A.28: m_L/m_S-maps comparing the effects of detector size and post-edge normalization range. Maps are computed from the eEMCD-signal in dipole approximation at thickness 10 nm using the double difference method. The averaging range for determination of q is equal to the post-edge normalization range.

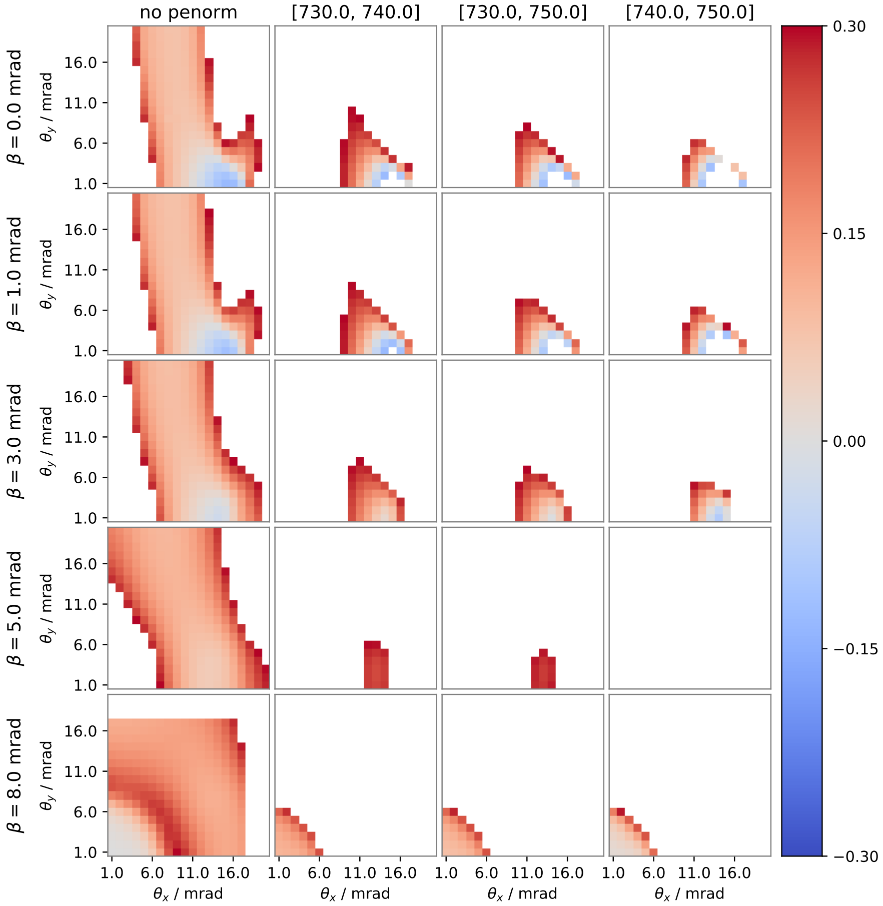

Figure A.29: m_L/m_S-maps comparing the effects of detector size and post-edge normalization range. Maps are computed from the eEMCD-signal in dipole approximation at thickness 20 nm using the double difference method. The averaging range for determination of q is equal to the post-edge normalization range.

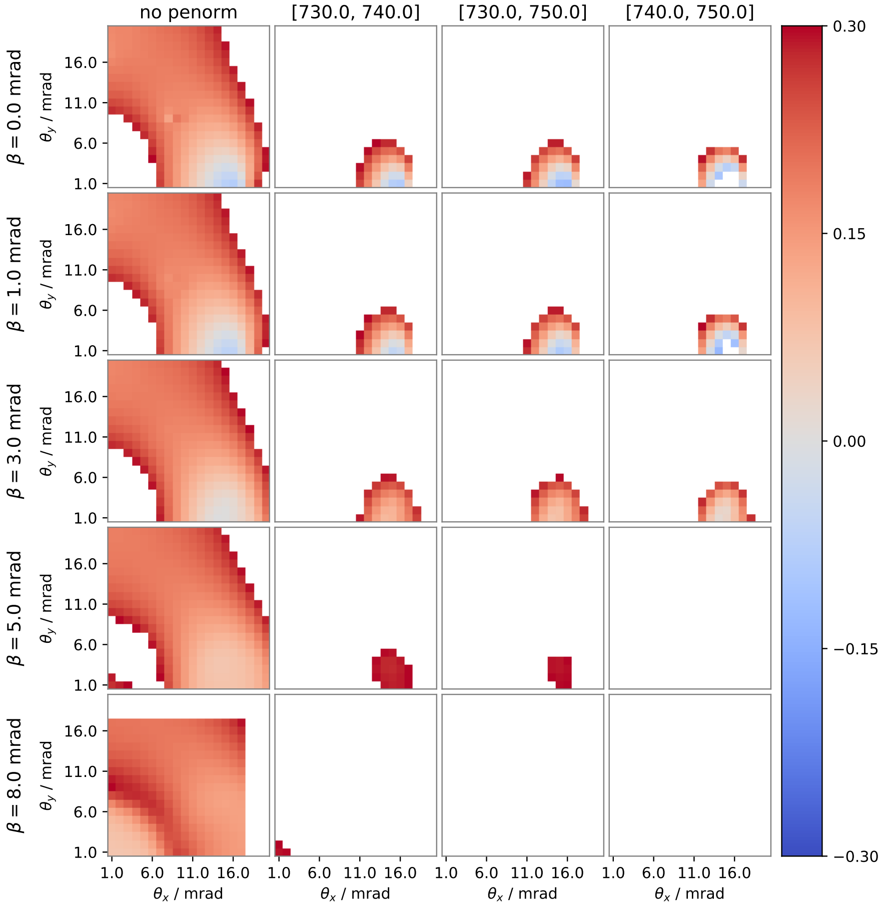

Figure A.30: m_L/m_S-maps comparing the effects of detector size and post-edge normalization range. Maps are computed from the eEMCD-signal for Rayleigh expansion up to third order at thickness 10 nm using the double difference method. The averaging range for determination of q is equal to the post-edge normalization range.

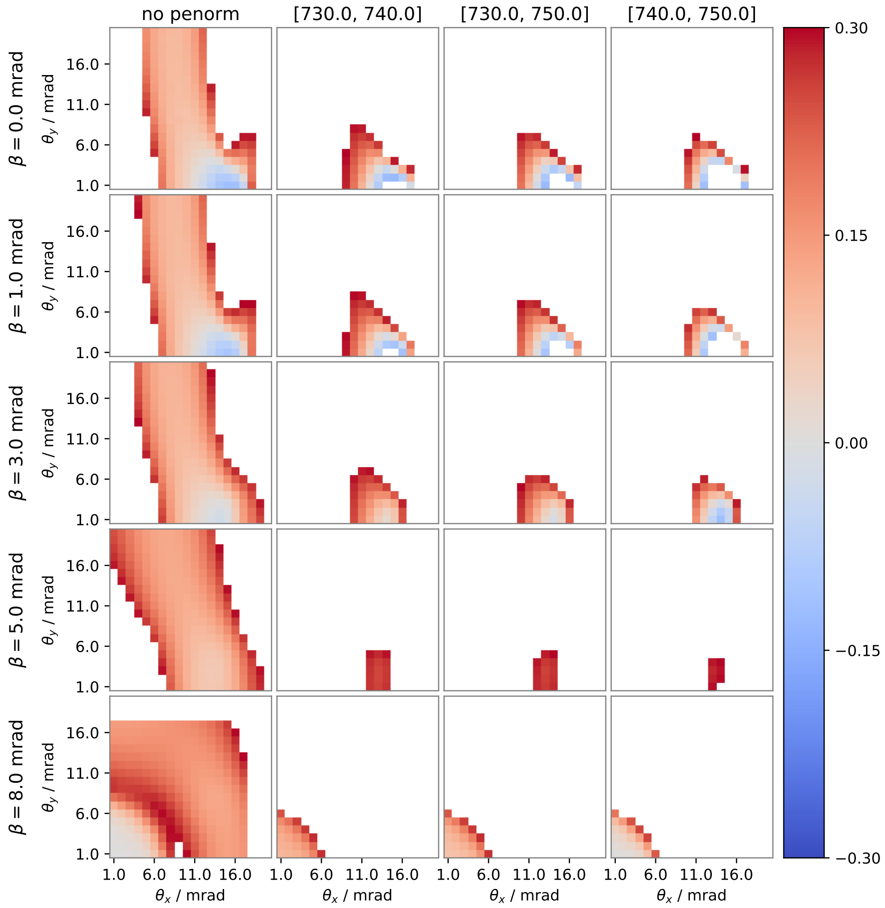

Figure A.31: m_L/m_S-maps comparing the effects of detector size and post-edge normalization range. Maps are computed from the eEMCD-signal for Rayleigh expansion up to third order at thickness 20 nm using the double difference method.

A.2.2.2 *Right-left difference method*

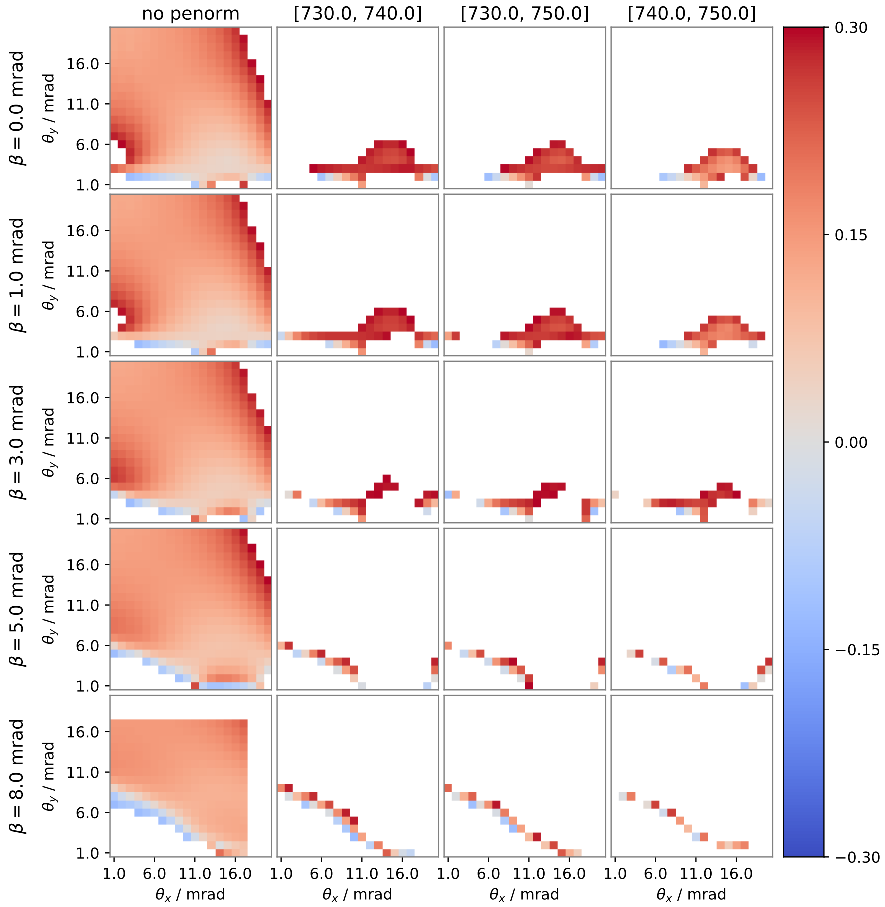

Figure A.32: m_L/m_S-maps comparing the effects of detector size and post-edge normalization range. Maps are computed from the eEMCD-signal in dipole approximation at thickness 10 nm using the up-down difference method. The averaging range for determination of q is equal to the post-edge normalization range.

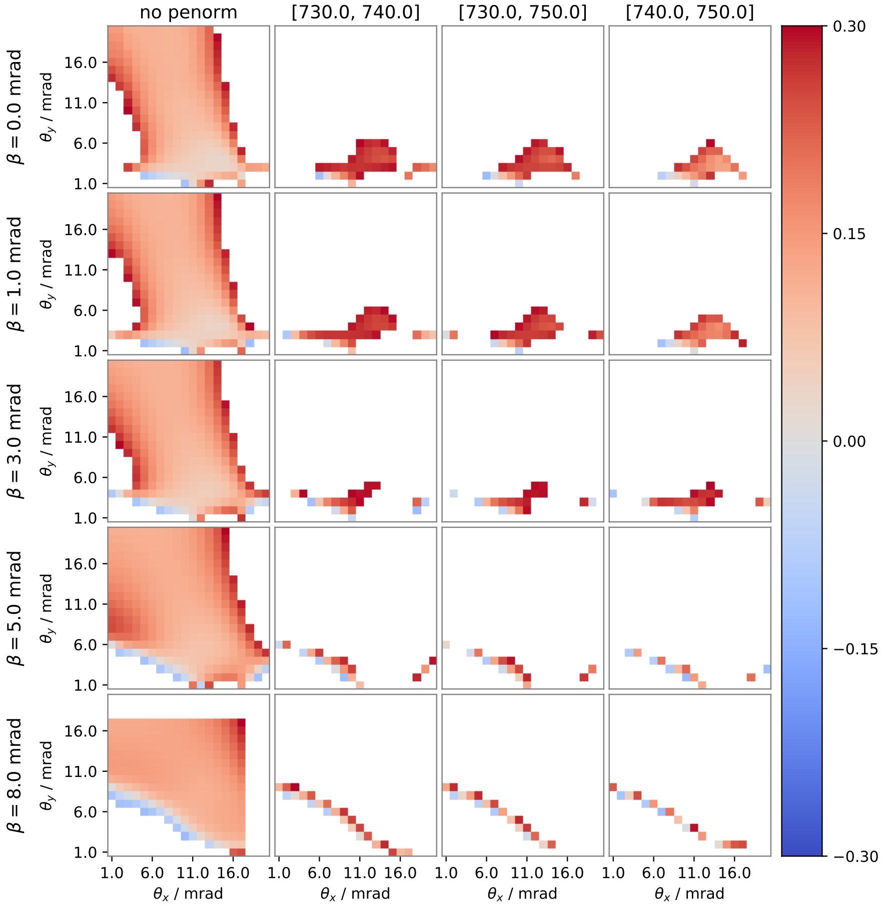

Figure A.33: m_L/m_S-maps comparing the effects of detector size and post-edge normalization range. Maps are computed from the eEMCD-signal in dipole approximation at thickness 15 nm using the right-left difference method. The averaging range for determination of q is equal to the post-edge normalization range.

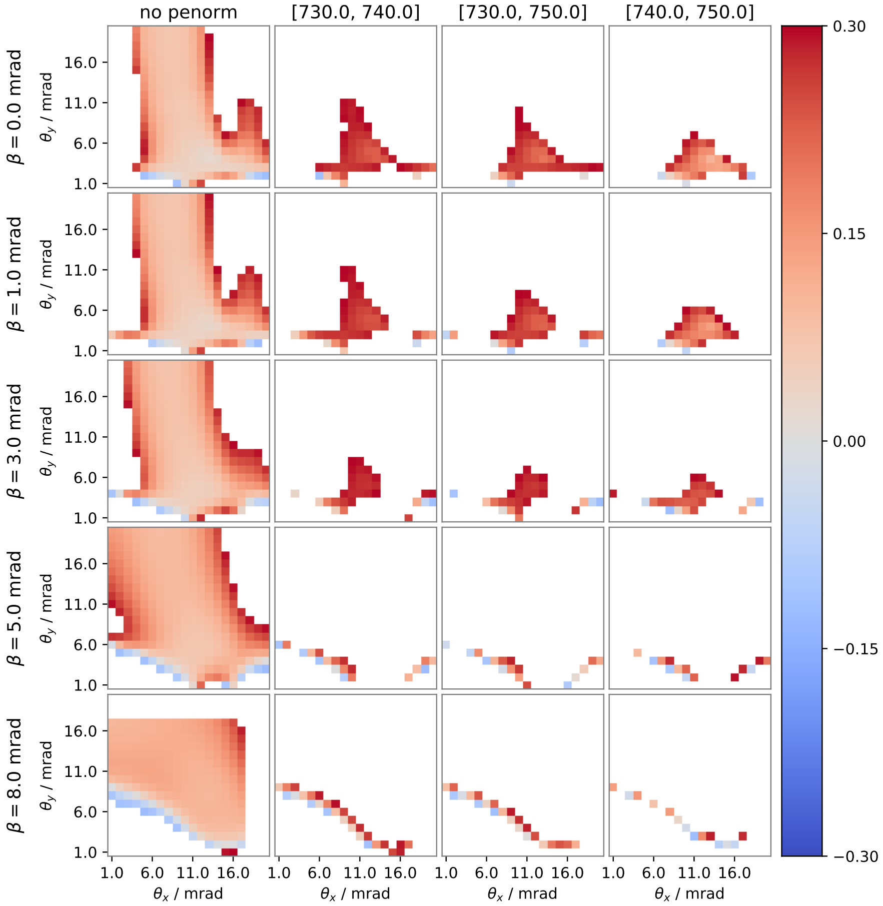

Figure A.34: m_L/m_S-maps comparing the effects of detector size and post-edge normalization range. Maps are computed from the eEMCD-signal in dipole approximation at thickness 20 nm using the right-left difference method. The averaging range for determination of q is equal to the post-edge normalization range.

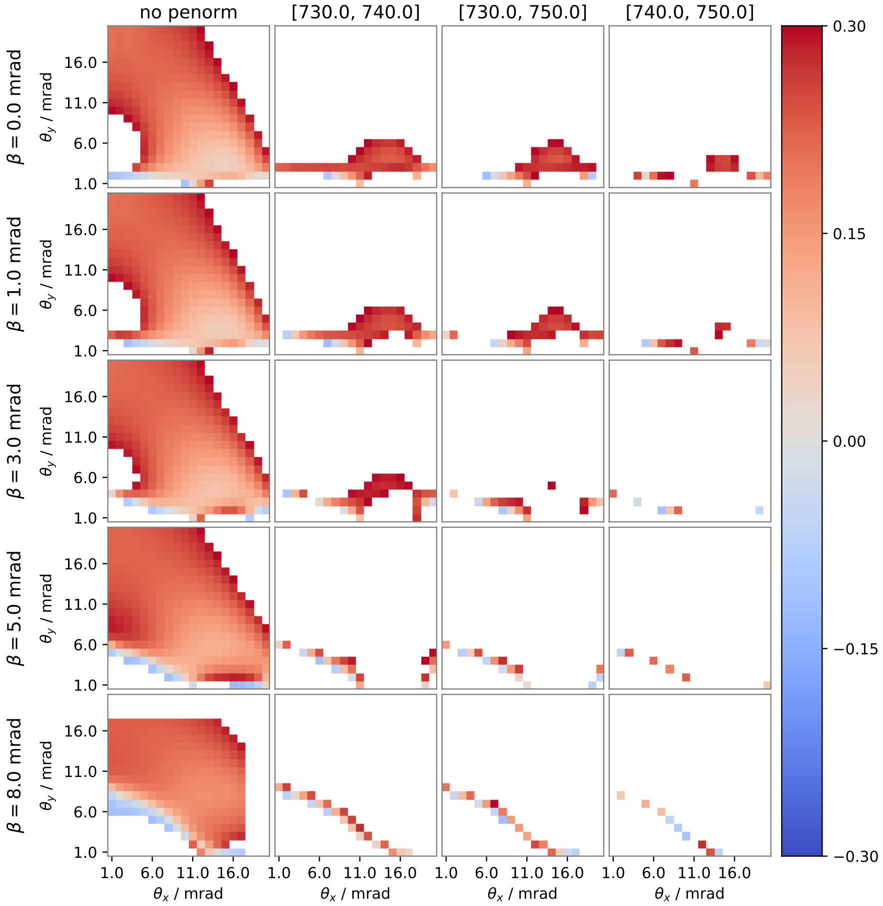

Figure A.35: m_L/m_S-maps comparing the effects of detector size and post-edge normalization range. Maps are computed from the eEMCD-signal for Rayleigh expansion up to third order at thickness 10 nm using the right-left difference method. The averaging range for determination of q is equal to the post-edge normalization range.

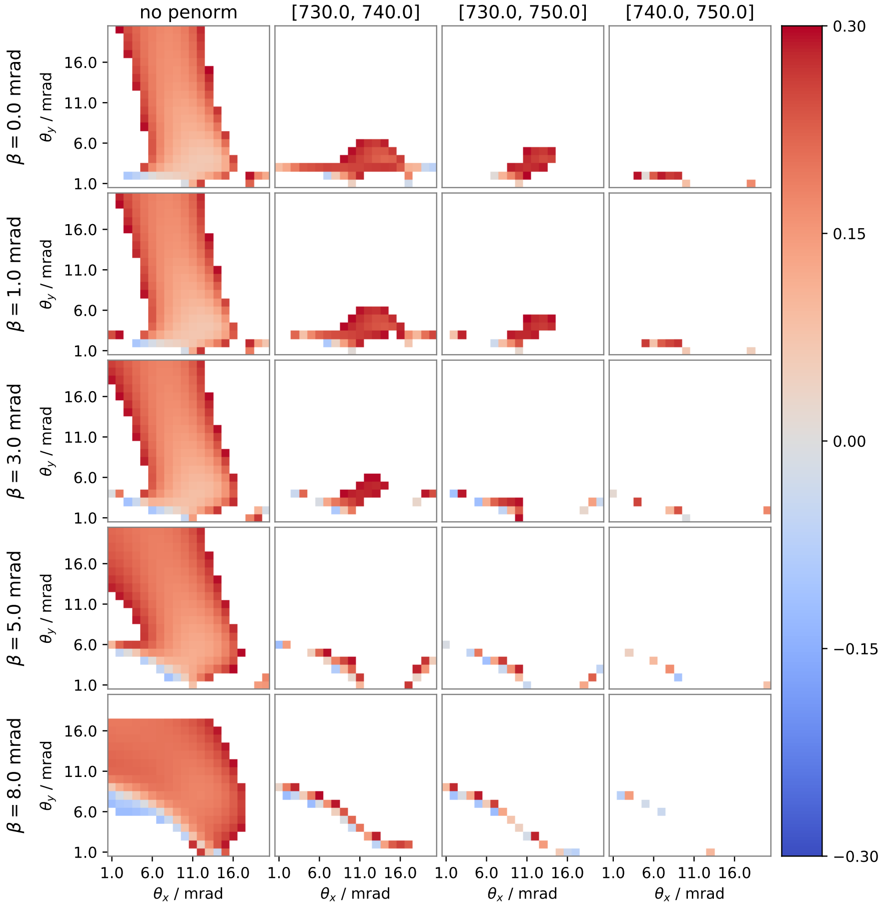

Figure A.36: m_L/m_S-maps comparing the effects of detector size and post-edge normalization range. Maps are computed from the eEMCD-signal for Rayleigh expansion up to third order at thickness 15 nm using the right-left difference method. The averaging range for determination of q is equal to the post-edge normalization range.

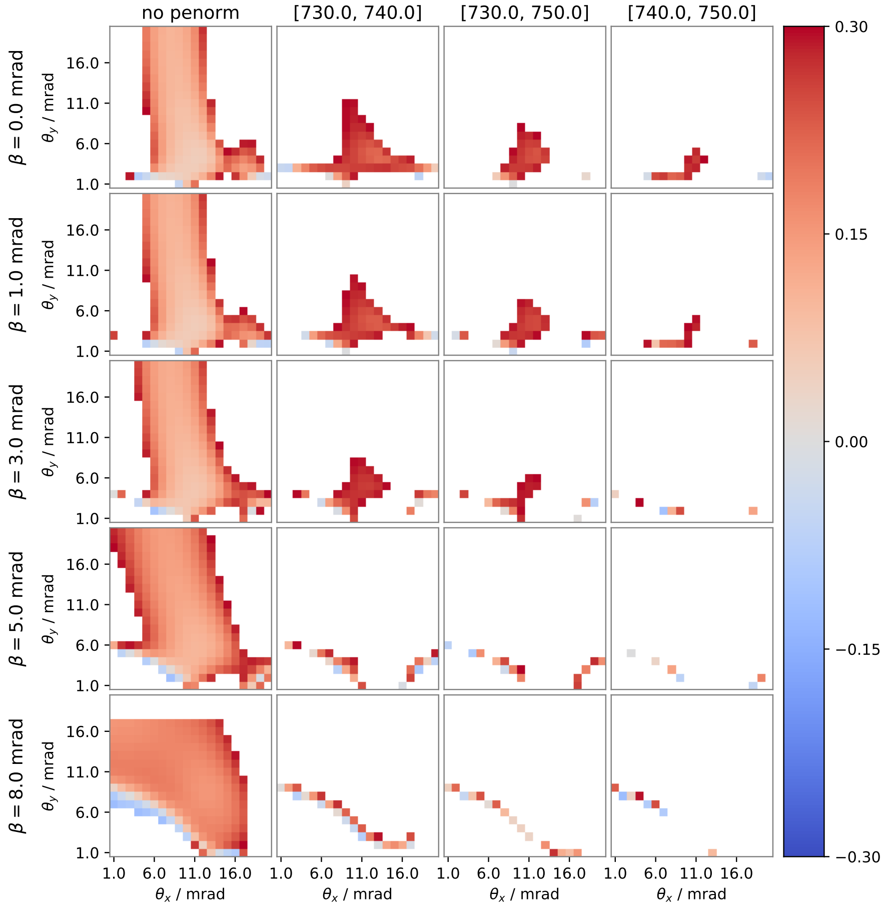

Figure A.37: m_L/m_S-maps comparing the effects of detector size and post-edge normalization range. Maps are computed from the eEMCD-signal for Rayleigh expansion up to third order at thickness 20 nm using the right-left difference method. The averaging range for determination of q is equal to the post-edge normalization range.

A.2.2.3 *Up-down difference method*

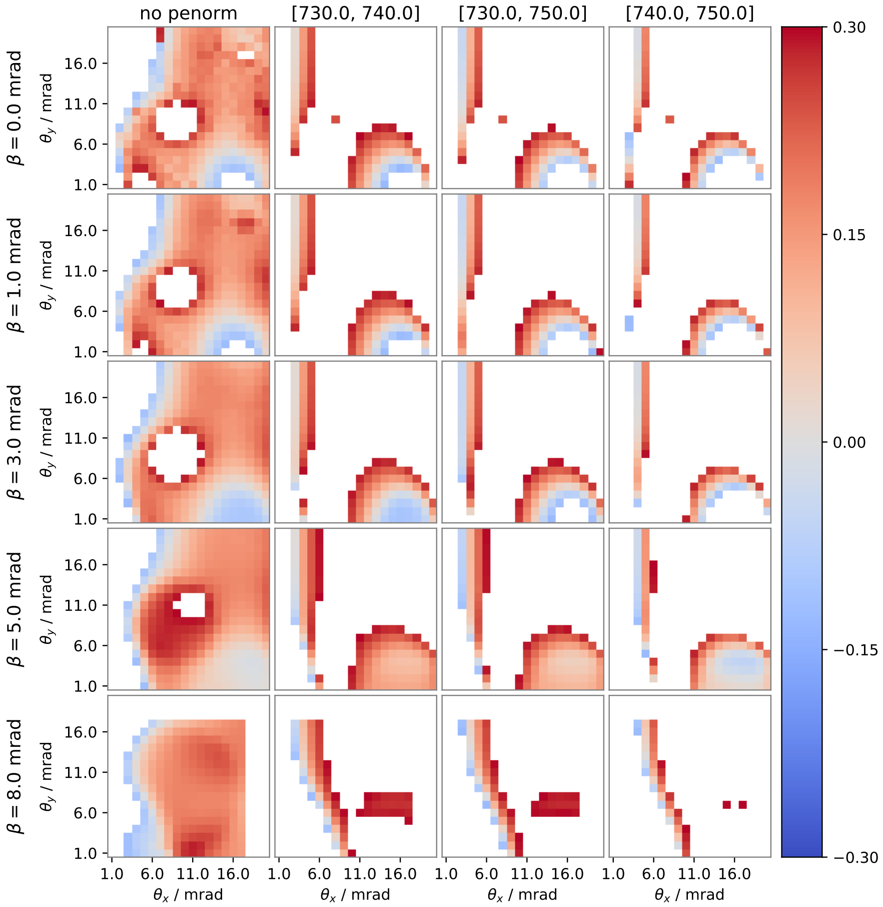

Figure A.38: m_L/m_S-maps comparing the effects of detector size and post-edge normalization range. Maps are computed from the eEMCD-signal in dipole approximation at thickness 10 nm using the up-down difference method. The averaging range for determination of q is equal to the post-edge normalization range.

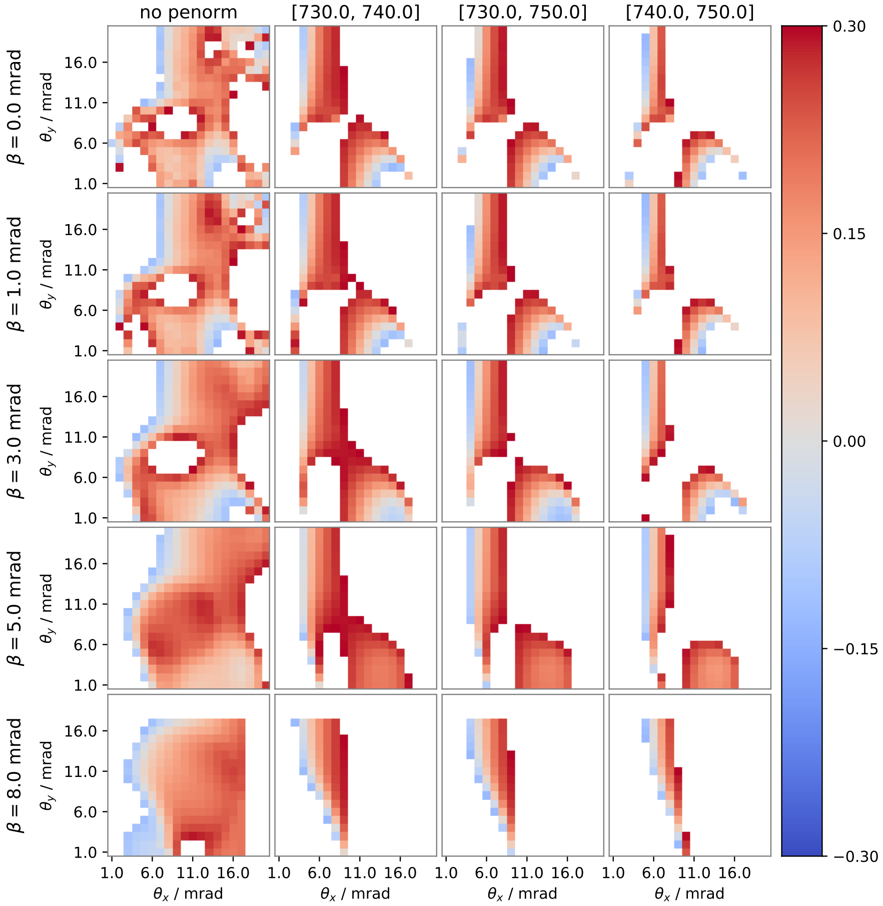

Figure A.39: m_L/m_S-maps comparing the effects of detector size and post-edge normalization range. Maps are computed from the eEMCD-signal in dipole approximation at thickness 15 nm using the up-down difference method. The averaging range for determination of q is equal to the post-edge normalization range.

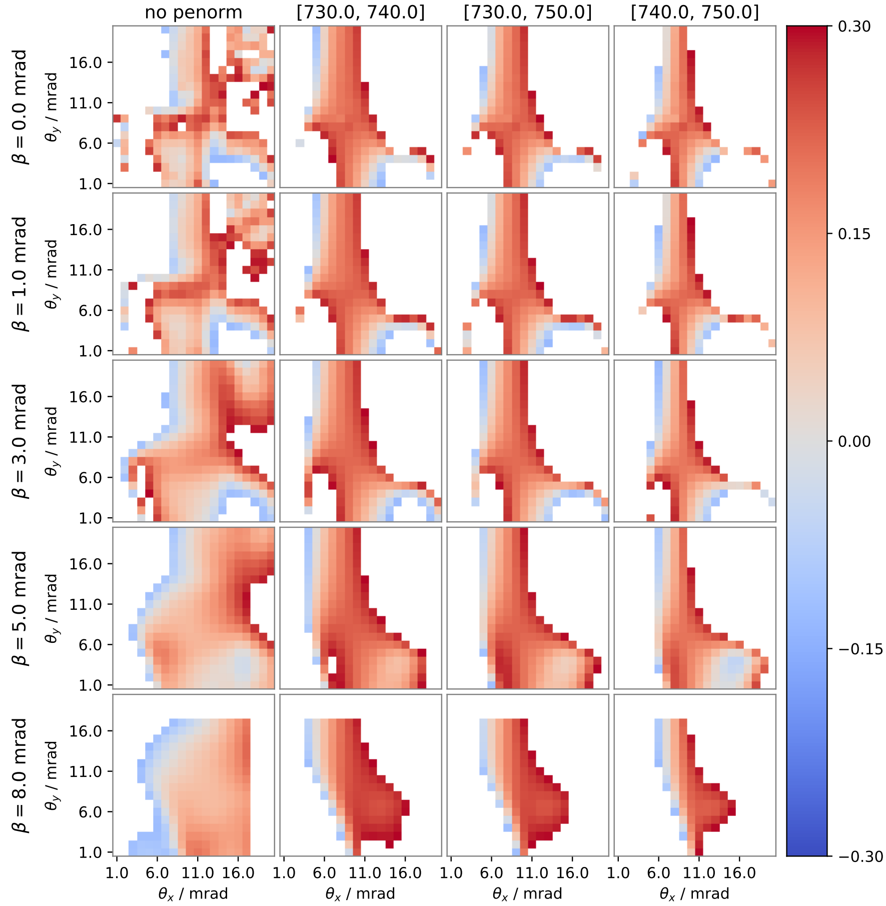

Figure A.40: m_L/m_S-maps comparing the effects of detector size and post-edge normalization range. Maps are computed from the eEMCD-signal in dipole approximation at thickness 20 nm using the up-down difference method. The averaging range for determination of q is equal to the post-edge normalization range.

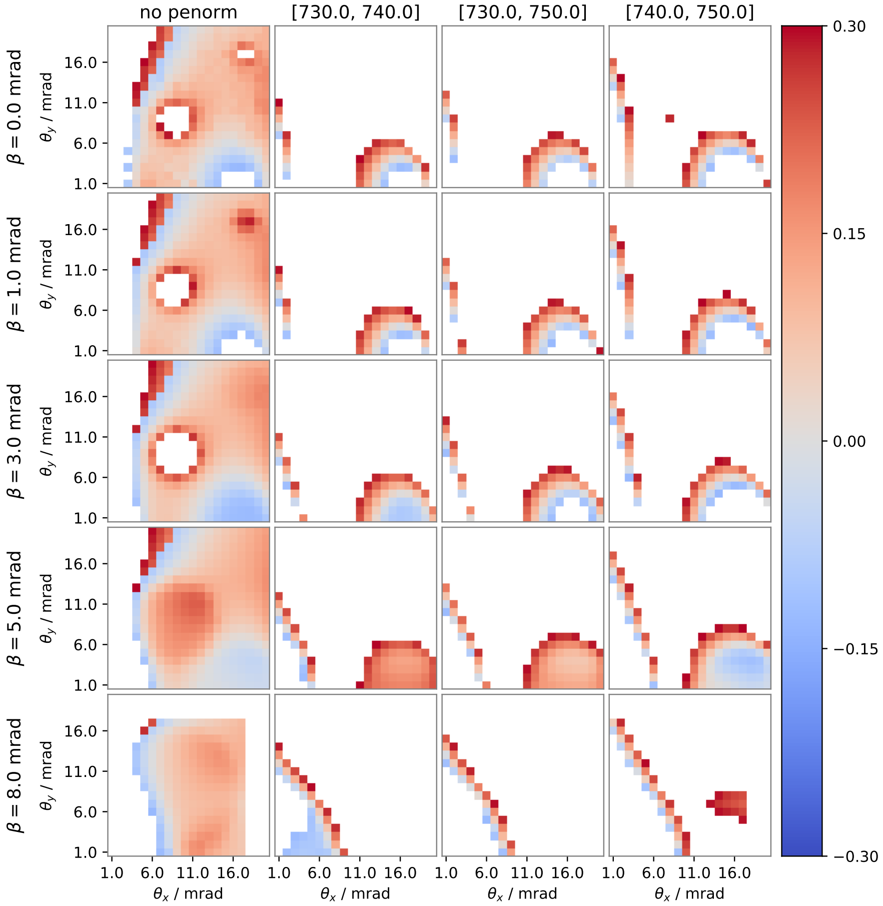

Figure A.41: m_L/m_S-maps comparing the effects of detector size and post-edge normalization range. Maps are computed from the eEMCD-signal for Rayleigh expansion up to third order at thickness 10 nm using the up-down difference method. The averaging range for determination of q is equal to the post-edge normalization range.

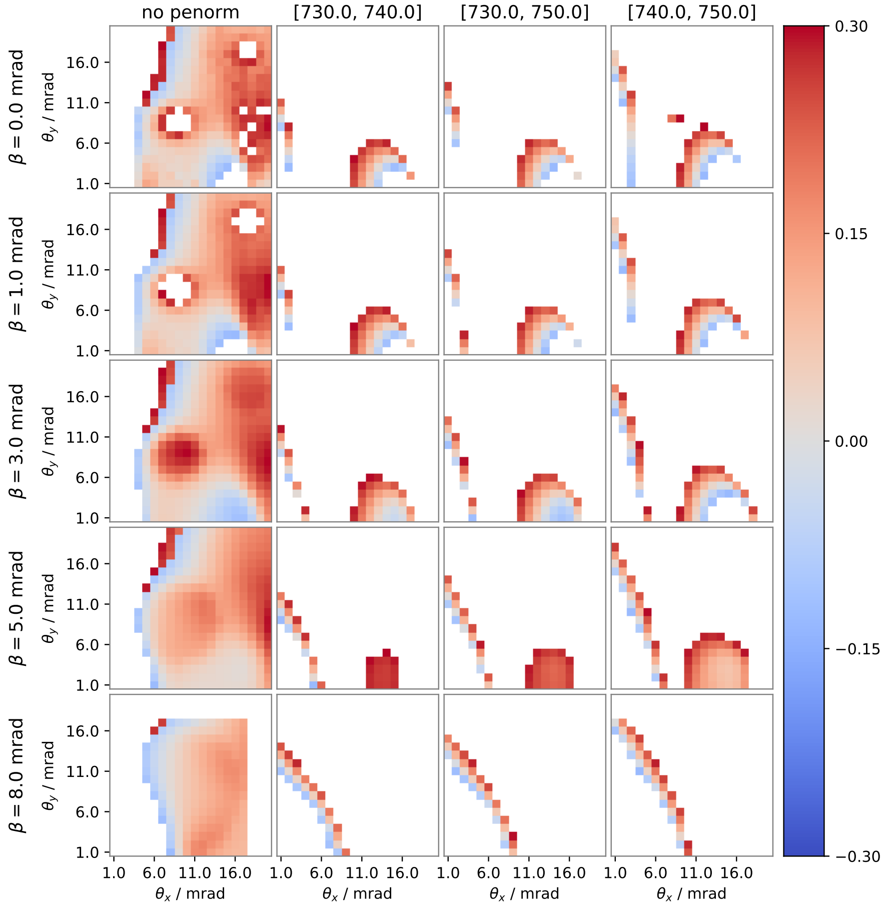

Figure A.42: m_L/m_S-maps comparing the effects of detector size and post-edge normalization range. Maps are computed from the eEMCD-signal for Rayleigh expansion up to third order at thickness 15 nm using the up-down difference method. The averaging range for determination of q is equal to the post-edge normalization range.

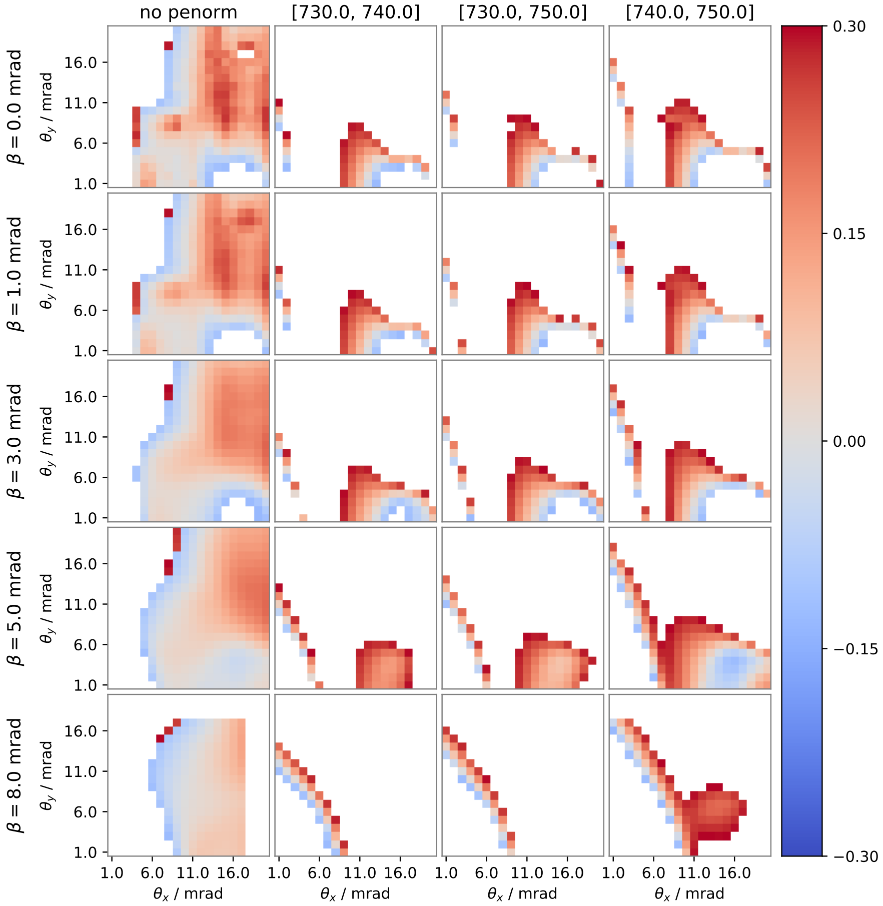

Figure A.43: m_L/m_S-maps comparing the effects of detector size and post-edge normalization range. Maps are computed from the eEMCD-signal for Rayleigh expansion up to third order at thickness 20 nm using the up-down difference method. The averaging range for determination of q is equal to the post-edge normalization range.

A.3 ADDITIONAL MAPS OF THE APPARENT ANISOTROPY

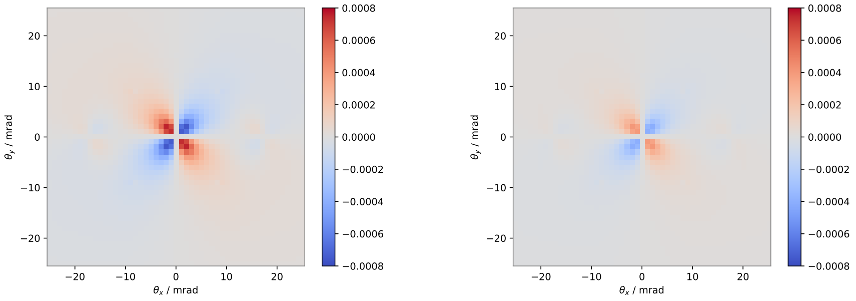

(a) dipole-approximation @ L_3-edge (b) dipole-approximation @ L_2-edge

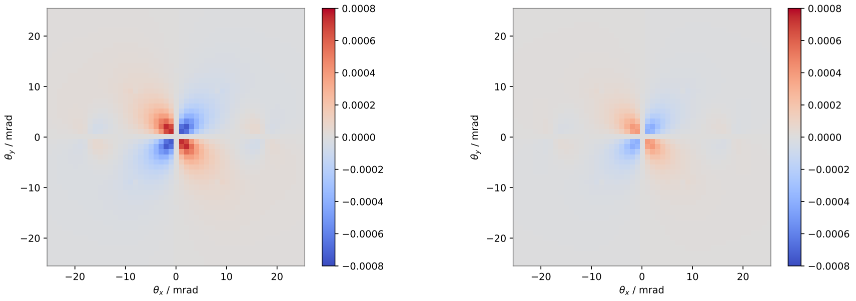

(c) 11-diagonal term @ L_3-edge (d) 11-diagonal term @ L_2-edge

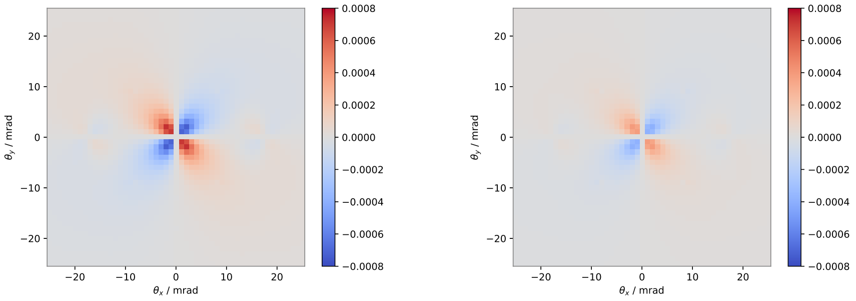

(e) lamb3-approximation @ L_3-edge (f) lamb3-approximation @ L_2-edge

Figure A.44: Maps showing the contribution to the eEMCD-signal, which is attributable to the real part of the MDFF, i.e., maps showing the difference between the maps shown in figure A.3 and A.1 the pEMCD-signal for the following approximations to the MDFF: dipole approximation, computed from the 11-term, and in lamb3-approximation at the L_3- and L_2-edge at thickness 10 nm.

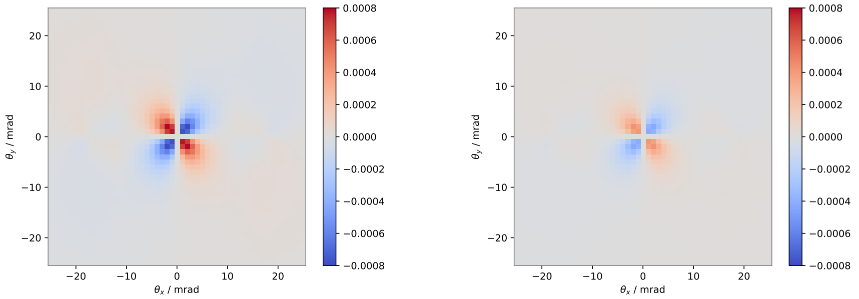

(a) dipole-approximation @ L_3-edge (b) dipole-approximation @ L_2-edge

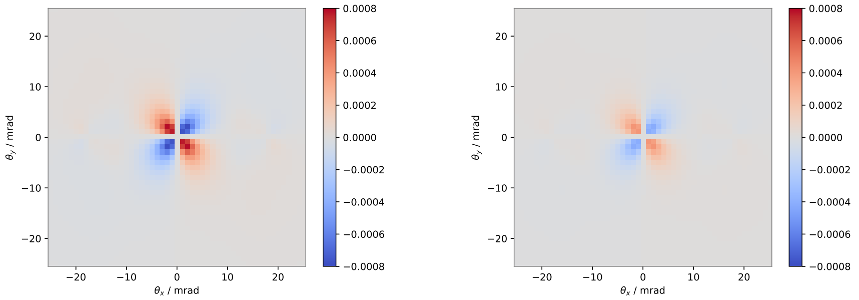

(c) 11-diagonal term @ L_3-edge (d) 11-diagonal term @ L_2-edge

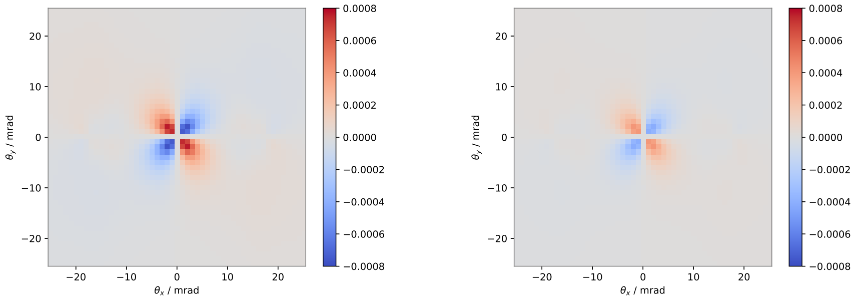

(e) lamb3-approximation @ L_3-edge (f) lamb3-approximation @ L_2-edge

Figure A.45: Maps showing the contribution to the eEMCD-signal, which is attributable to the real part of the MDFF, i.e., maps showing the difference between the maps shown in figure A.4 and A.2 the pEMCD-signal for the following approximations to the MDFF: dipole approximation, computed from the 11-term, and in lamb3-approximation at the L_3- and L_2-edge at thickness 20 nm.

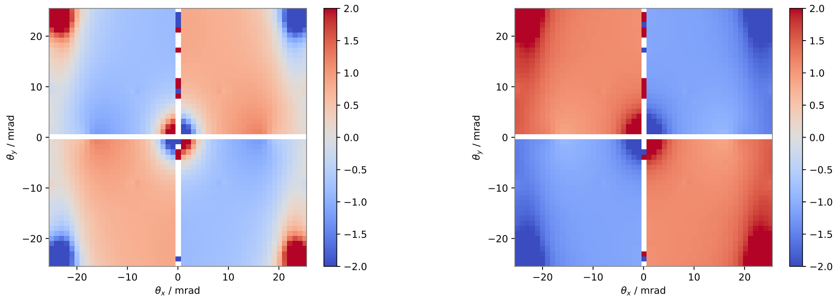

(a) dipole-approximation @ L_3-edge (b) dipole-approximation @ L_2-edge

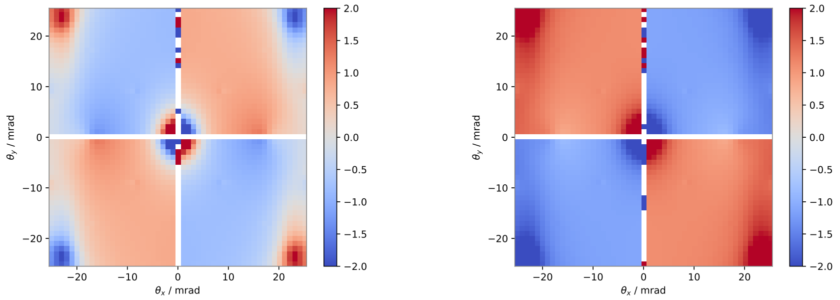

(c) 11-diagonal term @ L_3-edge (d) 11-diagonal term @ L_2-edge

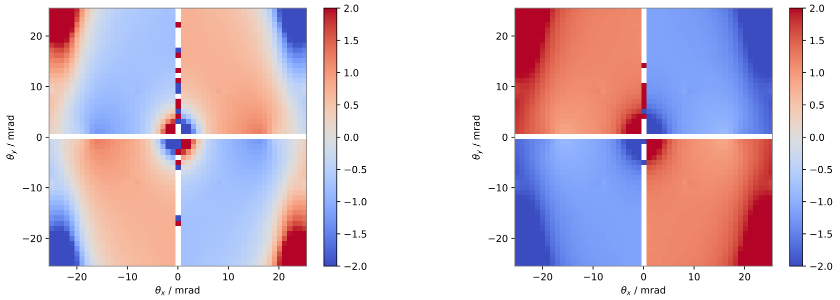

(e) lamb3-approximation @ L_3-edge (f) lamb3-approximation @ L_2-edge

Figure A.46: Edge-resolved maps of the relative strength of the contribution due to the real part of the MDFF to the energy-integrated eEMCD-signal $\Delta\sigma^{L_j}_{\mathrm{dd,re}}/\Delta\sigma^{L_j}_{\mathrm{dd,im}}$ for selected approximation levels of the MDFF at thickness 10 nm.

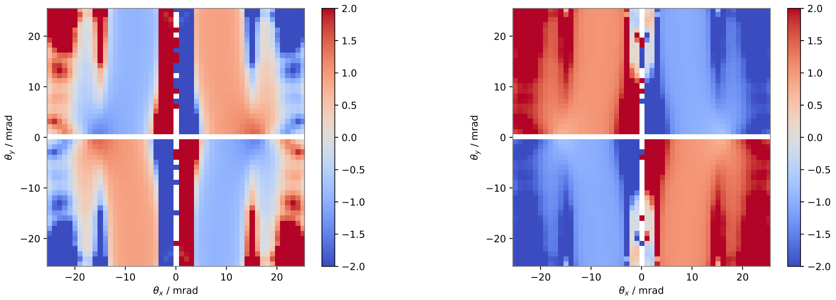

(a) dipole-approximation @ L_3-edge (b) dipole-approximation @ L_2-edge

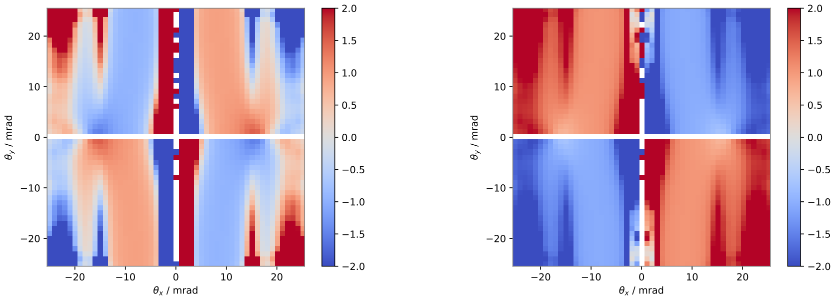

(c) 11-diagonal term @ L_3-edge (d) 11-diagonal term @ L_2-edge

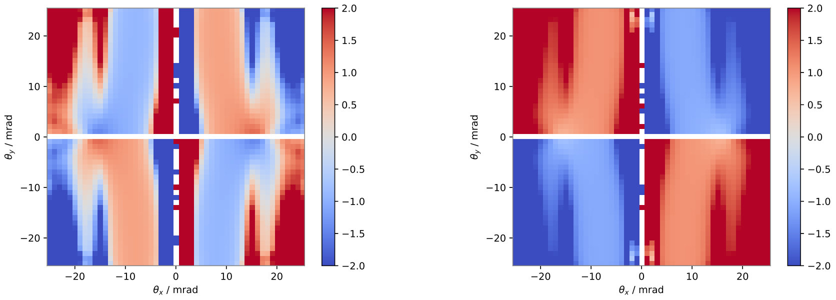

(e) lamb3-approximation @ L_3-edge (f) lamb3-approximation @ L_2-edge

Figure A.47: Edge-resolved maps of the relative strength of the contribution due to the real part of the MDFF to the energy-integrated eEMCD-signal $\Delta\sigma_{\mathrm{dd,re}}^{L_j}/\Delta\sigma_{\mathrm{dd,im}}^{L_j}$ for selected approximation levels of the MDFF at thickness 20 nm.